Theoretical Assessment of ϕ - $f_1(1420)$ Mass Degeneracy Induced by Density-Driven Chiral Mixing Based on ϕ Production Cross Section Measurement at J-PARC E16

Ren Ejima

A thesis submitted for the degree of
Doctor of Philosophy

March 1, 2026

Graduate School of Advanced Science and Engineering
Hiroshima University

Supervisor: Kenta Shigaki

Abstract

The purpose of this study is to experimentally clarify the origin of hadron masses. For many years, the connection between hadron mass generation and chiral symmetry has been investigated through in-medium vector-meson mass modifications observed in lepton-pair production. However, this issue remains unresolved because mass changes caused by chiral symmetry restoration cannot be clearly separated from those induced by hadron–medium interactions. In this study, we take a different approach by focusing on the mass degeneracy of chiral partners, which is difficult to explain solely by medium interactions. Observing multiple degeneracies would therefore provide more direct evidence for chiral symmetry restoration. Although detecting lepton pairs from axial-vector mesons—the chiral partners of vector mesons—has long been considered challenging due to the requirement of chiral mixing, we propose using a zero-temperature, finite-density medium. In contrast to finite-temperature systems, chiral mixing at finite density occurs through a fundamentally different mechanism and is not suppressed at the chiral phase transition or by thermal photons, making the observation of axial-vector mesons feasible. Based on chiral mixing at finite density, we estimate its impact on the electron-pair invariant mass spectrum measurable in the J-PARC E16 experiment and assess the feasibility of observing chiral-partner mass degeneracy. Using the faint ϕ-meson signal observed during the detector commissioning run (J-PARC E16 Run0-e), we evaluated the ϕ-meson production cross section in 30 GeV p+A collisions. This cross section is then used as input to estimate the production of the ϕ meson and its chiral partner, $f_1(1420)$ meson, by the chiral effective field theory for the planned physics run, J-PARC E16 Run2. We further evaluate the expected significance and observability of mass degeneracy of them. The results show that, assuming ideal chiral mixing, the use of two lead targets throughout the Run2 beam time would allow observation at approximately the 2σ level. Moreover, if chiral symmetry in the strange sector is restored by as little as 10% at nuclear density, the invariant mass distribution exhibits a mass shift toward degeneracy of about 30–40 MeV, which is enough to observe with the mass resolution of the E16 spectrometer.

Acknowledgments

This research is fundamentally based on collaborative work with my advisor, Professor Kenta Shigaki, Professor Chihiro Sasaki of the University of Wrocław, and Philipp Gubler of JAEA. I extend my deepest gratitude to all three. Professor Kenta Shigaki not only engaged in discussions regarding the estimation of experimental effects within this research but also provided daily support for my work. Professor Chihiro Sasaki engaged in extensive discussions with me regarding the fundamental theoretical aspects of this research. Furthermore, being invited to the University of Wrocław and given the opportunity to present a seminar there was an immensely valuable experience. Philipp Gubler handled the calculations using the transport model employed in this research and participated in our daily physics discussions. I would like to express my gratitude to these three individuals once again. Furthermore, the J-PARC E16 collaborators provided invaluable cooperation regarding the use of RIKEN CCJ for background calculations and the ϕ meson production cross section measurements used in this research. In particular, I discussed background calculations with Satoshi Yokkaichi. Kyoichiro Ozawa, Tomoki Murakami, and Wataru Nakai taught me detector work from the ground up for the experiment's execution and engaged in discussions regarding detector improvements. Satomi Nakasuga and Yuhei Morino taught me the entire analysis process, from signals from the detector to tracking and obtaining the electron pair invariant mass distribution. Kazuya Aoki, Masaya Ichikawa, Shunnosuke Nagafusa, and others provided tremendous assistance with daily detector operations. I would like to express my gratitude once again to all the J-PARC E16 collaborators. Furthermore, I received significant financial support from the Japan Society for the Promotion of Science (JSPS), WPI-SKCM2, and KEK. I am deeply grateful.

Contents

List of Figures

List of Tables

Chapter 1

Introduction

In the following sections, we discuss the origin of the hadron mass(§1.1), and the situation of experimental research on it.

1.1 Origin of Hadron's Mass

1.1.1 Chiral Symmetry and its Spontaneously Breaking

First, we will discuss the spontaneous breaking of the chiral symmetry, which is closely related to the mass of hadrons. The strong interactions governing hadrons and the quarks that make up hadrons are described by the following QCD Lagrangian.

$$\mathcal{L}_{QCD} = \bar{q}_{\alpha,f}(i\gamma^{\mu}D_{\mu}^{\alpha\beta} - m_f\delta^{\alpha\beta})q_{\beta,f} - \frac{1}{4}G_{\mu\nu}^{\alpha}G_{a}^{\mu\nu} \tag{1.1}$$

Here we take the limit where the mass of the quark is zero. This limit is called the chiral limit. In the chiral limit, when considering N_f quarks, the QCD Lagrangian has the following symmetry.

$$SU(N_f)_L \times SU(N_f)_R \times U(1)_V \times U(1)_A \tag{1.2}$$

Of these, $SU(N_f)_L \times SU(N_f)_R$ is chiral symmetry, $U(1)_V$ is baryon number conservation, and $U(1)_A$ is axial U(1) symmetry. Chiral symmetry is a symmetry for transformations that rotate the phase of the right-handed and left-handed components of the field independently, called chiral transformations, such as the following.

$$\psi \to e^{it^a(\theta_V + \gamma^5\theta_A)}\psi \tag{1.3}$$

In reality, however, the chiral symmetry is overtly broken because quarks have mass. Furthermore, the QCD vacuum breaks the chiral symmetry spontaneously as well by creating quark-anti-quark pair condensates in the vacuum to stabilize it. This phenomenon is similar to the phase transition of metals to superconductivity. The chiral symmetry is then broken as follows.

$$SU(N_f)_L \times SU(N_f)_R \to SU(N_f)_V \tag{1.4}$$

Then, when the chiral symmetry is broken, π, K mesons, etc. appear as Nambu Goldstone particles, and the vacuum condenses quark-antiquark pairs, as described earlier. These quark-antiquark pairs are not symmetric to the chiral transformation, and the vacuum expectation value of the quark-antiquark pairs is an order parameter of the spontaneous breaking of the chiral symmetry. And hadrons in the vacuum of condensed quark-antiquark pairs become much heavier than the mass sum of their constituent quarks because their condensation acts like water resistance. This is the same mechanism by which elementary particles gain mass through the Higgs mechanism.

1.1.2 Hadron's Mass in Finite Temperature and Density

This section examines how hadron masses change in a medium at finite temperature and finite density. As mentioned above, quark-antiquark pairs are condensed in the standard QCD vacuum. However, in environments of high temperature, such as the universe immediately after the Big Bang, or high density, such as the interior of a neutron star, the amount of condensation decreases, and chiral symmetry begins to recover. Consequently, it is known that the mass of hadrons at finite temperature and finite density differs from their mass under normal vacuum[1, 2, 3, 4]. We confirm this using a simple NJL model with two-flavor chiral symmetry $SU(2)_L \times SU(2)_R$.

$$\mathcal{L}_{NJL} = \bar{q}(i\gamma_\mu \partial^\mu - m)q + G\left[(\bar{q}q)^2 + (\bar{q}i\gamma^5\tau^a q)^2\right] \tag{1.5}$$

This is its Lagrangian. The distribution function can be expressed in terms of path integrals as follows.

$$Z_0 = \int \mathcal{D}\bar{q}\mathcal{D}q \exp\left[i\int d^4x \left[\bar{q}(i\gamma_\mu \partial^\mu - m)q + G\left[(\bar{q}q)^2 + (\bar{q}i\gamma^5\tau^a q)^2\right]\right]\right] \tag{1.6}$$

Extend this to a finite temperature and a finite density. The temperature β is introduced by introducing an imaginary time $\tau = t_f - t_i = -i\beta\hbar$ and the density is

treated by introducing a chemical potential μ.

$$Z_G = \int \mathcal{D}\bar{q}\mathcal{D}q \exp\left[\int_0^\beta d\tau \int d^3x \left[\bar{q}(-\gamma_0\frac{\partial}{\partial\tau} + i\gamma\cdot\nabla - m + \gamma_0\mu)q \right.\right. \\ \left.\left. + G[(\bar{q}q)^2 + (\bar{q}i\gamma^5\tau^a q)^2]\right]\right] \tag{1.7}$$

We then assume a quark-antiquark pair $\langle\bar{q}q\rangle$ as the mean field and perform the mean field approximation $(\bar{q}q)^2 \sim 2\bar{q}q\langle\bar{q}q\rangle - \langle\bar{q}q\rangle^2$. The distribution function is then as follows.

$$Z_G = \int \mathcal{D}\bar{q}\mathcal{D}q \exp\left[\int_0^\beta d\tau \int d^3x \left[\bar{q}(-\gamma_0\frac{\partial}{\partial\tau} + i\gamma\cdot\nabla - M + \gamma_0\mu)q - \frac{(M-m)^2}{4G}\right]\right] \tag{1.8}$$

Here, $M = m + 2g\langle\bar{q}q\rangle$, which can be treated collectively as a single mass term. What is happening, in other words, is that the introduction of a condensed mean field of quark-antiquark pairs has made the effective mass of quarks dependent on that mean field, and moreover, hadrons composed of such quarks will have more mass than the bare mass sum of quarks and that its origin is a mean field introduced by assuming the condensation of quark-antiquark pairs caused by the spontaneous breaking of chiral symmetry. The thermodynamic potential is then obtained from this distribution function. The thermodynamic potential is obtained as follows.

$$\Omega = -\frac{T}{V}\log Z_G \tag{1.9}$$

Furthermore, since the differentiation of the thermodynamic potential by the quark mass m leads to the expectation value of the quark-antiquark pair condensation, it follows that

$$\frac{d\Omega}{dm} = \langle\bar{q}q\rangle = \langle\bar{q}q\rangle + \frac{\delta\Omega}{\delta M}\frac{\partial M}{\partial m} \tag{1.10}$$

$$\frac{\delta\Omega}{\delta M} = 0 \tag{1.11}$$

Then, this equation can be followed.

$$\frac{\delta\Omega}{\delta M} = -2N_f N_C \int \frac{d^3p}{(2\pi)^3}\left(ME_p^{-1} + \frac{-ME_p^{-1}e^{-\beta(E_p-\mu)}}{1+e^{-\beta(E_p-\mu)}} + ME_p^{-1} \right. \\ \left. + \frac{-ME_p^{-1}e^{-\beta(E_p+\mu)}}{1+e^{-\beta(E_p+\mu)}}\right) + \frac{M-m}{2G} \tag{1.12}$$

$$M = m + 4GN_f N_C \int \frac{d^3p}{(2\pi)^3}\frac{M}{E_p}[1 - n_F^-(E_p) - n_F^+(E_p)] \tag{1.13}$$

Solving this for M yields the effective mass of quarks in the mean-field at finite temperature and finite density.

$$n_F^{\pm} = \frac{1}{1 + e^{-\beta(E_p \pm \mu)}} \tag{1.14}$$

In practice, numerical calculations show the following temperature and chemical potential dependence of M. Thus, the effective mass M of the quark varies with the

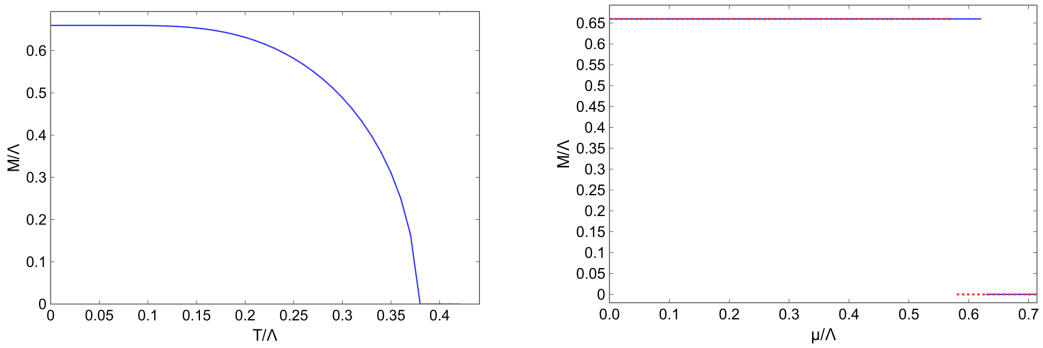

Figure 1.1: Temperature (left) and chemical potential (right) dependence of M.

amount of the mean field $\langle \bar{q}q \rangle$ at a finite temperature and a finite density. Whereas M continuously decreases with increasing temperature, it changes discontinuously with increasing chemical potential. Therefore, the chiral phase transition is a crossover phase transition with respect to temperature, whereas it is a first-order phase transition with respect to chemical potential. Furthermore, the form of the thermodynamic potential is checked. For example, if the temperature is fixed at 0 and the chemical potential is moved, we get the following. By the way, this is often

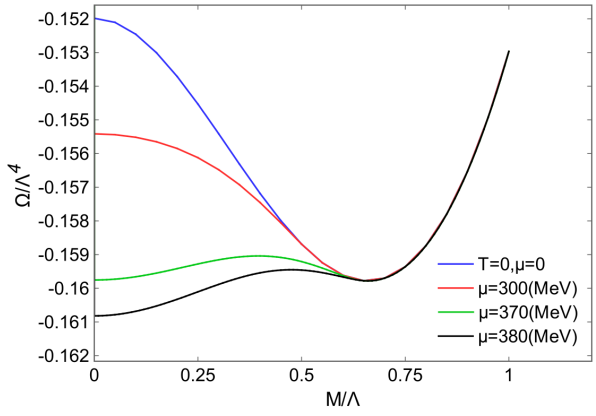

Figure 1.2: Chemical potential dependence of thermodynamic potential.

represented three-dimensionally in terms of the π meson field and the σ meson field as follows. The x-axis is the effective mass of the quark M normalized by *Lambda*,

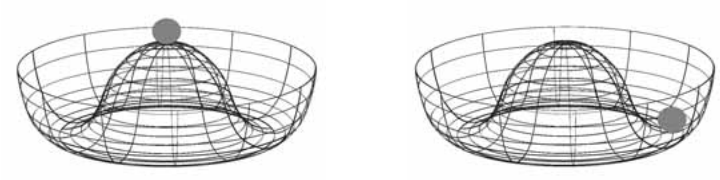

Figure 1.3: 3D diagram of the thermodynamic potential. In order for the vacuum to become stable, the vacuum is realised not at the centre of the potential, but at the bottom of the slope rolling downhill. This is the concept of symmetry breaking.

where $M = m + 2\langle\bar{q}q\rangle$. The blue line with zero temperature zero density usually represents vacuum, and the thermodynamic potential is more stable if the mean field $\langle\bar{q}q\rangle$ takes a finite value rather than zero. This is the spontaneous breaking of the chiral symmetry. As the chemical potential increases, the peak on the left side gradually decreases and eventually takes the lowest pole. This is the chiral phase transition.

1.1.3 Chiral Partner

Noether's theorem in quantum field theory, as in analytical mechanics, states that when the Lagrangian density has a symmetry, there is a corresponding conserved quantity. The conserved quantity corresponding to the chiral symmetry is expressed as follows

$$\partial_\mu J_5^\mu = 2im\bar{\psi}\gamma^5\psi,\ j_5^\mu = \bar{\psi}\gamma^\mu\gamma^5\psi \tag{1.15}$$

The quark field also has $U(1)$ symmetry and thus conserves the following quantities in a similar way.

$$\partial_\mu J^\mu = 0,\ J^\mu = \bar{\psi}\gamma^\mu\psi \tag{1.16}$$

Here, $U(1)$ symmetry is the symmetry for transformations such that

$$\psi \to e^{-i\alpha}\psi \tag{1.17}$$

In the chiral limit ($m \to 0$), QCD has chiral symmetry, and the chiral symmetry current is conserved as follows.

$$J^{\mu}_{R,L} = \bar{\psi}\gamma^{\mu}\frac{1 \pm \gamma^5}{2}\psi = \bar{\psi}_{R,L}\gamma^{\mu}\psi_{R,L},\ \partial_{\mu}J^{\mu}_{R,L} = 0 \tag{1.18}$$

The conserved charge $Q_{V,A}$ is defined by integrating the time components of the conserved current. Among the chiral transformations, Q_V and Q_A are the conserved charges corresponding to the polar and axial transformations, respectively, and take the form of the sum or difference of the number of right- and left-handed quarks, as follows.

$$Q_{R,L} = \int d^3x J^0_{R,L} = \int d^3x \psi^{\dagger}_{R,L}\psi_{R,L},\ Q_V = Q_R + Q_L,\ Q_A = Q_R - Q_L \tag{1.19}$$

$Q_{V,A}$ has the following exchange relationship with the parity operator.

$$PQ_VP^{-1} = Q_V,\ PQ_AP^{-1} = -Q_A \tag{1.20}$$

Now consider a particle with eigenvalues of mass M and parity π. In other words, if we let the parity operator act on that particle state, we get the eigenvalue π.

$$P|M,\pi\rangle = \pi|M,\pi\rangle \tag{1.21}$$

The conserved axial charge Q_A acts on this equation.

$$PQ_A|M,\pi\rangle = -Q_AP|M,\pi\rangle = -\pi Q_A|M,\pi\rangle \tag{1.22}$$

Then $Q_A|M,\pi\rangle$ can be considered a particle with the same mass and opposite parity as $|M,\pi\rangle$. This pair of $Q_A|M,\pi\rangle$ and $|M,\pi\rangle$ is called a chiral partner. However, when chiral symmetry is preserved, the chiral partner takes on such a state, but in a vacuum where chiral symmetry is broken, the chiral partner has a different mass. This property is also important in experiments: if we can experimentally observe that the spectral function (mass or width) of the chiral partner is degenerate in a finite temperature, finite density medium, we can prove that the chiral symmetry has been restored and that the hadron mass has changed accordingly, i.e. that the hadron mass has changed in accordance with the chiral symmetry breaking The mass of the hadron is produced by the breaking of the chiral symmetry.

1.1.4 SU(3) Flavor Symmetry Breaking

In the chiral limit, the vector mesons are split into flavor SU(3) octets and a singlet. In reality, however, the mass of the s-quark is very large compared to the u,d quarks and the SU(3) flavor symmetry is broken. As a result, the octet and singlet components mix.

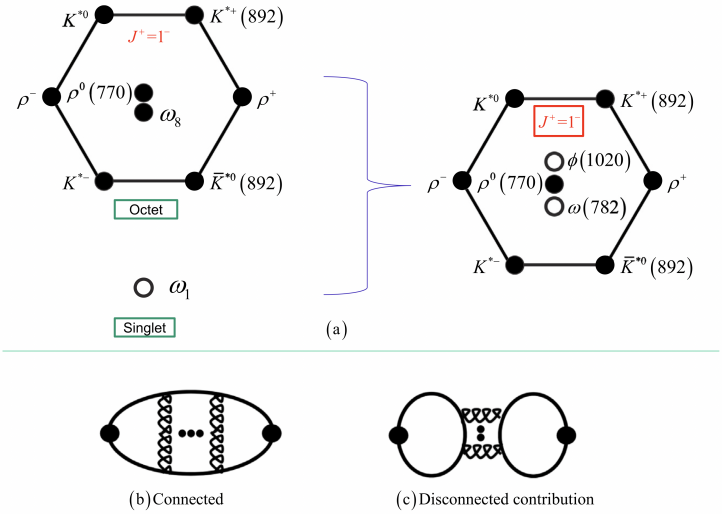

Figure 1.4: (a):In the chiral limit, the vector mesons are split into octets and singlets (left), but in practice the octets and singlets mix (right) because the s-quarks are heavy SU(3) and flavor symmetry is broken. (b):connected diagram, which only contributes to the octet component. (c):disconnected diagram, which contributes to the singlet component and mixes octet and singlet components. [5, 6]

Then, in the chiral limit, the axial vector mesons that are chiral partners of the octet and the singlet of the vector meson are as shown in Fig 1.5, but there is no chiral partner for the singlet while there is a corresponding chiral partner for the octet component [5, 6].

However, it is known from lattice QCD calculations that the contribution of the disconnected diagram is relatively small [7], and it is still significant to measure the ω, ϕ and f_1 mesons as approximate chiral partners. However, it should be noted that lattice QCD results are calculations at finite temperature only, and it is non-trivial what happens at finite density.

1.1.5 Parity Doublet Model

Next, we shall explain how chiral partners undergo mass changes and degenerate along with the restoration of chiral symmetry, using a simple parity doublet model

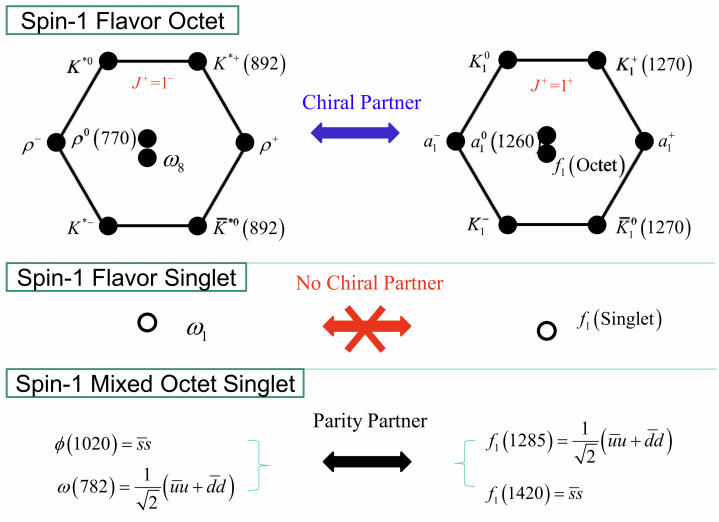

Figure 1.5: Vector meson octet and singlet chiral partners. The octet component has a chiral partner, but the singlet component has no chiral partner. Therefore, K mesons and ρ mesons made of octets only have corresponding chiral partners, but ω mesons and ϕ mesons made of mixed octets and singlets do not strictly have chiral partners and have parity doublets.

for understanding. For any baryon fields N_1 and N_2, applying a chiral transformation yields the following transformation.

$$N_{1L} \to LN_{1L},\ N_{1R} \to RN_{1R} \tag{1.23}$$

$$N_{2L} \to RN_{2L},\ N_{2R} \to LN_{2R} \tag{1.24}$$

At this point, a mass term that does not break the following chiral symmetry can be written.

$$-m_0(\bar{N}_1\gamma_5 N_2 - \bar{N}_2\gamma_5 N_1) \tag{1.25}$$

This mass m_0 is called the chiral invariant mass. Other terms that may contribute to the mass include the interaction term between the scalar field σ and the baryon. This is expressed as follows.

$$-g_1\bar{N}_1\sigma N_1 - g_2\bar{N}_2\sigma N_2 \tag{1.26}$$

σ corresponds to $\bar{q}q$ and takes its expectation value in the vacuum state. That is, σ is an order parameter for chiral symmetry and assumes a non-zero value when chiral symmetry undergoes spontaneous breaking.

$$\langle\sigma\rangle = \sigma_0(\simeq f_\pi \sim 93\,\text{MeV}) \tag{1.27}$$

Consequently, the interaction term between the σ field and baryons becomes a mass term, and the two-component mass matrix can be written as follows by choosing an appropriate basis:

$$\mathcal{L}_{\text{mass}} = -(\bar{N}_1, \bar{N}_2) \begin{pmatrix} g_1\sigma_0 & m_0\gamma_5 \\ -m_0\gamma_5 & g_2\sigma_0 \end{pmatrix} \begin{pmatrix} N_1 \\ N_2 \end{pmatrix} \tag{1.28}$$

In this basis, the mass matrix is mixed rather than diagonal and N_1 and N_2 are not mass eigenstates. By diagonalising the mixture (taking eigenvalues and eigenvectors), the following combinations are obtained, which are the mass eigenstates.

$$\begin{pmatrix} N_+ \\ N_- \end{pmatrix} = \begin{pmatrix} \cos\theta & \gamma_5\sin\theta \\ -\gamma_5\sin\theta & \cos\theta \end{pmatrix} \begin{pmatrix} N_1 \\ N_2 \end{pmatrix} \tag{1.29}$$

However, the mixing angle θ can be expressed as $\tan 2\theta = 2\mathrm{m}_0/(\mathrm{g}_1 - \mathrm{g}_2)\sigma_0$. The eigenvalues are as follows.

$$M_\pm = \frac{1}{2}\left[(g_1 + g_2)\sigma_0 \pm \sqrt{(g_1 - g_2)^2\sigma_0^2 + 4m_0^2}\right] \tag{1.30}$$

This is the mass that is actually observed. If the vacuum preserves chiral symmetry, then $\langle\sigma\rangle = 0$, $\langle\bar{q}q\rangle = 0$, and all masses originate from m_0, so $m_{N_+} = m_{N_-} = m_0$. This state represents the degenerate mass of the chiral partners. However, in a normal vacuum, the chiral symmetry is spontaneously broken, so $\langle\sigma\rangle \neq 0$, and the chiral partners possess different masses.

1.2 Situation of Experiments

In this section, the status of the experiments that reveal the relationship between hadron masses and spontaneous breaking of chiral symmetry is summarized.

In the history of accelerators, they have evolved to reach ever higher energies, and in the field of nuclear physics, high-energy heavy-ion collisions have successfully produced QGPs (quark gluon plasmas). The temperature evolves with time, but the QGP is not a matter of time. The temperature of the QGP reaches about the chiral phase transition temperature, which evolves with time, so that spontaneous chiral symmetry breaking is expected to be restored inside the QGP. Therefore, several experiments have challenged the comparison of the spectral function of hadrons in a high-temperature medium such as QGP with that of normal vacuum[8, 9, 10, 11]. Similar experiments have also been performed in fixed-target experiments and in

dense medium with deliberate baryon stopping, which has attracted much attention in recent years. Some examples are given below.

1.2.1 CERES/NA45 as a Finite Temperature Region

For example, below are the results of electron pair measurements from the CERES/NA45 experiment at SPS, where the NA45 experiment is dedicated to electron pair measurements using two ring image Cherenkov detectors. Comparison of the electron pair invariant mass distribution for lead-gold collisions with a scaled proton-proton collision distribution shows that the ρ meson peak (770 MeV) disappears and an enhancement is observed around the lower 300-500 MeV region [12]. In other words, the ρ meson spectrum changed drastically, and it was noticed that this might be a signal of chiral symmetry restoration in a high-temperature medium. In the 200-600 MeV mass region, the increase factor for the proton-proton distribution was 2.7. The ρ mass distribution is better reproduced by an increase in the width of the ρ mass distribution due to the $\pi\pi \rightarrow \rho$ reaction than the model of ρ mass reduction [13] due to chiral symmetry restoration, and the link to chiral symmetry is open.

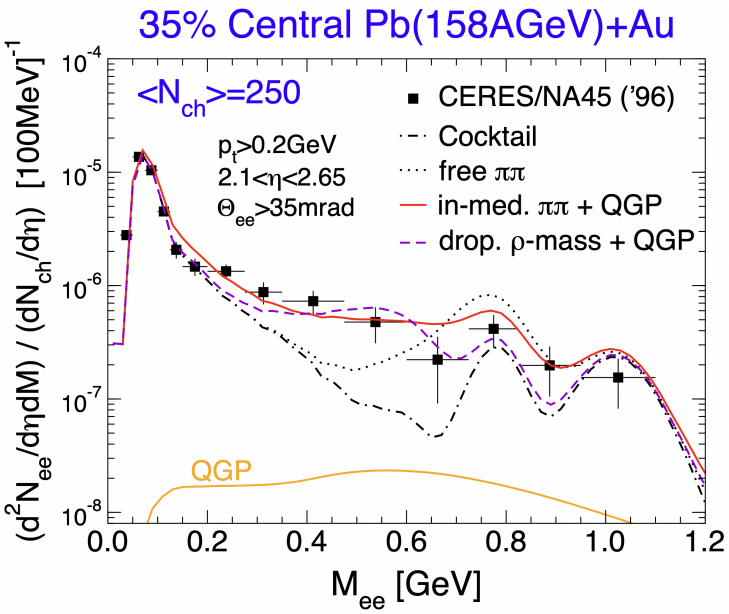

Figure 1.6: Electron pair invariant mass distribution measured in Pb(158AGeV)+Au collisions in the CERES/NA45 experiment [12]. The purple dashed line is a calculation assuming mass dropping due to chiral symmetry restoration of ρ mesons by BR scaling, while the red solid line is a calculation incorporating hadron interactions such as $\pi\pi \rightarrow \rho$, so-called collision broadening, etc., which does not include the effect of chiral symmetry restoration.

Thus, many experiments have been successful in capturing changes in hadron mass in the medium, but the biggest challenge in this research field is the inability to distinguish whether the changes are due to the restoration of chiral symmetry or to the interaction between the hadron and the medium.

1.2.2 NA60 as a Finite Temperature Region

The NA60 experiment measured low-mass muon pairs in In-In collisions at 158 AGeV. This experiment also showed a deformation from the normal vacuum distribution, but unlike the NA45 results, it was not consistent with dropping ρ [10]. One of the challenges in this research field is that different experiments produce different scenarios, some favoring mass dropping, others favoring broadening, etc.

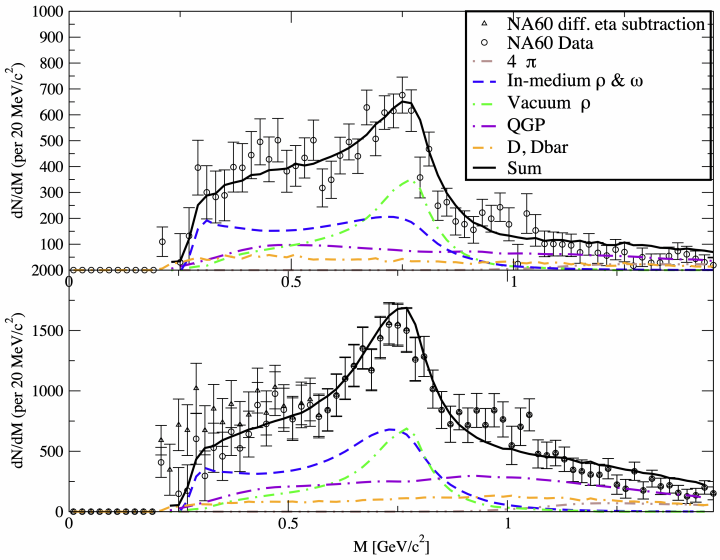

Figure 1.7: Invariant mass distribution of muon pairs measured in the NA60 experiment [10]. The data are well explained by the hadronic many-body effect even without chiral symmetry restoration. On the other hand, a structure is visible around 1 GeV that cannot be explained by it. This could be the A_1 meson, the chiral partner of the ρ meson, although it cannot be definitive due to large errors.

The experimental results are to some extent neatly explained by the hadronic many-body effect, even without any mass change, etc [10]. associated with the restoration of chiral symmetry. There is also a structure around 1 GeV that is not found in the theoretical model. It is not clear whether this is an error or due to hadronic decay not taken into account in the theoretical model, but one possibility is that the a_1 meson, the chiral partner of the ρ meson, may have been visible. If this is indeed the a_1 meson, it would be nice to confirm that the mass difference with the ρ meson is reduced, but it is hard to say from this result.

1.2.3 KEK-PS E325 as a Finite Density Region

KEK-PS E325 experiment uses nuclei as the medium, rather than a high-temperature medium like QGP. Although nuclei are very dense, temperature effects can be largely neglected because thermal equilibrium cannot be defined. KEK-PS E325 experiment is similarly dedicated to electron pair measurements, especially the spectrum of the ϕ meson, which has a narrow width and relatively few interactions with the medium[14, 15, 16].

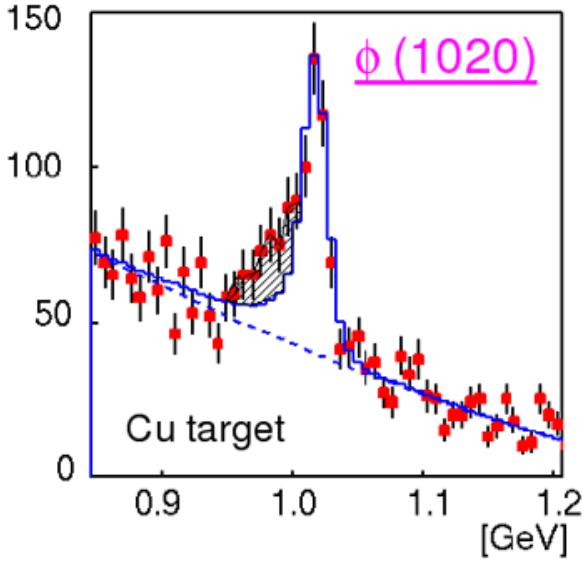

Figure 1.8: Electron pair invariant mass distribution measured by the KEK-PS E325 experiment[16]. The blue line is the Breit-Wigner distribution of ϕ mesons in normal vacuum. The measured data (red) has an excess compared to that distribution, suggesting that the partial restoration of chiral symmetry in the nucleus may have lightened the ϕ mesons that decayed in the nucleus and created such a tail.

In the E325 experiment, an exccess was observed for the Breit-Wigner distribution of ϕ mesons [14, 15, 16], as shown in Figure1.8. It has been suggested that some ϕ mesons may have been lightened by decaying in nuclei with partially recovered chiral symmetry. However, even though the interaction of ϕ mesons composed of s quarks with nucleons composed of u,d quarks is largely suppressed by the OZI rule, recent femtoscopy experiments have shown that they cannot be neglected, as discussed in the next section1.2.4. Therefore, the challenge is that it is not possible to discern from this alone whether this experimental result is also a mass change of the *phi* meson associated with the restoration of chiral symmetry or a mass change due to the ϕ-N interaction. This applies not only to the ϕ meson, but also to the ρ and ω mesons [17, 18, 19, 20, 21]. Ultimately, the challenge facing the entire field is that, while the transformation of the distribution of the lepton mass is understood,

it remains uncoupled from the origin of the hadron masses [22, 23, 24, 25].

Furthermore, results from other experiments, such as the JLab CLAS experiment, did not observe any mass change of the ρ, ω, ϕ meson within the nucleus[26]. In the CBELSA-TAPS experiment, as in the JLab CLAS experiment, no significant mass shift of the ω meson was observed[27]. Thus, the lack of consistency between several experiments also presents a challenge.

1.2.4 ϕ-N Interaction

The deformation of the mass spectrum of vector mesons in high-temperature, dense medium compared to that in normal vacuum has been confirmed in many experiments, although the deformation varies from experiment to experiment. In order to conclude that this deformation is associated with a partial restoration of chiral symmetry, the contribution of other effects to the deformation of the mass distribution must be known. One of the most important contributions is the hadronic many-body effect, i.e. the interaction of vector mesons with the medium, as confirmed, e.g. in CERES/NA45. In particular, there are many pions and nucleons consisting of light u,d quarks, and it is necessary to know about the mass and width changes due to the interaction of these with vector mesons. By the way, ϕ mesons are composed of $s\bar{s}$, so their interactions with nucleons and pions are largely suppressed by the OZI rule. Therefore, it has been thought that the interaction between ϕ mesons and nucleons in nuclei is small when nuclei are used as the medium, as in the KEK-PS E325 experiment. However, recently, the p-ϕ correlation function has been measured by femtoscopic experiments (Fig1.9) [28].

The p-ϕ correlation function measured in the CERN ALICE experiment suggests an attractive interaction between the two particles [28]. Furthermore, it was confirmed that this result agrees well with the lattice QCD results from the HAL QCD Collaboration [29]. However, since the ALICE measurement includes both both spin-1/2 and spin-3/2 components, while the HAL QCD result only concerns spin-3/2, a direct comparison is not possible. Moreover, the ALICE and HAL QCD results yield relatively long scattering lengths, which contrasted with many hadronic models and the QCD sum rule results discussed later [30]. Therefore, research is required to reconcile the experimental results with the theory (some first step of such works can be found in Refs. [31, 32]). ALICE's result means that it is not the tree level, but the higher-order loop diagrams that create such attraction. Attractive interactions cause negative mass shifts and broadening of widths. Therefore, it must be taken into account whenever the mass shift or width change of a vector meson is discussed

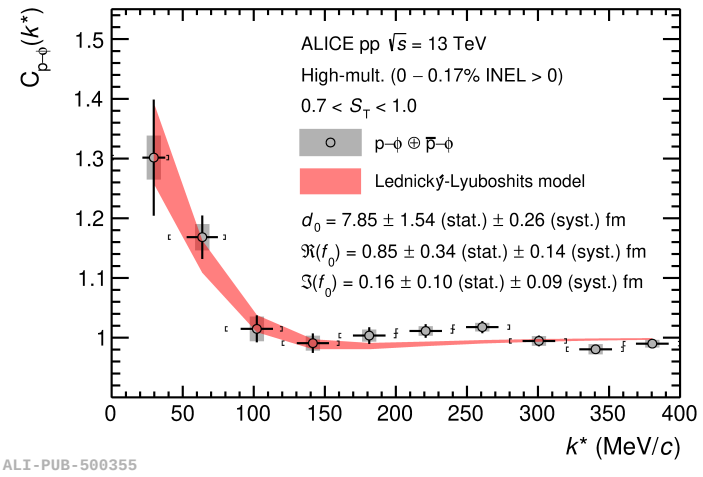

Figure 1.9: The p-ϕ correlation function measured in the CERN ALICE experiment. Attractive interactions were confirmed [28].

in the mass distribution. Many theoretical models have calculated the self-energy of ϕ mesons in a medium with N-*phi* interactions, but it was difficult to determine how high-orderterms should be considered. Recently, however, the p-ϕ correlation function has been experimentally measured, and if the self-energy can be calculated on this basis, the effect of the interaction between the ϕ meson and the medium on the mass distribution can be estimated with high confidence. Therefore, many theoretical studies are currently being carried out.

QCD sum rule

Unlike hadronic models, the QCD sum rule approach relates the integrals of hadron spectral functions to the expectation values of QCD operators, some of which are order parameters for chiral symmetry. Recent QCD sum rule studies indicate that the mass shift of the ϕ meson strongly depends on the strangeness sigma term $\sigma_{sN} = m_s\langle N|\bar{s}s|N\langle$. σ_{sN} is the parameter that governs the restoration of chiral symmetry in the strange quark sector within the linear density approximation. Furthermore, QCD sum rule studies predict that if σ_{sN} is less than 35 MeV, the ϕ meson exhibits a small but positive mass shift, whereas increasing σ_{sN} leads to a corresponding negative mass shift[33]. Combining this result with recent lattice QCD calculations of σ_{sN} ($\sigma_{sN} = 52.9(7.0)MeV$ [?]) predicts a very small negative mass shift of approximately 5 MeV at nuclear density.

1.2.5 Pionic Atom

The pionic atom is a different experiment from previous experiments, in which $\bar{q}q$, the order parameter for spontaneous breaking of chiral symmetry, is measured in the atomic nucleus. The pionic atom is a normal atom with electrons bound around the nucleus, but instead of electrons, pions are bound. pions are much heavier than electrons, so they have a much lower orbital energy than electrons. Because pions are much heavier than electrons, they are bound to a more inner orbital, and the pions feel the density of the nucleus. By measuring the X-ray transition energy of the pionic atom, the scattering length of π-N is obtained.

$$\epsilon_{1s} \propto \mathrm{Re}(V_{\pi N}) \sim \rho \cdot b_1 \tag{1.31}$$

Here ρ is the density and b_1 is the scattering length. The Tomozawa-Weinberg relation is then used to relate the scattering length to the pion decay constant f_π.

$$b_1(\rho) \propto \frac{1}{f_\pi^2(\rho)} \tag{1.32}$$

Furthermore, the low-energy theorem and the Gell-Mann-Oakes-Renner relation allow for the following.

$$f_\pi^2(\rho) \propto \langle \bar{q}q \rangle_\rho \tag{1.33}$$

It can be associated with the By measuring the change in the scattering length b_1 with respect to the density ρ, one can estimate the degree of chiral symmetry restoration in normal vacuum and finite density. Specifically, the linear density approximation often holds and is analyzed using the following equation.

$$\frac{\langle \bar{q}q \rangle_\rho}{\langle \bar{q}q \rangle_{\mathrm{vac}}} \sim 1 - C \cdot \frac{\rho}{\rho_0} \tag{1.34}$$

Experiments on pionic atoms suggest that chiral symmetry is restored by about 40% in nuclear density in the u,d sector [34].

This makes it almost certain that chiral symmetry is partially recovered in finite densities. It now remains to be verified whether there is a relationship between the spontaneous breaking of the chiral symmetry and the hadron mass.

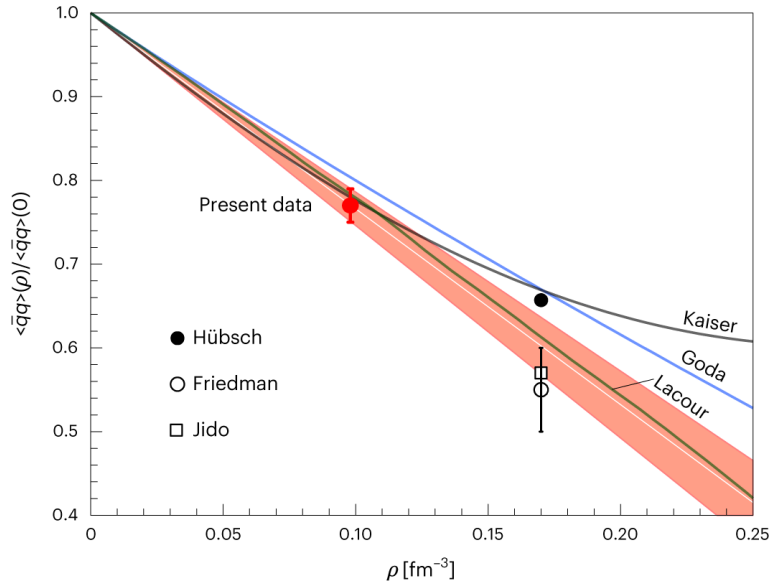

Figure 1.10: Experimental results and some theoretical predictions for pionic atoms performed at RIKEN RIBF. Experimental results suggest that chiral symmetry is recovered by about 40% at nuclear density ρ_0 if linear density approximation holds [34].

1.3 J-PARC E16 Experiment

The J-PARC E16 experiment[35] is a follow-up to the KEK-PS E325 experiment, with the primary objective of systematically measuring the deformation of the mass spectrum of ϕ mesons in nuclear density.

1.3.1 Setup

J-PARC

J-PARC is a proton accelerator located in Tokai Village, Ibaraki Prefecture, Japan. The proton beam reaches the Hadron Hall after passing through three accelerator stages: the LINAC, RCS, and MR. The LINAC is a linear accelerator that accelerates protons up to 400 MeV. The RCS is a synchrotron accelerator that further accelerates the protons from the LINAC up to 3 GeV. The MR is a synchrotron accelerator that accelerates the protons from the RCS up to 30 GeV. The proton beam accelerated in the MR is delivered to the Hadron Hall, where it is further split into three beams: the A line, B line, and C line. The proton beam from the B line is then directed to the target for the J-PARC E16 experiment. Approximately 0.1% of the proton beam is diverted into the B line by a dipole magnet known as the Lambertson magnet (Figure 1.13)[36]. The Lambertson magnet has regions with and without magnetic fields,

separated by magnetic poles. Only the portion of the beam in the vertical direction passes through the region with a magnetic field, causing the beam to diverge and be transported to the B line. This enables the extraction of a high-momentum proton beam at 30.9 GeV/c and a high intensity of 1 $\times 10^{10}$/spill (a spill lasts approximately 2 seconds).

Figure 1.11: J-PARC accelerator is consist from LINAC, RCS, and MR.

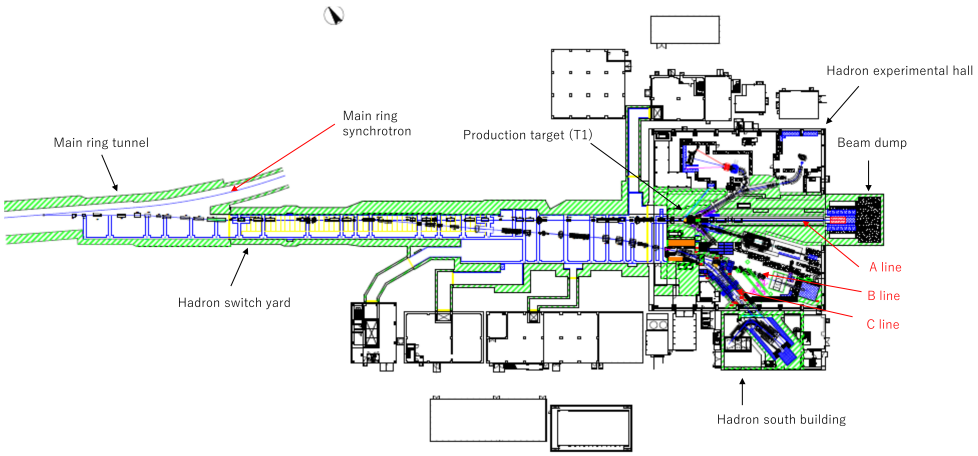

Figure 1.12: Hadron hall

Target

This experiment employs CH2, C, Cu, and Pb as targets. The use of several target types is intended to systematically verify density effects by varying the nuclear radius. Furthermore, to suppress broadening effects such as electron production via π^0 Dalitz decay or gamma conversion within the target, and scattering between

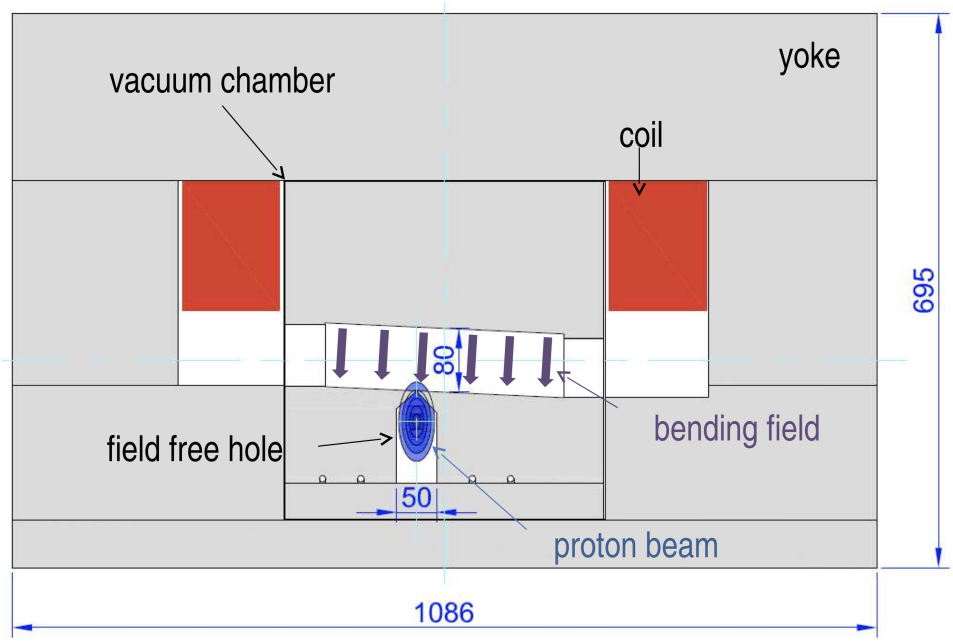

Figure 1.13: Beam splitting method using the Lambertson electromagnet[36]. The magnetic field is applied in the direction of the arrows. The ellipses represent beam sizes of 1σ, 2σ, 3σ, and 4σ.

electron pairs and nuclei within the target, the target thickness must be extremely thin, approximately 0.5% of the radiation length. Consequently, while the KEK-PS E325 experiment, with its lower beam intensity, could not utilize a Pb target, the J-PARC E16 experiment, which can achieve high-intensity beams, can employ it. For the Run0-e data analyzed here, two C targets and one Cu target were used. To avoid reducing the yield, the three targets were aligned in a straight line along the beam path and irradiated simultaneously (Figure 1.14).

Spectrometer

The E16 experiment's spectrometer comprises four types of detectors, whose roles are divided into tracking and electron identification. Tracking is performed by the Silicon Strip Detector (SSD) and GEM Tracker (GTR), while electron identification is handled by the Hadron Blind Cherenkov Detector (HBD) and Lead-Glass Calorimeter (LG). To achieve a momentum resolution of 5 MeV/c for tracking, a position resolution of 100 μm in the x-direction and 700 μm in the y-direction is required. Past test experiments have confirmed that this resolution is achievable[37, 38]. Furthermore, the GTR achieves this position resolution even for oblique incident angles of 0–30 degrees, enabling it to detect electrons with momenta down to 0.2 GeV/c. Additionally,

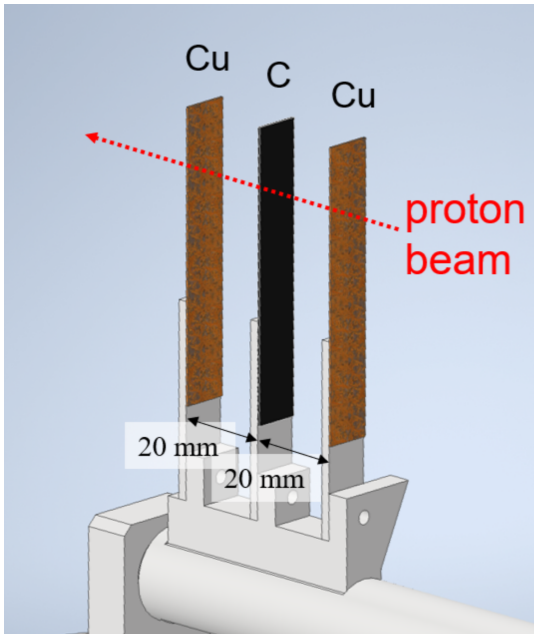

Figure 1.14: Target placement. In Run0e, they were arranged along the beam axis in the order Cu, C, Cu.

it has been confirmed that the two detectors responsible for electron identification meet the requirement to reject background charged pion mesons at 99.8% online and 99.97% offline, maintaining an electron detection efficiency of 57%[39, 40]. In Run0e, the E16 experiment's spectrometer comprises eight modules. Each module consists of a set containing the Silicon Strip Detector (SSD), GEM Tracker (GTR), Hadron Blind Cherenkov Detector (HBD), and Lead-Glass Calorimeter (LG). Each module is assigned a name. As shown in Figure 1.15, modules numbered 101 to 104 are arranged along the right arm, while modules numbered 106 to 109 are arranged along the left arm. A single module covers a range of ±15 degrees vertically and ±12 to 14 degrees horizontally.

Dipole magnets are positioned to sandwich the spectrometer from above and below, with charged particles passing through the spectrometer along the magnetic field. The magnetic field in the central region where the target is located is 1.77 T.

SSD

SSD is the innermost detector layer, a silicon-based tracking detector. SSD employs the Silicon Tracking System (STS)[41, 42] intended for use in the GSI FAIR CBM experiment, which consists of a single detection surface.

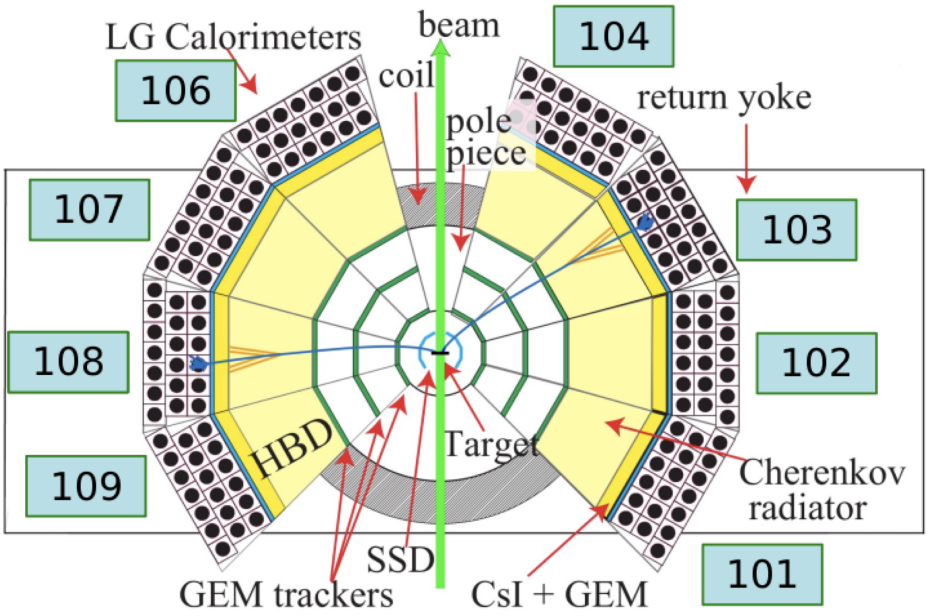

Figure 1.15: Top view of the E16 spectrometer (x-z plane). The beam passes through the paper facing upwards. The target is positioned centrally, with detectors arranged in order of proximity to the target: SSD, GTR, HBD, LG. The numbers 101 to 109 denote the names of each module.

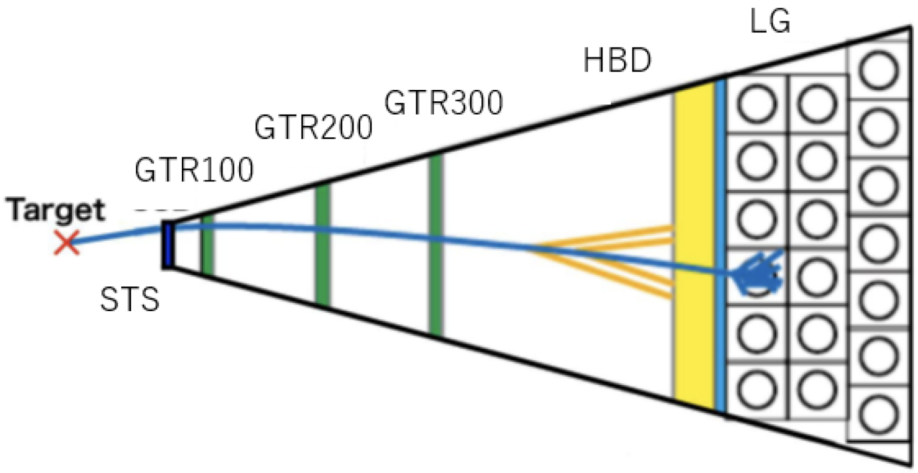

Figure 1.16: Module external view.

GTR

GTR is the main tracker for the E16 spectrometer using GEM[43]. Within a single module, the GTR comprises three layers of GTR chambers: GTR-100, GTR-200, and GTR-300. The numerical designation, such as 100, indicates the size of the detection surface for each chamber. For example, 100 denotes a chamber with a detection surface of 100 mm×100 mm. Each GTR chamber has a layered structure comprising, in the order shown in Figure 1.17, Myler, MESH, GEM1, GEM2, GEM3, and Readout Strip Foil.

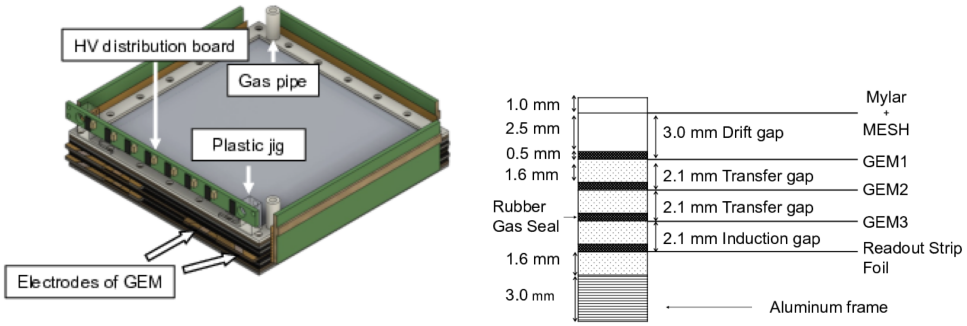

Figure 1.17: Module external view.

Each GEM had a voltage applied to its front and rear surfaces. Although the operating voltage varied depending on the GEM's state, it was typically maintained at approximately 380 to 400 volts. This voltage intensified the electric field locally within the small holes opened in the GEM, enabling the amplification of ionized electrons. Furthermore, a voltage is applied between the MESH and GEM1. The 3 mm space between the MESH and GEM1 is termed the drift gap, and the voltage applied across this gap is called the drift voltage. This drift voltage also varies depending on the chamber's state, but a high voltage such as 1200 V/cm is applied. This drift electric field causes the ionized electrons to drift towards the GEM.

Each GEM is divided into several segments to minimize damage when the front and rear conduct due to discharge or similar events. For example, the GEMs in the GTR-300 are divided as follows: GEM1 and GEM2 are each divided into 12 segments, while GEM3 is divided into 24 segments. The reason why only GEM3 in the GTR-300 is divided into 24 segments, as will be explained later, is for the generation of the trigger signal.

The space between the Myler and the readout strip foil is filled with ArCO2 (70:30) at a pressure of 1 atm. Charged particles flying from the target ionize ArCO2 within

the GTR chamber. The resulting ionization electrons are amplified by three layers of GEM, and the signal flows from the readout strip foil to the readout circuit. The signal from the readout strip foil is sampled by a readout circuit called APV25 (Figure 1.18).

The GTR readout and trigger chain is organized into two linked paths: a continuous data path for strip waveform readout and a fast trigger path that enables event selection. In the data path, signals induced on the readout foil are processed by APV board(Figure 1.18), which performs analog shaping and 40 MHz sampling. The analog outputs of the APV are transmitted to the Scalable Readout System (SRS) (Figure 1.19), where the signals are digitized and transferred to the DAQ PC via UDP/IP for data acquisition and offline analysis. In parallel, a fast trigger signal is generated using charge signals induced on the rear side of the third GEM (GEM3) of the GTR300. These signals are fed into Analog Shaper Discriminator (ASD) boards (Figure 1.20), which provide shaped and discriminated outputs for trigger purposes. The ASD outputs are sent to a merger module, where coincidence logic is applied together with trigger signals from the LG and HBD detectors. When the coincidence condition is satisfied, a global trigger signal is issued and distributed to the readout system. Upon receiving this trigger, the buffered waveform data stored in the APV pipeline are read out through the SRS, completing the full GTR readout chain. This is why the GEM3 in the GTR300 is divided into 24 segments, finer than other GEMs.

On the detection plane of the GTR chamber, the lateral and longitudinal directions are referred to as local-x and local-y, respectively. The Readout Strip Foil is independent in both local-x and local-y, with matching performed during subsequent analysis.

Each GTR chamber is arranged as shown in Figure 1.21. As can be seen in Figure 1.21, the GTR chambers are arranged with modules closer to the target alternating with modules farther from the target. Modules positioned closer to the target are referred to as the A type, while those positioned farther from the target are referred to as the B type. Figure 1.22 shows the arrangement of the GTR chambers in the xy plane, with the GTR-100, 200, and 300 mounted on a CFRP frame. Although the GTR chambers can be mounted in three levels (upper, middle, and lower), only the middle level was mounted for Run0-e and subsequent Run1.

HBD

The HBD is a gas Cherenkov counter for electron identification[44]. CF4 gas is enclosed within an aluminum housing as the Cherenkov emitter, with a radiator

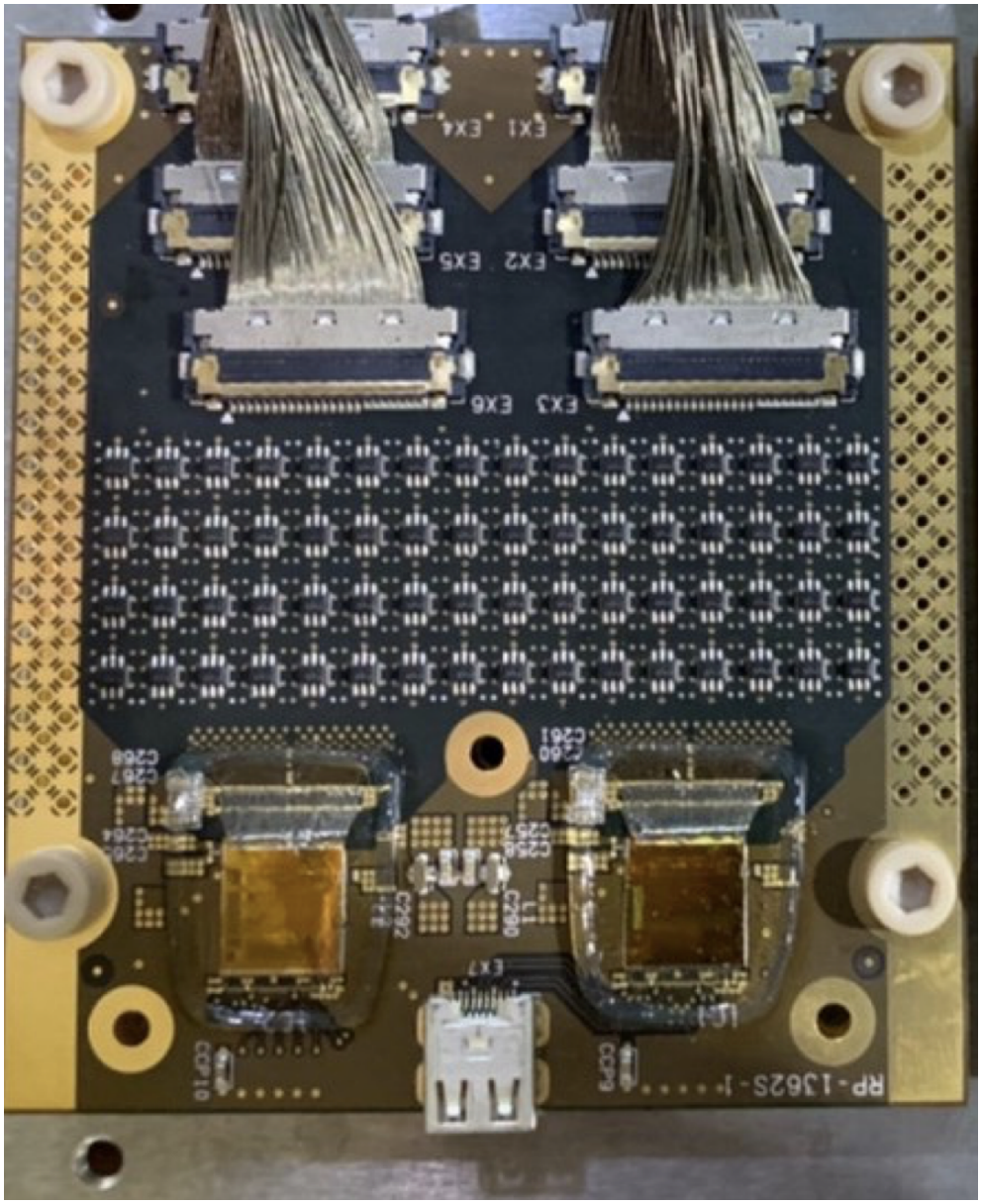

Figure 1.18: APV board. Signals are input via the coaxial cable connector at the top of the photograph and output via the HDMI port at the bottom.

Figure 1.19: Photograph of the SRS. The rear section of the crate contains the ADC card, while the FEC card is visible at the front.

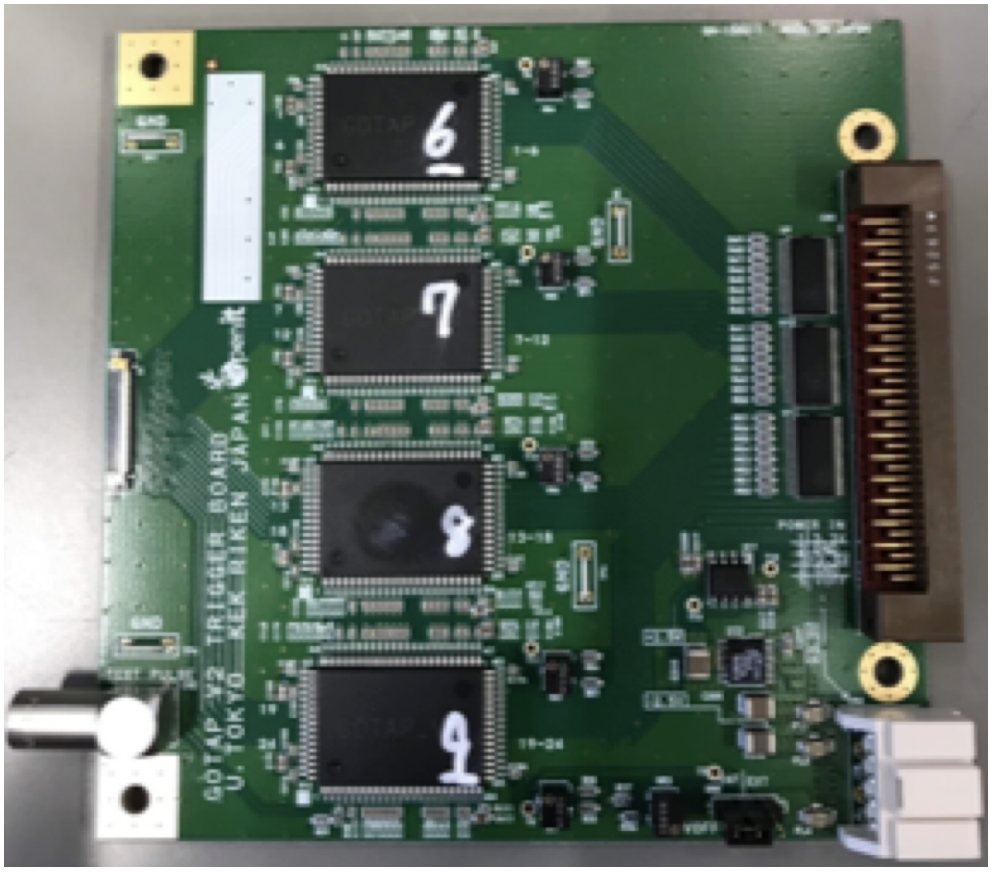

Figure 1.20: Photograph of an ASD board. Each ASD board carries four ASD chips.

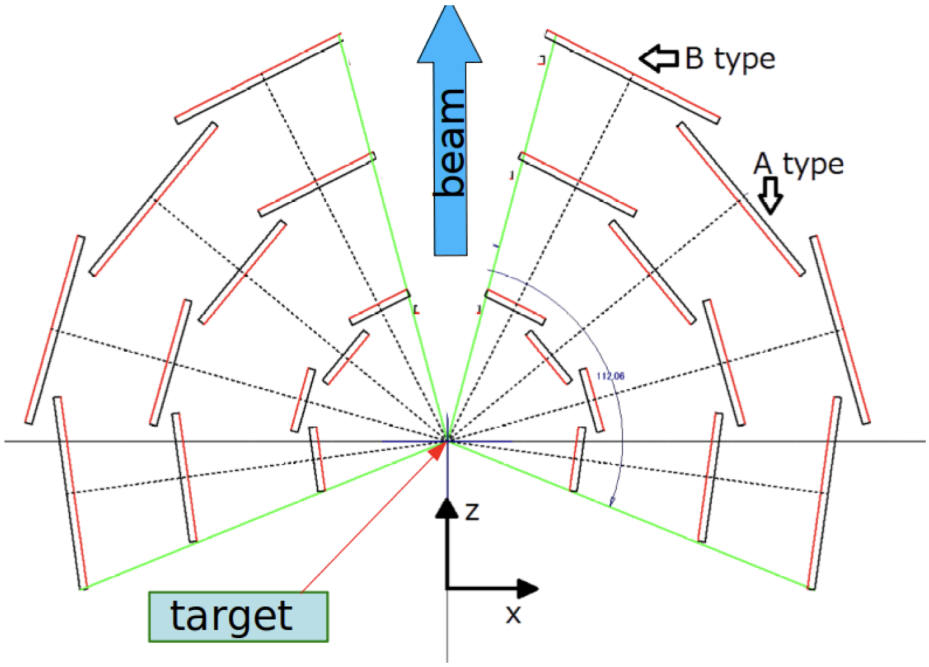

radius[mm]	STS	GTR100	GTR200	GTR300
A type	117	196	403	581
B type	148	239	452	638

Figure 1.21: Layout diagram of the GTR chamber. Viewed from the same orientation as Figure 1.15.

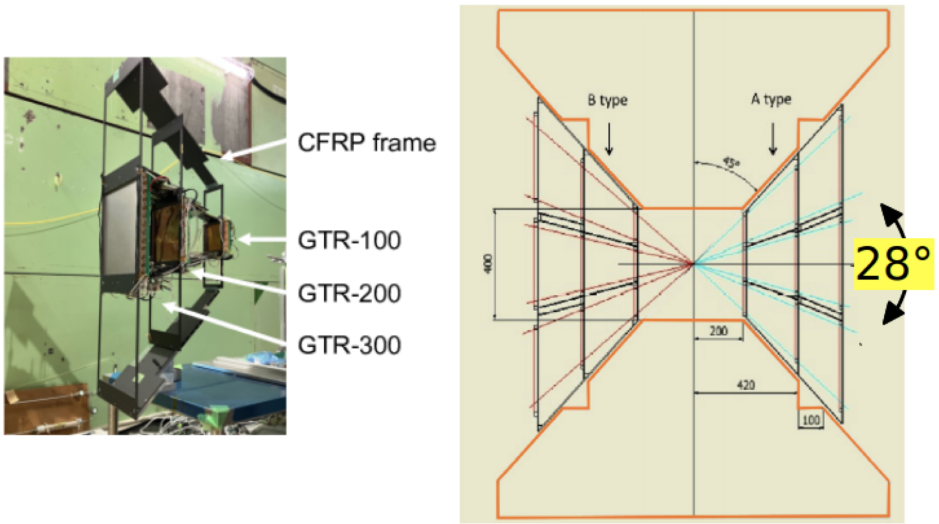

Figure 1.22: (Left) Photograph of the GTR module. The GTR-100, 200, and 300 are mounted in the middle section of the CFRP frame. (Right) Cross-sectional view of the GTR section in the xy plane within the spectrometer.

length of 500 mm in the local-z direction (perpendicular to the detection plane of each module, pointing outward from the target). Electrons passing through this 500 mm section of the HBD first emit Cherenkov light. However, hadrons such as pions are too heavy to produce Cherenkov light. Beyond this 500 mm section lies the LG-side face of the HBD, measuring 600 mm × 600 mm. This face houses the MESH, three layers of GEM, and the pad readout. The three layers of GEM each comprise four 300mm × 300mm GEMs. The surface of the first GEM is coated with CsI, which converts the Cherenkov light into photoelectrons. Furthermore, between the MESH and the first layer of GEM, an electric field is formed that causes electrons to drift towards the MESH side, contrary to the GTR. This is because charged particles ionize CF4 as they pass through the HBD; therefore, hadrons such as $\pi^{\pm}$ also generate ionizing electrons. Since such ionizing electrons are not desired for detection, an electric field is formed to create a drift direction towards the MESH to adsorb them. Photoelectrons generated in CsI are amplified through three layers of GEM and read out via the pad readout. The pad readout is hexagonal in shape, and each side measures 10 mm. The readout signal is sampled by the APV25. The sampling frequency is 31.25 MHz (32 ns), and the number of samples is 15, resulting in a total width of 480 ns. These figures are identical to those for the GTR.

LG

LG is an electromagnetic calorimeter that uses lead glass and serves as a detector to distinguish electrons from hadrons based on differences in light emission. A single LG module comprises 38 lead glass blocks. Furthermore, the LG module is divided horizontally into six layers. Each layer consists of six blocks. (However, only the third and fourth layers contain seven blocks.) The size of the block varies between layers but is approximately 145 mm (H) × 120 mm (W) × 110 mm (D). Figure 1.23 shows the arrangement of each block. Photons generated by the lead glass blocks are detected by PMTs attached to each block. The signals from the PMTs are sampled by a circuit called DRS4. The sampling frequency is 960 MHz (1.04 ns), and the number of samples is 200. Therefore, the total width is 208 ns.

1.4 Purpose of this study

As mentioned above, no experimental results have yet been obtained that link hadron masses to spontaneous breaking of chiral symmetry. In summary, the chiral symmetry is partially recovered in a finite medium at a finite temperature, and in such a medium

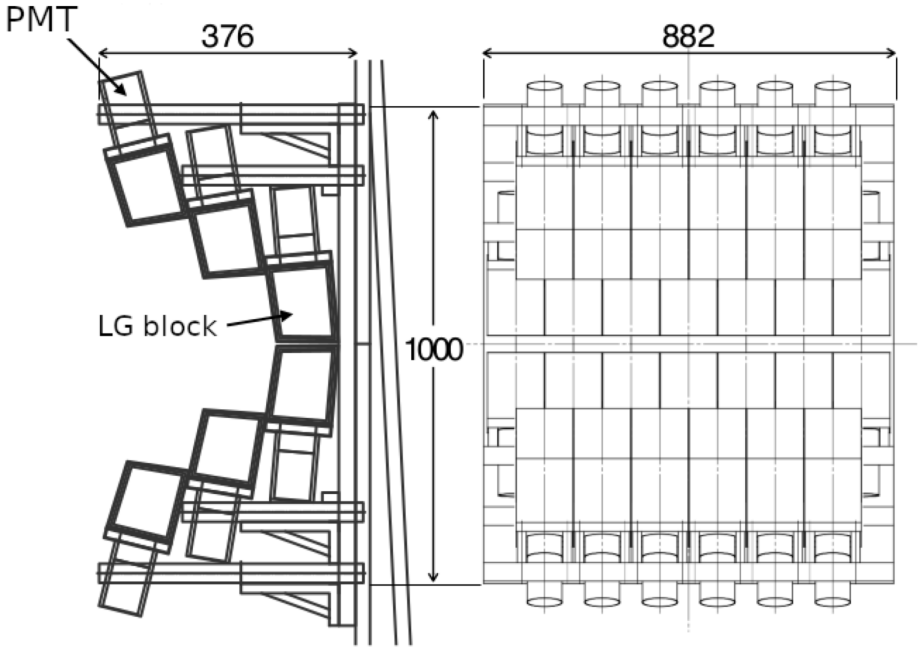

Figure 1.23: Side view and front view of the LG module.

the hadron mass spectrum is usually deformed from the spectrum in vacuum, but there are other possible reasons for the deformation. Therefore, it is necessary to rigorously estimate the interaction between the vector mesons and the medium and to check whether the deformation remains even after subtracting the contribution from the deformation of the spectrum. Therefore, we aim to experimentally observe the mass degeneracy of the chiral partners as stronger evidence that the hadron mass has changed as a result of the partial restoration of chiral symmetry. The mass degeneracy between chiral partners is difficult to explain in terms of monotonic effects, such as interactions with the medium. Furthermore, as the mass difference between the chiral partners is also an order parameter of the chiral symmetry, the observation of the mass degeneracy of the chiral partners is a very powerful evidence to link the two, as it allows us to observe the chiral symmetry restoration and the hadron mass change at once, rather than observing them piecemeal. This can be a very strong piece of evidence in linking the two. However, as we have seen in the NA60 example, it is very difficult to observe axial vector mesons, and to observe them in lepton pairs, they need to pass through chiral mixing, which disappears with chiral crossover at finite temperatures. There are other difficulties unique to finite temperatures, as will be discussed later, but there are still few examples of experiments at finite densities, and the problems do not arise at finite temperatures. The aim of this study is to investigate how much axial vector mesons can be observed and how much the

chiral partner tends towards mass degeneracy, using the J-PARC E16 experiment, a finite-density experiment that is currently underway, as an example, taking into account chiral mixing peculiar to finite densities.

Chapter 2

Density-Induced Chiral Mixing

Axial vector mesons cannot decay directly into lepton pairs. Therefore, mixing of axial vector mesons and vector mesons must be used to observe axial vector mesons. This mixing is called chiral mixing, and since chiral mixing at finite temperatures and chiral mixing at finite densities are caused by completely different mechanisms, the characteristics of each, including the finite temperature case, are presented in this chapter.

2.1 Low Energy Theorem

First, a theorem that holds only at low energies [45] is presented. This is because, while this theorem is the best-known theorem for discussing the degeneracy of the spectral functions of vector mesons and axial vector mesons, it is not known to hold only at low energies and has been erroneously applied even near the chiral phase transition temperature. This theorem is explained before describing chiral mixing. At temperatures sufficiently below the chiral phase transition temperature, Green's functions for vector mesons and axial vector mesons are given by

$$G_V^{\mu\nu}(T) = (1-\epsilon)G_V^{\mu\nu}(0) + \epsilon G_A^{\mu\nu}(0) \tag{2.1}$$

$$G_A^{\mu\nu}(T) = (1-\epsilon)G_A^{\mu\nu}(0) + \epsilon G_V^{\mu\nu}(0) \tag{2.2}$$

$$\epsilon = \frac{T^2}{6f_\pi^2} \tag{2.3}$$

As we have said many times, this theorem holds at low energies, but it is sometimes erroneously used at high energies as well. Suppose that we apply it to high energy. At $\epsilon = 1/2$, $G_V = G_A$, and if this is the signal for chiral symmetry restoration, then the temperature would be approximately $T = 160\,\mathrm{MeV}$. Although this value does not seem to be a bad value for the chiral phase transition temperature, when the spectral function is actually written, the masses of the vector mesons and axial vector mesons are not degenerate. Also, as will be shown in the next section, given the diagram of chiral mixing at finite temperatures, it should not vanish at the chiral phase transition temperature, but if this low-energy theorem is wrongly applied to high energies as well, the chiral mixing is maximized at about the chiral phase transition temperature The chiral mixing is maximized at about the chiral phase transition temperature.

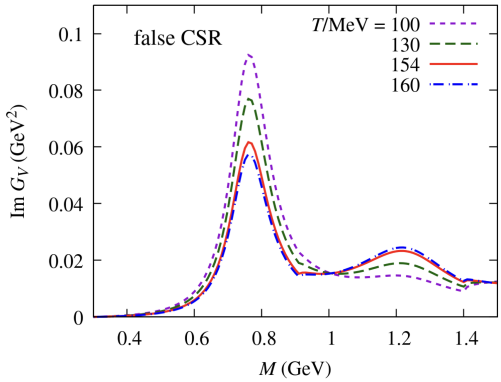

Figure 2.1: Spectral function of the vector meson considering the low-energy theorem. False chiral symmetry restoration that reaches $\epsilon = 1/2$ at $T = 160\,\mathrm{MeV}$ but is not mass degenerate.

2.2 Chiral Mixing in Hot Matter

Next, we describe the chiral mixing applicable in high-temperature regions such as those near the chiral phase transition temperature. At finite temperatures, chiral mixing is induced by the thermal pion field and occurs via the following diagram.

This means that chiral mixing at finite temperatures requires a pion field, so the temperature must reach about the mass of the pion. Furthermore, once the chiral symmetry is fully restored, the chiral partners are perfectly matched in mass, so a diagram through the pion is no longer valid. In other words, the chiral mixing at finite temperatures must disappear along with the chiral crossover [46].

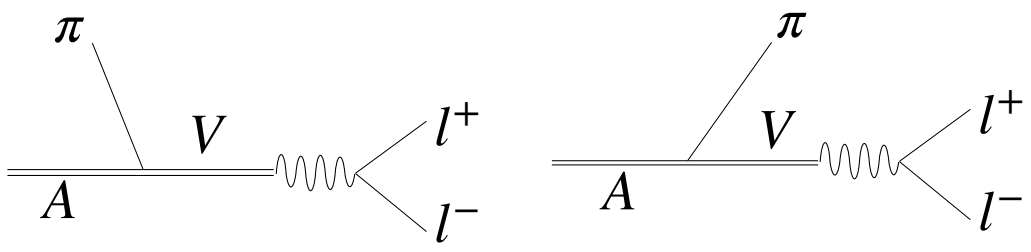

Figure 2.2: Diagram of chiral mixing at finite temperature, with vector mesons and axial vector mesons induced by the thermal pion field [46].

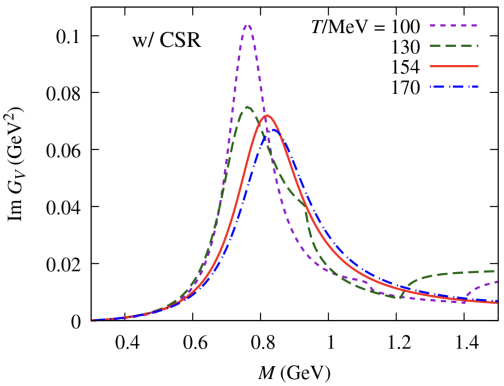

Figure 2.3: Spectral function of vector mesons considering chiral mixing at finite temperature. The signal of axial vector mesons appears at $m_A \pm m_\pi$, but the signal disappears near the chiral phase transition temperature ($T = 170\,\mathrm{MeV}$) [46].

At finite temperatures, additional factors make the observation of axial-vector mesons more difficult. At finite temperatures, lepton pairs derived from thermal photons are produced. Since thermal photons obey Bose-Einstein statistics, the vector-meson spectrum undergoes the following modifications.

$$\frac{dN}{d^4p}(p_0, \vec{p}; T, \mu_B) = \frac{\alpha^2}{\pi^3 s} \frac{\mathrm{Im} G_V(p_0, \vec{p}; T, \mu_B)}{e^{p_0/T} - 1} \tag{2.4}$$

Axial vector mesons create a signal on the heavier side than vector mesons and are not taller to begin with. When the Bose-Einstein distribution of thermal photons is multiplied by it, the axial vector mesons become relatively shorter than the vector mesons. This suppression of the signal from axial-vector mesons is called Boltzmann suppression.

2.3 Chiral Mixing in Dense Matter

Next, chiral mixing at finite density is described. First, consider the standard Lagrangian of the interaction between nucleons and ω mesons.

$$\mathcal{L}_\omega = g_\omega \bar{N} \gamma^\mu \omega_\mu N \tag{2.5}$$

The time component of this Lagrangian is as follows.

$$\mathcal{L}_{\omega 0} \propto \mu_B N^\dagger N \tag{2.6}$$

This form overtly breaks the charge conjugation, and the expected value of this time component is proportional to the density as follows.

$$\langle \omega_0 \rangle = g_{\omega NN} \cdot n_B / m_\omega^2 \tag{2.7}$$

This means that charge-conjugation symmetry is broken at finite densities. Therefore, consider the lowest order term that breaks the charge conjugation, but also has chiral and parity symmetries.

$$L = 2c\epsilon^{0\mu\nu\lambda} \mathrm{tr} \left[\partial_\mu V_\nu \cdot A_\lambda + \partial_\mu A_\nu \cdot V_\lambda \right] \tag{2.8}$$

Here V is the vector meson field and A is the axial vector meson field. In addition, c is not the speed of light, but the mixing strength. Unlike chiral mixing at finite temperatures, vector mesons and axial vector mesons mix directly at finite densities,

without any pion field or other intermediary [47, 48]. In fact, this term can be derived independently from the anomaly term of the WZW action [49, 50] and the Chern-Simons term in Holographic QCD [47]. However, the mixing strength values differ in each model as follows.

$$\text{WZW action} : c = 0.1\frac{\rho}{\rho_0}[\text{GeV}] \tag{2.9}$$

$$\text{Holographic QCD} : c = 1.0\frac{\rho}{\rho_0}[\text{GeV}] \tag{2.10}$$

However, the excessively strong mixing strength in holographic QCD leads to the condensation of vector mesons at densities only slightly higher than the nuclear density ρ_0 [47]. This is a consequence of the large N_c assumption when incorporating the AdS/CFT correspondence into QCD. In contrast, the standard chiral approach based on the gauged action of WZW yields a mixing strength approximately one order of magnitude weaker than that of holographic QCD, obtained as follows [50].

$$c = g_{\omega\rho a_1}\langle\omega_0\rangle = g_{\omega\rho a_1} \cdot g_{\omega NN}\frac{\rho_B}{m_\omega^2} \simeq 0.1\frac{\rho}{\rho_0}[\text{GeV}] \tag{2.11}$$

In the ϕ sector, the mixing strength is expected to be somewhat smaller due to the ϕ-N interaction being weaker than the ω-N interaction. However, as indeterminacy remains in the ϕ-N interaction [51, 28, 52, 53, 48], no method currently exists to precisely determine the mixing strength within the s-sector. Therefore, this study adheres to Weinberg's principle [54], namely that a general Lagrangian should be expressible as a linear combination of all possible operators permitted by symmetry. At finite density, the charge conjugation invariance is explicitly broken, leading to the derivation of a new class of operators, including the chiral mixing operator, which is the subject of this research. The low-energy constant remains unknown. Dimensional analysis suggests that the mixing strength is of the order of the Fermi momentum $p_F = 263$ MeV at the nuclear density ρ_0, but a precise value has not been obtained from any experiment. Therefore, this study treats the proportionality coefficient of the mixing strength in the s-sector as a free parameter and explores the response from high-density media.

However, in any case, the mixing strength is proportional to the density. Therefore, at a finite density, there is no suppression in the chiral phase transition as at a finite temperature, and the higher the density, the stronger the mixing.

Furthermore, this term changes the dispersion relation of the transverse waves of

vector mesons and axial vector mesons as follows.

$$s = p_0^2 - \vec{p}^2 = \frac{1}{2}\left[m_V^2 + m_A^2 \pm \sqrt{(m_A^2 - m_V^2)^2 + 16c^2\vec{p}^2}\right] \tag{2.12}$$

However, for the $\pm$ part, $+$ is the axial vector meson and $-$ is the vector meson. This dispersion relationship is illustrated in Figure 2.4.

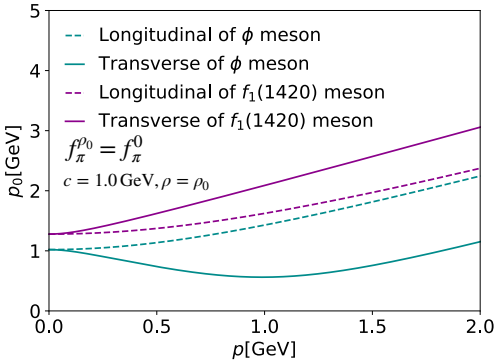

Figure 2.4: Dispersion relation for vector mesons due to the chiral mixing term [48]. Here the masses at rest are $m_V = 1.02$ GeV and $m_A = 1.42$ GeV and the mixing strength is 1.0 GeV.

Furthermore, a Taylor expansion of this dispersion relation in terms of ternary momentum yields

$$p_0^2 \sim m_{V,A}^2 + \left(1 \pm \frac{4c^2}{m_A^2 - m_V^2}\right)\vec{p}^2 \tag{2.13}$$

The fractional part in parentheses is the term due to the effect of mixing, including the mixing strength c, which increases as the mass difference between the vector meson and the axial vector meson becomes smaller and the ternary momentum increases. In other words, at finite density, the chiral mixing is enhanced by these two [55].

From the Lagrangian density of chiral mixing at finite density, the current-current correlation function is expressed as follows [50].

$$G_{V,A}^{\mu\nu}(p_0, \vec{p}) = P_L^{\mu\nu} G_{V,A}^L(p_0, \vec{p}) + P_T^{\mu\nu} G_{V,A}^T(p_0, \vec{p}) \tag{2.14}$$

Here, $P_{L,T}^{\mu\nu}$ denotes the polarization tensors, which are expressed as follows.

$$P_{T,\mu\nu} = g_{\mu i}\left(\delta_{ij} - \frac{\vec{p}_i \vec{p}j}{\vec{p}^2}\right) \tag{2.15}$$

$$P_{L,\mu\nu} = -\left(g_{\mu\nu} - \frac{p_\mu p_\nu}{p^2}\right) - P_{T,\mu\nu} \tag{2.16}$$

Formulating the chiral Lagrangian for pions, vector mesons, and axial-vector mesons in a nonlinear realization yields the longitudinal and transverse components of the current-current correlation function as follows.

$$G_V^L = \left(\frac{g_V}{m_V}\right)^2 \frac{-s}{D_V^L} \tag{2.17}$$

$$G_V^T = \left(\frac{g_V}{m_V}\right)^2 \frac{-sD_A^T + 4c^2\vec{p}^2}{D_V^T D_A^T - 4c^2\vec{p}^2} \tag{2.18}$$

$$G_A^L = \left(\frac{g_A}{m_A}\right)^2 \frac{-s}{D_A^L} \tag{2.19}$$

$$G_A^T = \left(\frac{g_A}{m_A}\right)^2 \frac{-sD_V^T + 4c^2\vec{p}^2}{D_V^T D_A^T - 4c^2\vec{p}^2} \tag{2.20}$$

Here, $D_{V,A}^{L,T}$ denotes the inverse of the propagator for the longitudinal and transverse waves of the vector meson and axial-vector meson, respectively: $D_{V,A}^{L,T} = s - m_{V,A}^2 - \Sigma_{V,A}^{L,T}$. The detailed calculation method for self-energy $\Sigma_V^{L,T}$ is presented in Section 3.1, but the effect on the ϕ meson is considered through the interaction between nucleons and kaons within the medium [56]. Furthermore, $s = p_0^2 - \vec{p}^2$, and $g_{V,A}$ is the coupling constant of the current corresponding to the vector/axial-vector meson. The spin-averaged current-current correlation function is expressed as follows.

$$G_{V,A} = \frac{1}{3}(G_{V,A}^L + 2G_{V,A}^T) \tag{2.21}$$

Thus far, the labels (V, A) correspond, respectively, to the iso-vector (ρ, a_1), iso-singlet (ω, $f_1(1285)$), and (ϕ, $f_1(1420)$) states. The coupling constant with the vector current can be related to ρ via chiral symmetry, resulting in $g_\rho = 0.119$ GeV.

$$g_\omega = \frac{1}{3}\frac{m_\omega^2}{m_\rho^2} g_\rho \tag{2.22}$$

$$g_\phi = \frac{\sqrt{2}}{3}\frac{m_\phi^2}{m_\rho^2} g_\rho \tag{2.23}$$

Calculating the imaginary part of the current-current correlation function thus obtained yields the spectral function. The dispersion relation of the longitudinal wave does not change, but the dispersion relation of the transverse wave has changed, and the spectral function has three peaks, as shown in Fig.2.5. Fig.2.5 is the spectral function of the vector meson (ϕ meson), but from left to right: the transverse wave component of the vector meson, the longitudinal wave component of the vector meson and the vector meson component of the transverse wave mixed with the transverse

wave component of the axial vector meson. Furthermore, although not considered in this study, it has been suggested that the dispersion relations of vector mesons within atomic nuclei may also change due to Lorentz invariance breaking [57, 41].

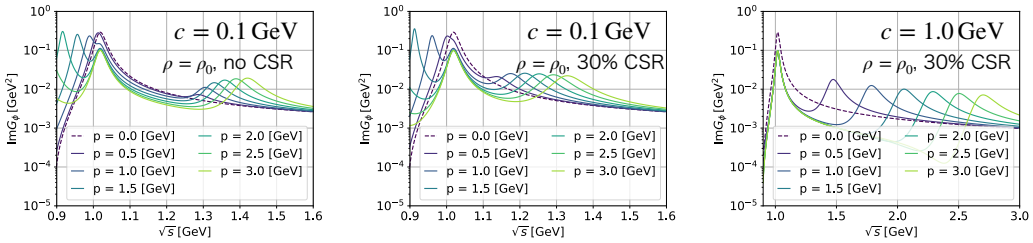

Figure 2.5: Spectral functions of vector mesons at nuclear density [48]. From left to right: mixing strength $c = 0.1$ GeV, no chiral symmetry restoration; $c = 0.1$ GeV, 30% chiral symmetry restoration; $c = 1.0$ GeV, 30% chiral symmetry restoration. Each spectral function has a three-peaked structure, which is due to changes in the dispersion relation of the transverse waves. In each spectral function, from left to right, there are three peaks: the transverse wave component of the vector meson, the longitudinal wave component of the vector meson and the vector meson component of the transverse wave mixed with the transverse wave component of the axial vector meson. This figure reflects effects such as broadening of the width due to *N-phi* interactions in the nucleus.

This study focuses on the ϕ meson and the $f_1(1420)$ meson as a pair of vector mesons and axial vector mesons. As explained in Section 1.1.4, these two are not exact chiral partners, but it is known that the contribution from disconnected diagrams that break the chiral partner symmetry is small, at least in vacuum and at finite density. Whether it is similarly small at finite density is not yet known, but we will assume this for now. This allows us to view this pair not merely as a parity doublet but as approximate chiral partners. Furthermore, the reason we consider the ρ meson and the a_1 meson, or the ω meson and the $f_1(1285)$ meson, is that these belong to the u,d sector. Consequently, they strongly interact with nucleons in the medium, creating resonant states. This requires considering the resonance states and their chiral partner resonance states, leading to a cumbersome spectral function [56]. This risks overlooking axial vector meson signals and introducing model dependence on resonances. Therefore, we focus on the s-sector ϕ meson and the $f_1(1420)$ meson.

Chapter 3

Calculation of Expected Di-electron Invariant Mass Spectrum at J-PARC E16 Experiment

In this chapter, the expected di-electron invariant mass distribution for the J-PARC E16 experiment is obtained, taking into account chiral mixing at finite density. As various effects are involved in the invariant mass distribution, the following sections explain how typical ones are treated.

3.1 Estimation of N-ϕ Interaction

In this section, we consider the interaction between nucleons and ϕ mesons in the target nucleus. As identified in Section 1.2.4, there is an attractive interaction between the nucleon and the ϕ meson, which causes a mass drop and a broadening of the spectral function of the ϕ meson. This effect is incorporated here in the mean-field approximation technique [58, 48]. First, the N-ϕ interaction has been investigated by many theoretical studies, but many theoretical models suggest that a large broadening occurs, while doing little about mass shift [59]. Therefore, for the sake of simplicity, we will not consider the mass shift resulting from the N-ϕ interaction but only the broadening. How do ϕ mesons consisting of $s\bar{S}$ interact with nucleons, but the main decay destination of ϕ mesons is $K\bar{K}$ and the kaon contains u, d quarks. Taking into account such a $K\bar{K}$ loop, it can be seen that the ϕ meson consisting of $s\bar{S}$ also interacts with the nucleon. In other words, the dressing of the kaon cloud is the origin of the modification of the ϕ mesons in nuclear matter. The

masses of kaon and anti-kaon in the mean field are expressed as follows [58].

$$m_K^* = \left[m_K^2 - a_K\rho_S + (b_K\rho_B)^2\right]^{1/2} + b_K\rho_B \tag{3.1}$$

$$m_{\bar{K}}^* = \left[m_{\bar{K}}^2 - a_{\bar{K}}\rho_S + (b_K\rho_B)^2\right]^{1/2} - b_K\rho_B \tag{3.2}$$

Here, ρ_s is the scalar density, and the three parameters are $a_K = a_{\bar{K}} = \Sigma_{KN}/f_\pi^2$ and $b_K = 3/(8f_\pi^2)$. However, the indeterminacy of the kaon-nucleon sigma term is large, so $a_K = 0.22$ GeV and $a_{\bar{K}} = 0.45$ GeV [60] are used instead. These values were obtained from data from kaon production in heavy-ion collision experiments. Using these parameters, $m_K^* = 510$ MeV and $m_{\bar{K}}^* = 380$ MeV at normal nuclear density. Then, with the change in the kaon mass, the width of the ϕ meson changes as follows.

$$\Gamma_\phi(s) = \frac{g_{\phi K\bar{K}}^2}{3\pi}\frac{k(s)^3}{s} \tag{3.3}$$

$$k(s) = \frac{1}{2\sqrt{s}}[(s - (m_K^* + m_{\bar{K}}^*)^2)(s - (m_K^* - m_{\bar{K}}^*)^2)]^{1/2} \tag{3.4}$$

The coupling constant $g_{\phi K\bar{K}}/4\pi = 1.69$ [61]. In systematic studies using the SU(3) coupled channel approach, etc., the ϕ meson shows a slight mass shift in nuclear density, but it is slight [59]. Therefore, for the sake of simplicity, this will be ignored in this article. The effective width of the ϕ meson obtained in this way is $\Gamma(s = m_\phi^2) \simeq 40$ MeV. In addition, at zero temperature, such as in nuclei, the effect of the meson loop vanishes. Therefore, the self-energy of the ϕ meson is replaced by the following.

$$\Sigma_\phi^{L,T}(s) = -im_\phi\Gamma_\phi^*(s) \tag{3.5}$$

3.2 Effect of Chiral Symmetry Partial Restoration

The pionic atom measurements strongly suggest a chiral symmetry restoration of about 40% in the u,d sector in nuclei [34]; in the strange sector the chiral symmetry restoration may be somewhat delayed, but it is expected to be reasonably well recovered. In this paper, we basically assume a chiral symmetry restoration of 30% in the STRANGE sector, except when we vary the degree of chiral symmetry restoration to check the results. Most chiral approaches show that there is no significant mass shift of the ϕ meson in cold nuclear matter. Therefore, in this thesis, we assume that the ϕ meson does not shift in mass due to chiral symmetry restoration, but the $f_1(1420)$ meson mass shifts, approaching medium independent m_ϕ, realizing the canonical condition ImG_A $rightarrow$ImG_V. The non-linear chiral Lagrangian based

on generalized hidden local symmetry (GHLS) can well explain the phenomelogy of pion and vector mesons [62, 63, 50]. Based on it, the masses of vector and axial vector states are expressed in leading order as follows [48].

$$m_A^2 - m_V^2 = g^2 \frac{m_A^2}{m_V^2} f_\pi^2 \tag{3.6}$$

where g is the gauge coupling constant $g = 6.61$ [50]. As mentioned above, m_ϕ is assumed to be fixed, so the mass of $f_1(1420)$ carries information about the medium-dependent chiral symmetry of the garment. The above equation is a relational expression that clearly connects m_{f_1} and the order parameter f_ϕ. Therefore, when m_{f_1} is fixed, m_{f_1} can also be treated as an order parameter. The relationship between this mass and f_π is shown in Figure 3.1. The horizontal axis represents $1 - (f_\pi/f_\pi^0)^2$. As chiral symmetry recovers, the order parameter f_π decreases; thus, a higher value on this horizontal axis indicates a greater restoration of chiral symmetry. According to the assumed scenario, the mass of the ϕ meson remains unchanged by the restoration of chiral symmetry, whilst the mass of the $f_1(1420)$ meson approaches that of the ϕ meson according to equation 3.6.

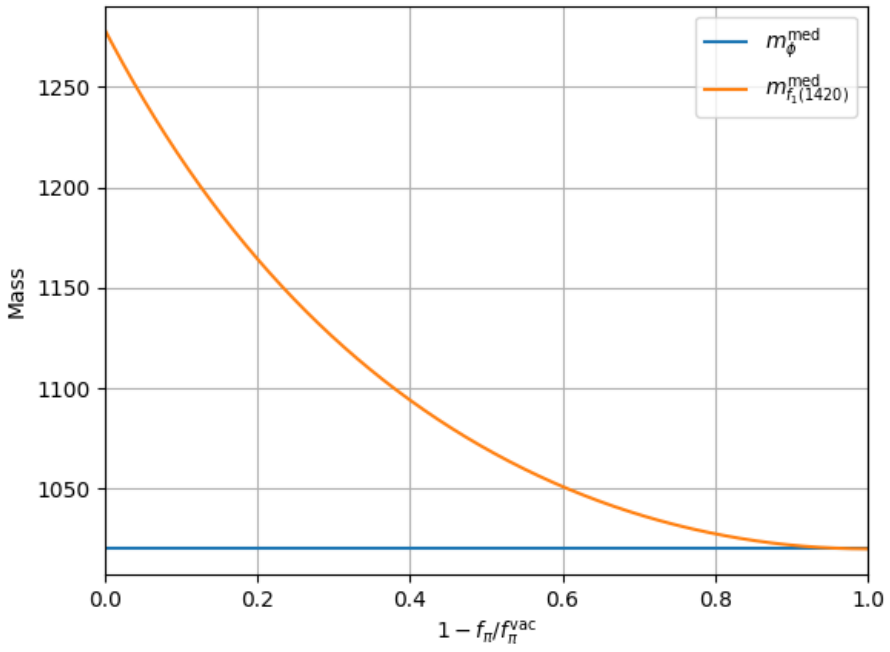

Figure 3.1: Mass density dependence of the ϕ meson and the $f_1(1420)$ meson. In this calculation, no change in the mass of the ϕ meson due to the restoration of chiral symmetry is assumed. Furthermore, the $f_1(1420)$ meson approaches the mass of the ϕ meson with the restoration of chiral symmetry, as described by equation 3.6.

Next, for width, the constant-width approximation of the $f_1(1420)$ meson above the threshold is expressed as follows.

$$\Gamma^{\rm vac}_{f_1(1420)}(s) = \Theta[s - (m_\pi + 2m_K)^2]\Gamma^{\rm vac}_{f_1(1420)} \tag{3.7}$$

$$\Gamma^{\rm vac}_{f_1(1420)} = 54.9\,{\rm MeV} \tag{3.8}$$

Using these widths in vacuum, we employ a simple model in which the width of the $f_1(1420)$ meson in the medium is expressed as follows due to the partial restoration of chiral symmetry [48].

$$\Gamma^*_{f_1(1420)}(s) = \Gamma^{\rm vac}_{f_1(1420)} \left(\frac{f^*_\pi}{f^{\rm vac}_\pi}\right)^2 + \Gamma^*_\phi(s)\left[1 - \left(\frac{f^*_\pi}{f^{\rm vac}_\pi}\right)^2\right] \tag{3.9}$$

Consequently, when the chiral symmetry is fully restored, the width also degenerates, achieving $\Gamma^*_\phi = \Gamma^*_{f_1}$. Figure 3.2 illustrates how the widths of the ϕ meson and the $f_1(1420)$ meson change as density increases. Following the simple model of the width of the $f_1(1420)$ meson considered here, the width of the $f_1(1420)$ meson approaches that of the ϕ meson as density increases, due to the restoration of chiral symmetry. In contrast, the width of the ϕ meson in this study does not change due to the restoration of chiral symmetry; its width varies with density solely due to the broadening effect caused by its interaction with nucleons. A method for quantifying mass and width near chiral symmetry restoration while fully incorporating nuclear many-body effects remains theoretically unknown. Meanwhile, calculations from lattice QCD at finite temperature and zero density provide intriguing clues: the thermodynamics of physical pions and kaons in $N_f = 2 + 1$ QCD is indeed governed by $O(4)$ universality [64]. The parameterisations of the mass and width, such as equations 3.6 and 3.9, used in this work are not unique, but are well supported by these lattice QCD results.

3.3 Kinematical Distribution of ϕ meson at J-PARC E16

To calculate the invariant mass distribution of the electron pairs obtained experimentally, it is necessary to integrate the spectral function. In doing so, the integration must be weighted by the kinematical distribution of the ϕ meson. Since the spectral function is a function of momentum and density, the required distributions are the momentum distribution of the ϕ meson and the density distribution experienced by

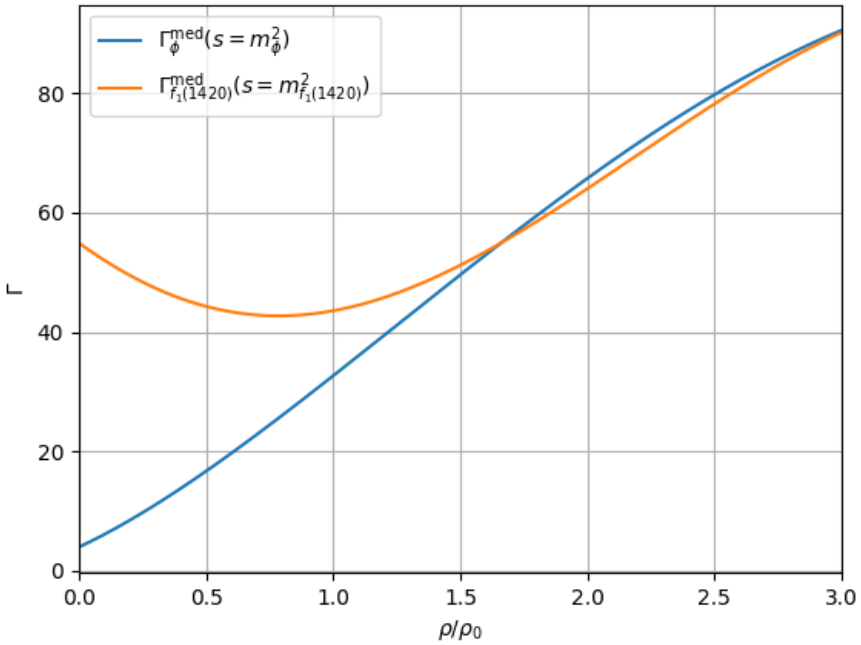

Figure 3.2: The width density dependence of the ϕ meson and the $f_1(1420)$ meson. In this calculation, the ϕ meson's width is assumed to change solely through its interaction with nucleons in the medium, without any change due to the restoration of chiral symmetry. Furthermore, the $f_1(1420)$ meson approaches the width of the ϕ meson with the restoration of chiral symmetry, as described by the simple model given by equation 3.9.

the ϕ meson at the time of decay. Therefore, the distribution is determined using a method called the PHSD transport approach [65, 66], which solves the off-shell equation of motion to describe how the ϕ meson moves through the nucleus following the reaction between the proton beam and the target nucleus. This allows consideration of the momentum distribution formed as the ϕ meson repeatedly scatters with nucleons within the nucleus, and of ϕ mesons experiencing various densities during this process – such as those decaying inside the nucleus, near the surface, or outside the nucleus. Figure 3.3 shows the momentum and density distributions of the ϕ meson obtained in the p+A 30 GeV fixed-target experiment using the PHSD transport approach. This figure represents the case for the Pb nucleus. As might

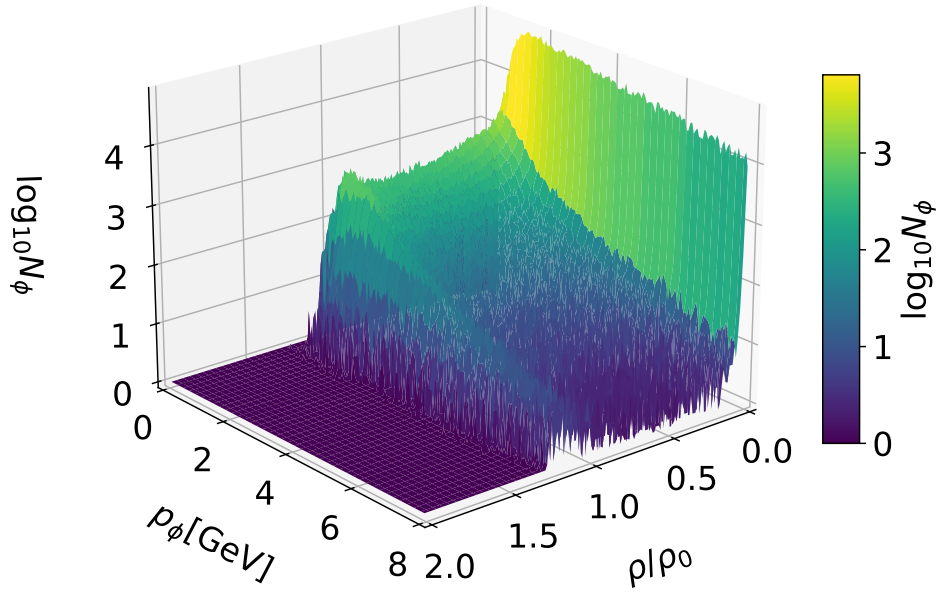

Figure 3.3: The momentum distribution of the ϕ meson obtained in the p+A 30 GeV fixed-target experiment calculated using the PHSD transport approach, and the distribution of the density felt by the ϕ meson when it decays [48].

be expected from its relatively long lifetime (46.4 fm in vacuum), it is evident that most ϕ mesons decay outside the target nucleus. Consequently, the distribution at $\rho = 0$ is markedly more abundant than elsewhere. In regions of higher density, the distribution is broadly flat, though exhibiting a small peak structure at $\rho = \rho_0$. Furthermore, at densities significantly higher than $\rho = \rho_0$, the distribution drops sharply towards zero. This distribution suggests that several ϕ mesons perceive a density greater than the nuclear density ρ_0. This is thought to originate from the initial stage of the p+A collision, where the incident proton locally creates a density

slightly higher than the nuclear density.

However, in the PHSD transport approach, calculations are performed for off-shell ϕ mesons, and their width must be unified to a single value. Therefore, the distribution of widths for ϕ mesons within the nucleus was calculated, taking into account chiral mixing, and the most frequent width was adopted. This distribution is shown in Figure 3.4. Consequently, since the nuclear density produces $\Gamma_\phi \sim 30$ MeV the most

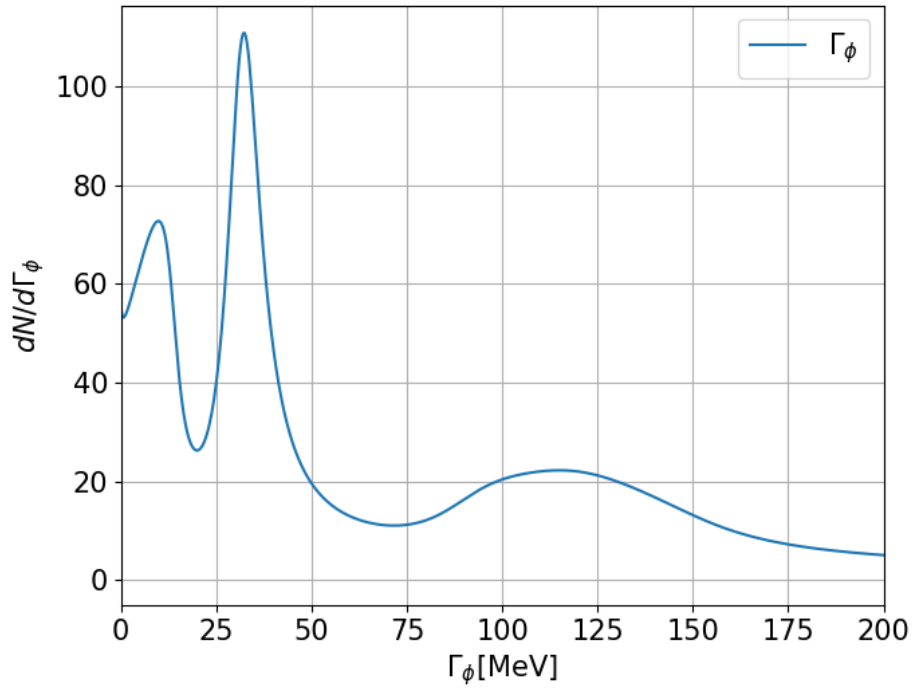

Figure 3.4: The distribution of the width of the ϕ meson within the atomic nucleus. Due to the consideration of chiral mixing at finite density, three peaks are observed: the central peak corresponds to the longitudinal component without chiral mixing, while the peaks on either side represent the transverse components with chiral mixing.

frequently, this value was adopted. Previous studies employing other calculation methods also yielded values around 20 to 40 MeV, making this value reasonable. However, examining the distribution reveals the existence of a ϕ meson with zero width. Should such a ϕ meson truly exist, it would result in a δ-function-like spectrum. The formula 3.3 used to calculate the width this time directly extends the vacuum formula to finite density. However, in reality, kaons also acquire a decay width, and the effect of this is neglected, leading to an unphysical situation near the threshold at $\sqrt{s} = m_K + m_{\bar{K}}$ (Figure 3.5). However, this is not problematic in regions where the kaon decay width is not significantly important, away from the vicinity of $\sqrt{s} = m_K + m_{\bar{K}}$. Therefore, the threshold region is ignored.

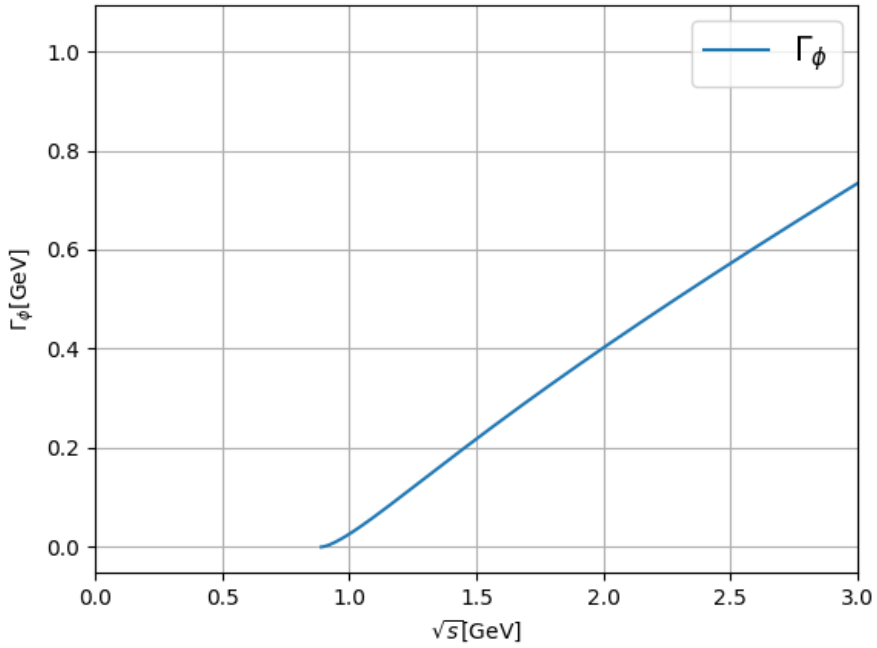

Figure 3.5: The $\sqrt{s}$ dependence of Γ_ϕ calculated based on equation 3.3. Since finite density effects on the kaon width are not considered, Γ_ϕ becomes zero at a certain $\sqrt{s}$, leading to a non-physical picture in this vicinity. Furthermore, the increase in Γ_ϕ as $\sqrt{s}$ grows stems from the expansion of the number of energy states available for decay within phase space.

3.4 Estimation of Background

The J-PARC E16 experiment is a fixed-target experiment at p+A 30 GeV. The anticipated background around the ϕ meson primarily consists of charged pions misinterpreted as electrons; electrons from Dalitz decay of π^0 mesons; electrons from interactions with the detector (gamma conversion); and a combinatorial background. To estimate the distribution of this background, Monte Carlo simulations were performed using JAM [67] and Geant4. First, all pairs of $(\pi^+, \pi^-), (e^+, e^-), (pi^+, e^-), (e^+, \pi^-)$ produced by the aforementioned background sources were reconstructed using their invariant mass. The distribution is shown in Figure 3.6. These distributions are then

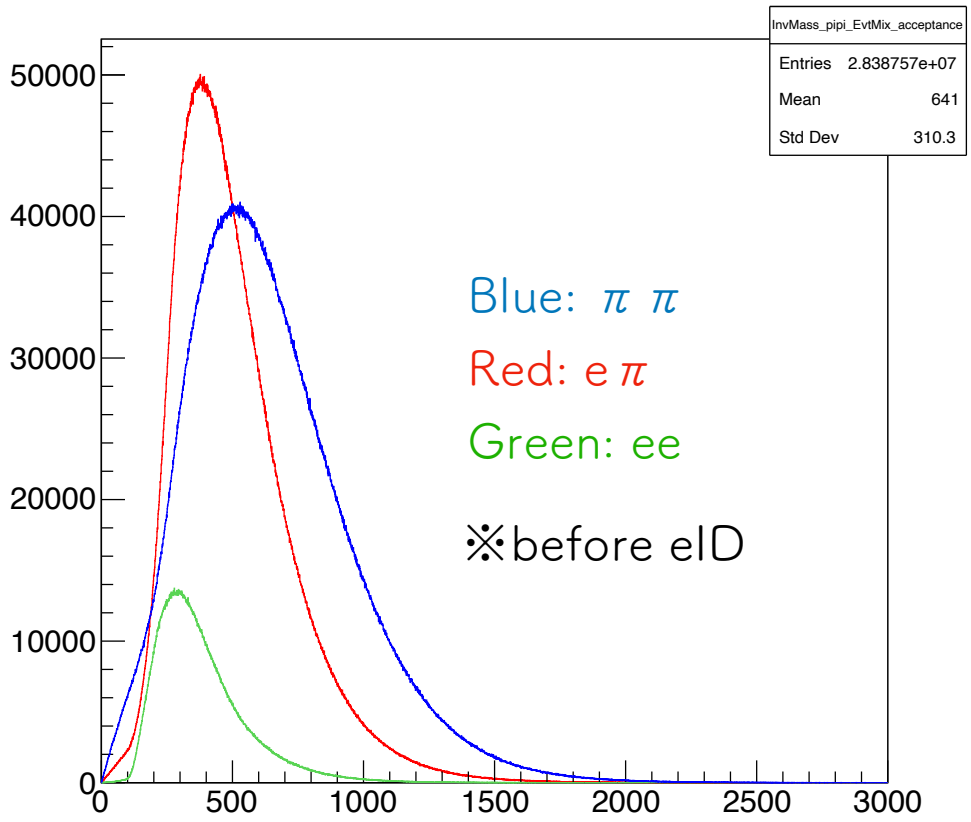

Figure 3.6: Background estimation via Monte Carlo simulation using JAM and Geant4 for J-PARC E16 Run2. This considers Dalitz decay of charged pions and π^0 mesons, electrons from gamma conversion, and their combinatorial background. This distribution is created through event mixing to increase the number of statistical quantities.Furthermore, the collision system in this diagram is p+Cu, and the number of Cu targets is one.

balanced through mechanisms such as the efficiency of electronic identification by

LG and HBD, and further scaled to the yield of E16 Run2.

The method of scaling is as follows.

$$N_{ee,e\pi,\pi\pi} = \frac{1}{N_p^{\rm sim}} \int \frac{dN_{ee,e\pi,\pi\pi}}{dm} dm \times \epsilon_{\rm pair\,pid} \times \epsilon_{\rm others} \times N_{\rm target} \times N_p^{\rm Run2} \tag{3.10}$$

Equation 3.10 represents the number of background pairs formed by various combinations assumed in Run2. The integral value in Figure 3.6 is scaled to correspond to this value. In equation 3.10, $dN_{ee,e\pi,\pi\pi}/dm$ represents the invariant mass distribution of the background composed of various pairs. However, it should be noted that this distribution is not the background shown in Figure 3.6, which was created by event mixing, but rather the invariant mass distribution prior to event mixing. Furthermore, as stated in the caption of Figure 3.6, the simulation used to obtain this figure assumes the collision reaction between a single Cu target and protons. $\epsilon_{\rm pair\,pid}$ is the square of the electron identification efficiency for LG and HBD for electron pairs, the square of $1 - \epsilon_{\pi\,\rm rejection}$ for pion pairs, and the product of the electron identification efficiency and $1 - \epsilon_{\pi\,\rm rejection}$ for electron-pion pairs. Note that $\epsilon_{\pi\,\rm rejection}$ is the pion rejection efficiency of LG and HBD. $\epsilon_{\rm others}$ is the product of the GTR trigger efficiency, the trigger logic efficiency, the pair reconstruction efficiency, and the efficiency remaining after other analyses; these efficiencies are described in the next section 5.2. $N_{\rm target}$ denotes the number of targets, $N_p^{\rm sim}$ is the number of protons simulated to strike the target, and $N_p^{\rm Run2}$ is the effective proton number for Run2. The specific calculation method is described in Section 6.1, but it can be considered the number of p+A collisions that are actually recorded as data in Run2.

3.5 Effect of E16 Spectrometer's Mass Resolution

The electron pair invariant mass distribution observed experimentally is not merely the integral of the spectral function, but rather a distribution further smeared by the spectrometer's mass resolution. Therefore, to reproduce the distribution obtained experimentally, it is necessary to incorporate the effect of mass resolution. To achieve this, a convolution integral is performed using a Gaussian that simulates the mass resolution. Specifically, the invariant mass distribution is obtained using the following expression:

$$\frac{dN}{dm} = \int \left[\frac{dN_\phi}{ds} + \frac{dN_{\rm Bkg}}{ds} \right] g(m-s) ds \tag{3.11}$$

Here, $g(m-s)$ is a Gaussian with mass resolution width, $dN_{\rm Bkg}/ds$ is each component of the background distribution obtained in Section 3.4, scaled by yield after passing

through electron identification, and dN_ϕ/ds is expressed as follows.

$$\frac{dN_\phi}{ds} = \int \frac{\alpha^2}{\pi^3 s} \mathrm{Im} G_V(\vec{p}, s, \rho) \frac{dN_\phi}{d\vec{p} d\rho dt} \frac{d\vec{p}}{2p_0} d\rho dt \tag{3.12}$$

Here, $dN_\phi/d\vec{p}d\rho dt$ represents the kinematical distribution of the ϕ meson obtained by the PHSD transport approach. However, in practice, as shown in Figure 3.3, it has already been integrated with respect to time.

Chapter 4

J-PARC E16 Run0e

This chapter describes how preparations were made and how the experiment was conducted for Run0-e of the J-PARC E16 experiment, which was the experiment carried out in this research.

4.1 Construction of GTR

This section describes the assembly of the GTR, the main tracker for E16. The procedure involves applying high voltage to the GEM used in the GTR during a process called conditioning, which tests the GEM and burns off debris near the GEM holes. This is followed by the assembly of the GTR chamber and testing it after mounting the chamber onto the CFRP frame. Subsequently, the actual operations during Run0-e and the detector's state after Run0-e are described.

4.1.1 Conditioning of GEM

The GEMs used in the GTR were developed by CERN and manufactured by Raytech Corporation. They are produced using a wet etching process and feature a biconical cross-section, as shown in Figure 4.1. The holes are spaced 140 μm apart and arranged in a triangular lattice pattern. GEM foils are available in sizes of 100 mm $\times$ 100 mm, 200 mm $\times$ 200 mm and 300 mm $\times$ 300 mm to correspond to 100GTR, 200GTR, and 300GTR respectively, and are referred to as 100GEM, 200GEM, and 300GEM. As explained in subsection 1.3.1, to mitigate damage from discharge and conduction while maintaining detector capacity, the copper layer on one side of the GEM is divided into island-shaped sections. The 100GEM has no divisions, the

200GEM has four divisions, and the 300GEM has twelve divisions. Furthermore, among the 300GTR, the 300GEM used as the final layer (GEM3) is also used for trigger signal generation; therefore, both sides are divided into 24 sections. Each of these divided islands is called a GEM strip, or simply a strip. If debris or burrs exist around the holes in these GEMs, discharges can occur from them. In the worst case, debris or burrs, carbonized by the discharge, can cause electrical continuity between the front and back of the GEM, preventing voltage from being applied to it. As such occurrences after assembling the GTR chamber would be troublesome, the process of applying voltage to individual GEMs prior to chamber assembly to burn away any debris or burrs via discharge, thereby preparing clean GEMs, is termed conditioning. Furthermore, if a significant portion of the GEM strip becomes conductive and unusable during this process, that section becomes a dead region, effectively reducing the acceptance area. Consequently, such a strip is not used in the chamber assembly in the first place. Conditioning is performed as shown in

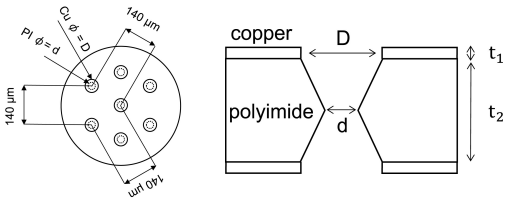

	100-GEM &200-GEM	300-GEM 12 segments	300-GEM 24 segments
D [μm]	65 ± 5		55 ± 5
d [μm]	35 ± 5		25^{+10}_{-5}
t_1 [μm]		4	
t_2 [μm]		50	

Figure 4.1: (Left) Arrangement and dimensions of holes drilled into the GEM surface. (Center) Cross-sectional view of GEM holes. (Right) Various dimensions.

Figure 4.2, whereby the GEM is placed within an acrylic box filled with nitrogen. A microammeter is connected to the GEM to gradually establish a potential difference across its front and rear surfaces, ultimately creating a 600 V potential difference. As the beam time operates at approximately 380 V, this potential difference is sufficiently higher. Conditioning was carried out for each GEM over a period of several days. An example of the results of conditioning is shown below. Following conditioning, the voltage was increased in 50V increments every 60 seconds for leak current measurement, with the leak current measured after applying 500V for one hour. Generally, GEMs with a leakage current of 1 nA or less and discharge counts of approximately 1 or 2 were deemed acceptable and used for chamber assembly. However, due to limited GEMs quantities in Run0-e, some GEMs that did not fully meet the criteria were also used.

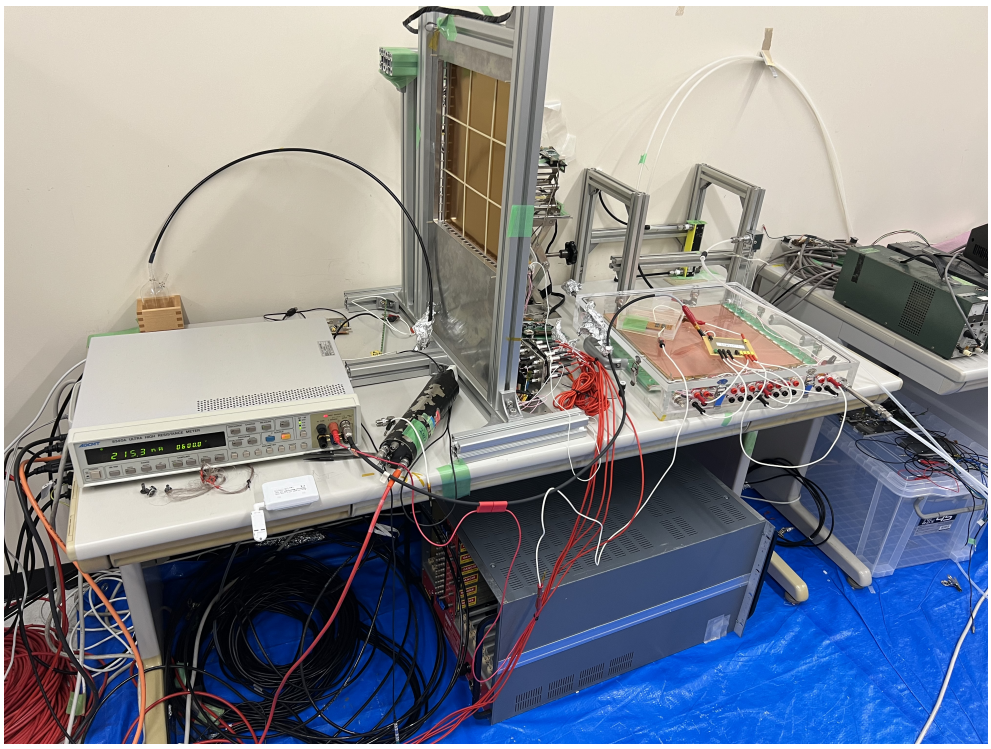

Figure 4.2: GEM conditioning setup. The acrylic box on the left side of the desk houses the GEM, its interior filled with nitrogen gas. Placed atop the acrylic box is the GEM's protective resistor, while the microammeter is positioned on the right side of the desk.

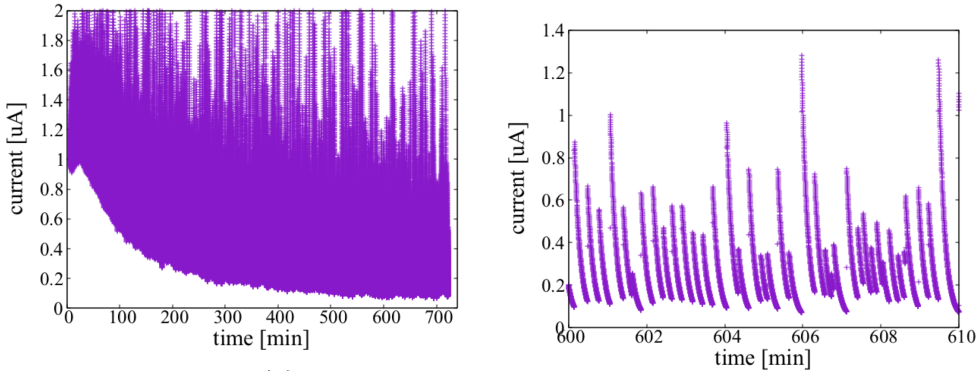

Figure 4.3: An example of GEM conditioning results. (Left) The horizontal axis represents time, the vertical axis represents the current flowing through the GEM. As conditioning progresses over time, the current flowing between the front and back of the GEM can be seen approaching zero. (Right) An enlarged view of the left diagram. Each time a discharge occurs, the current rises discontinuously, followed by an exponential decrease, and this pattern repeats.

4.1.2 Construction of GTR chamber

The GTR chamber, as shown in Figure 1.17, consists of layers stacked in the order MESH, GEM1, GEM2, GEM3 and the readout foil. Rubber sheets are inserted between each layer to trap gas. It was constructed specifically following the procedure shown in Figure 4.4. In the final step of Figure 4.4, an aluminum seal is applied to the Mylar. This is a countermeasure against the drift electric field between MESH-GEM1 being weaker than expected. It is unclear whether this was because the MESH, being a mesh rather than a perfect plane, produced a weaker electric field than a plane would, or whether the Mylar itself became charged and weakened the drift electric field; it is likely one of these two reasons. Proposals such as using aluminized Mylar instead of MESH were considered. However, to avoid issues such as time and cost implications, and to prevent the aluminized Mylar from expanding due to the gas pressure within the chamber, which could introduce positional dependence in the drift electric field, it was decided to retain the MESH. As a simple countermeasure, an aluminum seal was applied over the Mylar. By applying a voltage to the aluminum seal to bring it to the same potential as the MESH, the aforementioned problem was resolved. To minimize material increase as much as possible, the aluminum seal was selected from commercially available options to be as thin as possible. Furthermore, to dissipate the charge accumulated on the Mylar through the aluminum seal, we chose an adhesive with conductive properties.

4.1.3 Test of GTR before Run0e

This subsection describes the GTR testing prior to Run0-e. As shown in Figure 4.5, the assembled GTR chamber was installed within a CFRP frame. The GTR readout board was then connected via coaxial cable to the APV25 chip, a circuit for data readout.

Furthermore, the APV was connected to the PC via SRS, enabling data acquisition. However, in tests prior to Run0-e, as each GTR chamber was tested using a beta source, a separate trigger signal had to be generated and inputted to the APV. Consequently, during the tests, the chamber was positioned between the source and the scintillator, with the scintillator signal used as a trigger signal. In summary, the setup is as shown in Figure 4.6. An example of the results obtained from this test is shown in Figure 4.7. The signals read from the GTR chamber exposed to the beta source were verified and the dead region was first confirmed. Dead regions caused by APVs failure were addressed by replacing APVs. For dead regions due

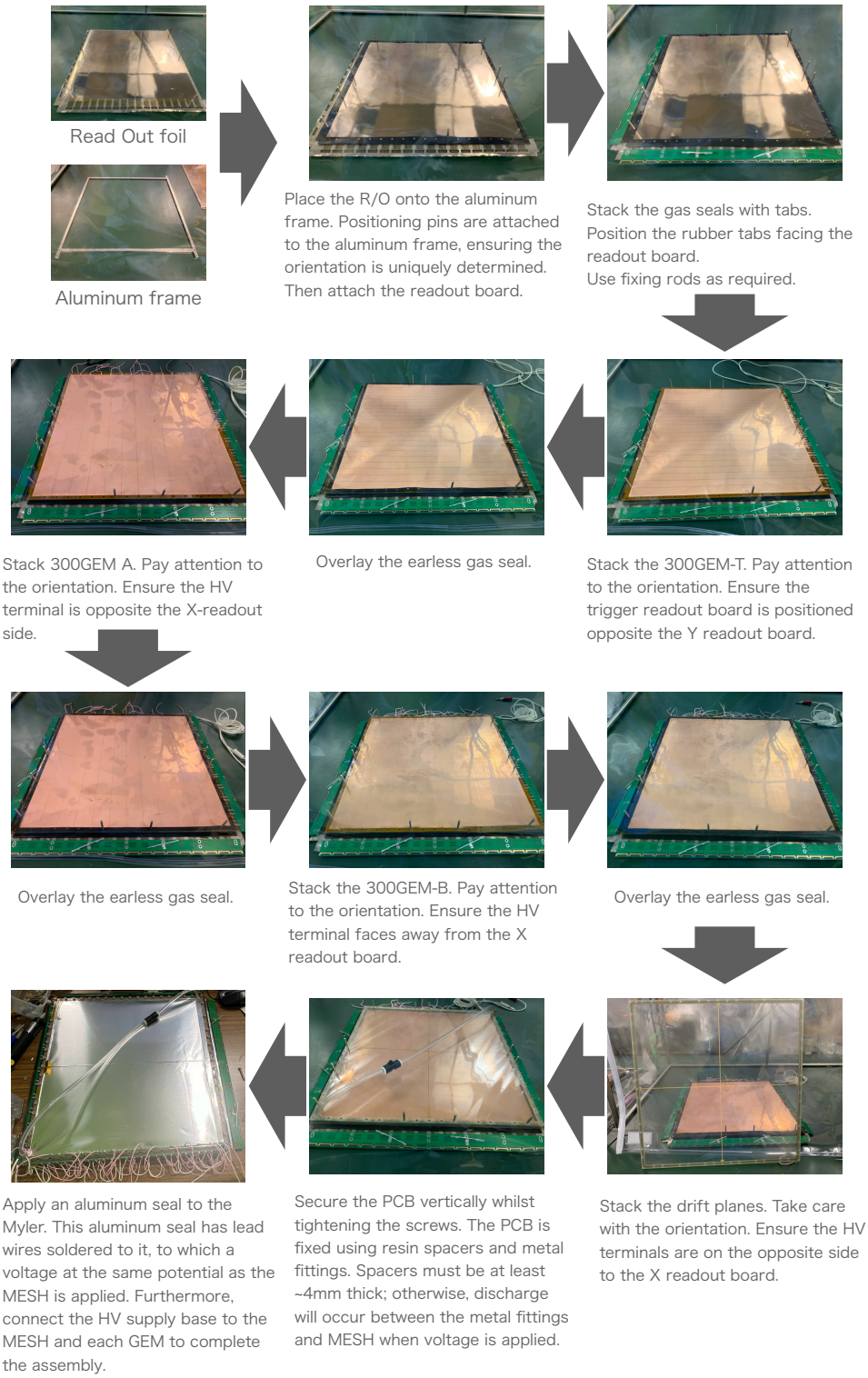

Figure 4.4: GTR chamber production procedure. Diagram shows GTR300 production example.

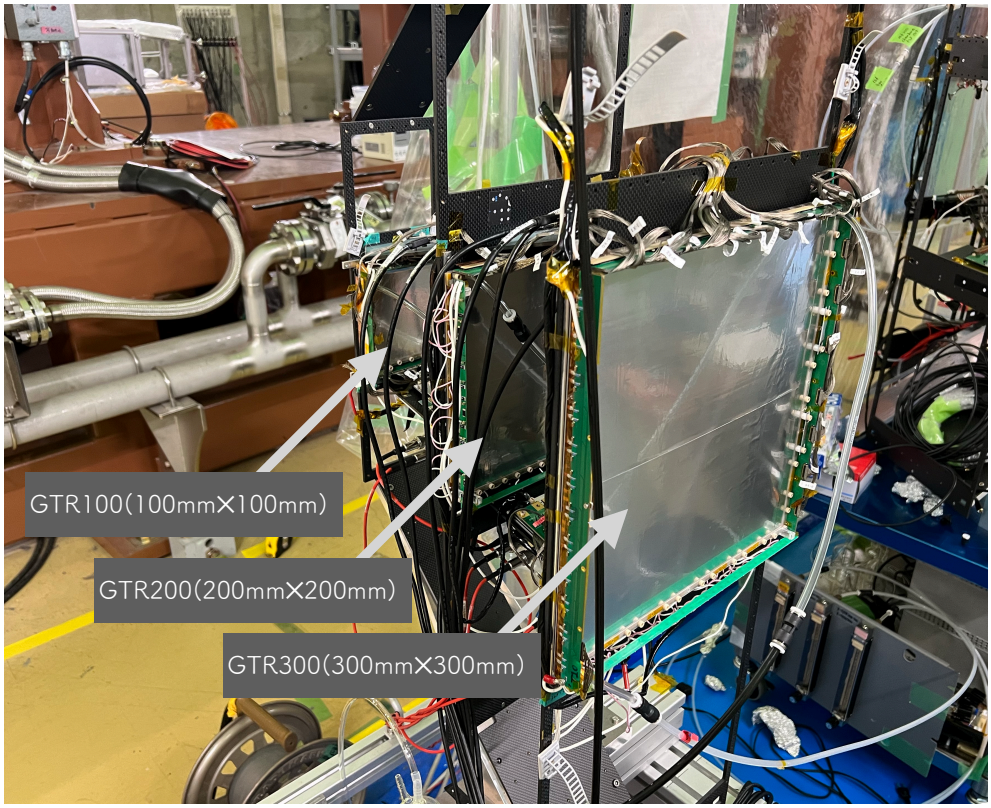

Figure 4.5: Photograph of the GTR chamber mounted on a CFRP frame.

to GEMs continuity issues, as the number of GEMs available in time for Run0-e was limited, assembly proceeded allowing continuity up to 2 strips. Furthermore, the wave height distribution of the readout signals (Figure 4.8) was examined. As the wave height readable by the APV saturates at a certain level, the wave height distribution exhibits a peak at the right end. Upon confirmation of the height of this peak, the gain of the GTR chamber was verified, and the voltage applied to the GEMs was adjusted until a sufficient gain was achieved. Furthermore, we confirmed the distribution of the time difference between the arrival times of the first and last ionized electrons generated by the electrons of the beta source within the drift gap reaching the readout foil (Figure 4.9). Since this time difference has a somewhat typical value, the distribution exhibits a peak structure. If this peak has a tail extending towards larger time differences, it indicates a slow drift velocity for the ionized electrons. In contrast, a narrow peak implies a fast drift velocity. We used this distribution to verify whether the drift velocity was sufficiently fast.

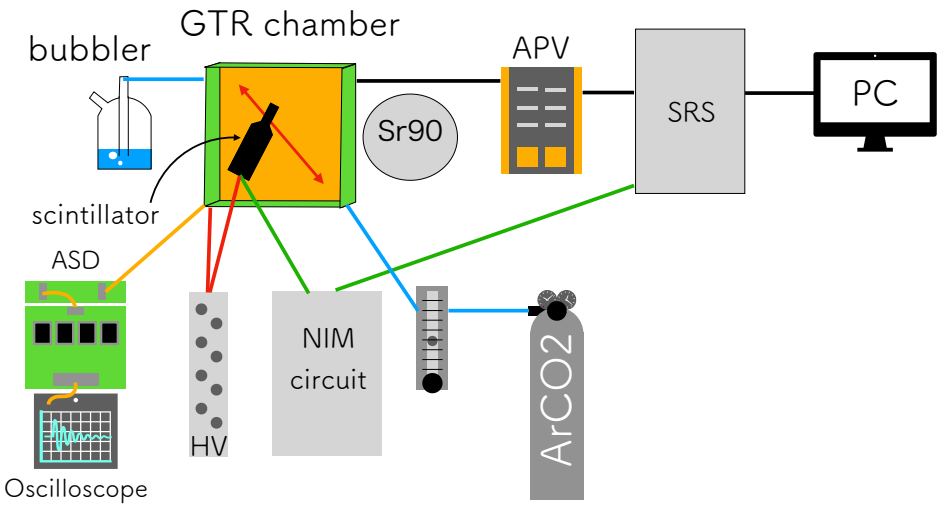

Figure 4.6: Illustration of the test setup for the GTR prior to Run0-e. The GTR chamber is positioned between the beta source (Sr90) and the scintillator, and is moved along the chamber's diagonal. Moving along the diagonal allows testing of both the x-strip and y-strip of the GTR chamber. The scintillator generates a trigger signal, which is then shaped by the NIM circuit and input to the APV via the SRS. Signals from the GTR chamber are sent to the PC via the APV and SRS. Regarding the GTR300, an ASD is also connected; an oscilloscope is used to verify that the trigger signal is correctly output from the ASD. High voltage is supplied to the GTR chamber and scintillator from the high voltage power supply module. ArCO2 is introduced into the GTR chamber, which is subsequently vented to atmosphere. A bubbler is fitted as a device to prevent atmospheric air from flowing back into the chamber.

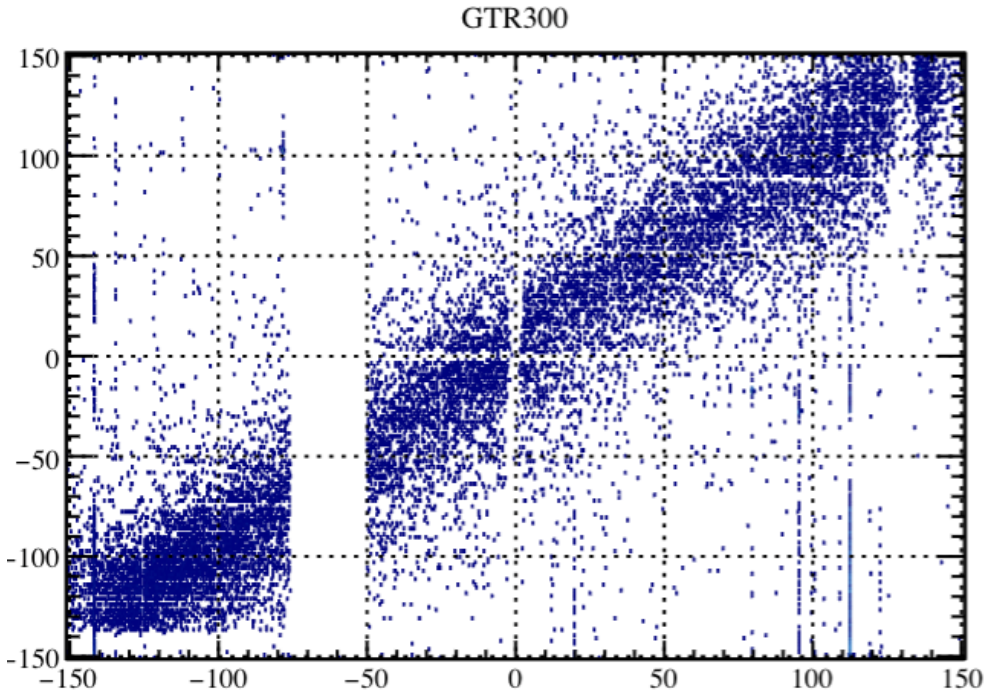

Figure 4.7: Signal read from the chamber when a beta source was directed at it and moved along the chamber's diagonal. There is an interrupted section on the left; this becomes a dead region due to reasons such as the GEM at this point becoming shorted between front and back, preventing electron amplification, or the APV corresponding to the strip at this point being faulty.

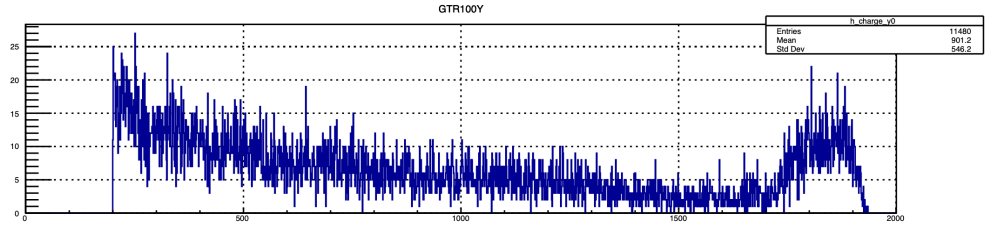

Figure 4.8: The wave height distribution of the signal read out from the chamber when the beta source was directed at the chamber and moved along its diagonal.

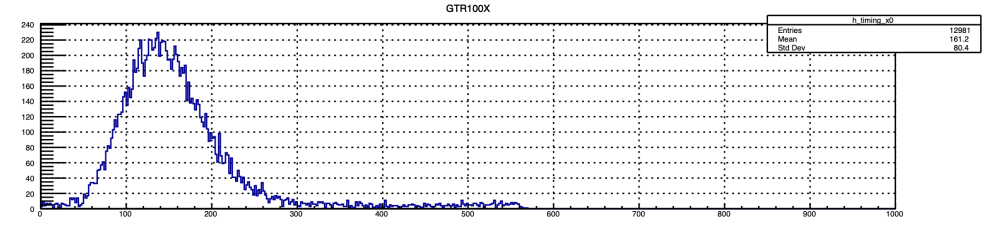

Figure 4.9: The distribution of arrival time widths for ionised electrons generated within the drift gap when a beta source is applied to the chamber.

4.2 Conditions of Detectors at Run0-e

This section provides an overview of Run0-e, its execution, and the detector dead region detected as a result.

4.2.1 Operation

Run0-e was conducted from 19 April to 3 June 2024. However, it was interrupted during two periods: from 3 May to 20 May and from 25 May to 30 May, due to malfunctions in the MR and other accelerators. The following figure 4.10 summarizes the activities carried out during Run0-e. Within this, the present study uses data from the Vector Meson Run, which triggers electron pairs originating from vector mesons, amounting to approximately 26.8 hours. The Vector Meson Run trigger requires that at least two electron-positron-like tracks be detected, with coincidences occurring at a minimum of two locations for each of the GTR, HBD, and LG triggers. Furthermore, to exclude electron pairs originating from the Dalitz decay of the pion, it also requires that the opening angle between these two tracks be greater than 45 degrees. Online, the opening angle is calculated using the hit positions in the LG. Furthermore, the proton beam reaching the B line has a temporal structure, characterized by an initial phase of instantaneously high beam intensity. High multiplicity events occur during this initial beam phase and at the time of target collision. Therefore, to avoid pile-up from multiple collision events, a GTR multiplicity veto was also applied. This involves setting a period during which the trigger is not issued when the GTR trigger signal is ringing at a high frequency.

4.2.2 Conditions and survived detectors

During Run0-e beam time, the multiplicity of charged particles is incomparable to that observed during source tests. The detailed cause remains unclear, but during Run0-e, the rear modules (101, 102, 108, 109) in particular experienced severe discharge. This resulted in over half the acceptance becoming dead regions, and the GEMs exhibited such poor conductivity that gain could not be achieved even with a high voltage applied. Consequently, only the three forward modules remained usable for analysis. Naively, one would expect a higher multiplicity towards the forward region, yet the rear modules suffered more damage. Although effects such as beam halo may be considered, this remains speculative.

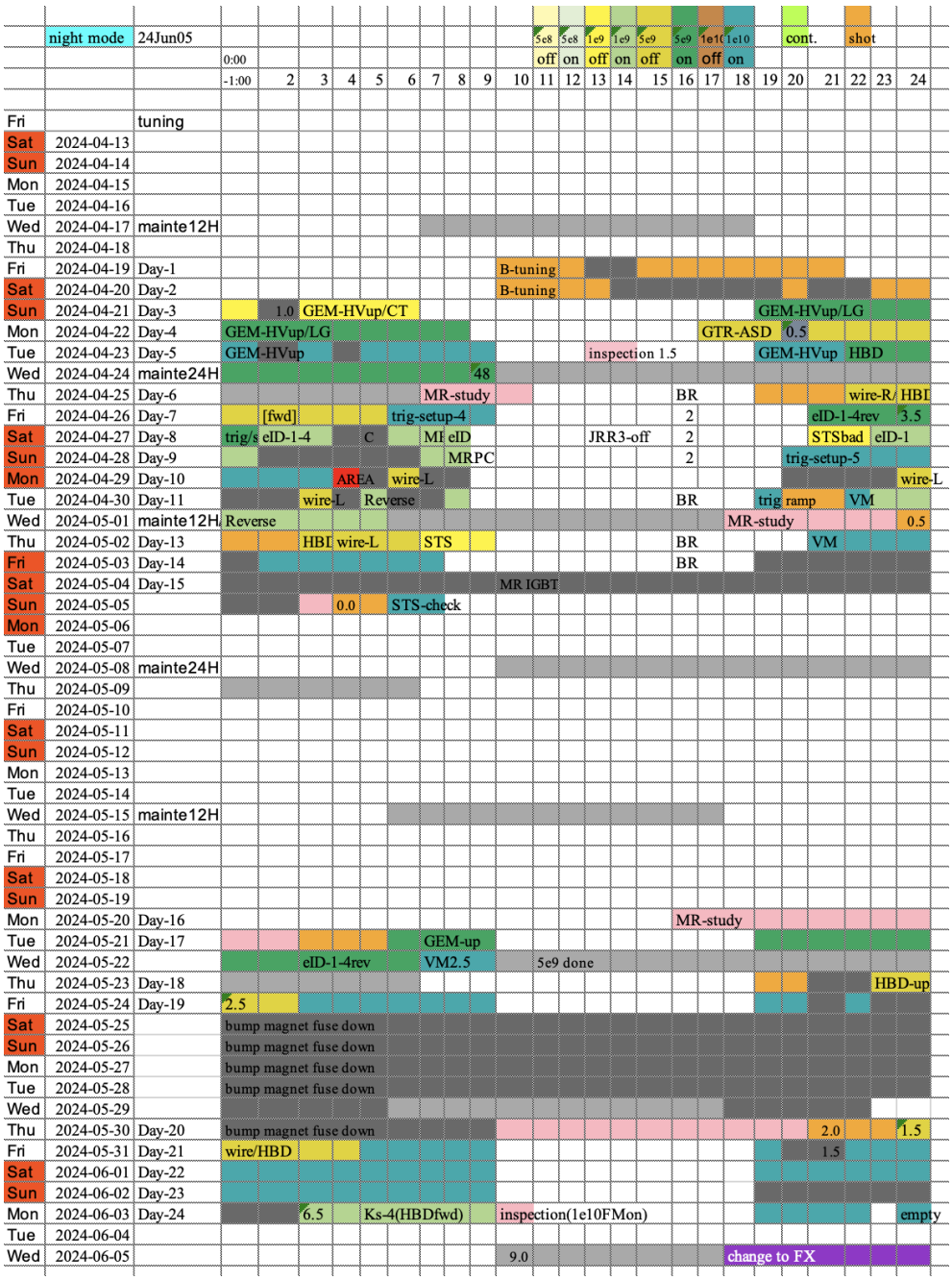

Figure 4.10: Study conducted on Run0-e. Each row represents one day, and each column represents one hour. Colours correspond to beam intensity, with white and grey areas indicating periods when the beam was unavailable. Additionally, the text labels correspond to the actions performed; for example, 'GEM-HVup' denotes ramping up the high voltage for GTR and HBD, while 'VM' refers to a run conducted in the Vector Meson Run state, triggering electron pairs originating from vector mesons.

Chapter 5

Analysis of J-PARC E16 Run0e

5.1 Reconstruction of di-electron invariant mass spectrum

5.1.1 Pair track selection

First, the procedure for obtaining the invariant mass distribution is described. Initially, tracking is performed across all possible combinations of the four layers: GTR and SSD. The Runge-Kutta method was employed for track fitting. Reconstructed tracks are extrapolated to the HBD and LG detection planes, where hits on the HBD and LG are required, respectively. Electron-positron identification is thus performed, seeking positron tracks in the left arm and electron tracks in the right arm. For electron identification, hits in the HBD and LG associated with the track require both an electron-like HBD cluster (ADC $>$ 6 photoelectrons and cluster size $\geq$ 2) and an LG hit ($0.53 < E/P < 2$). In principle, a single electron track should generate one HBD cluster. Therefore, an HBD cluster should be associated with one electron track. However, the high multiplicity of GTRs can lead to the formation of fake tracks. Consequently, it frequently occurs that multiple tracks are associated with a single HBD cluster. To correctly reconstruct the invariant mass distribution, it is necessary to select the true track from these candidates.

However, the background for the ϕ meson is relatively small compared to that for the ω meson, the main background being combinatorial. Consequently, the signal-to-noise ratio is relatively favorable. Therefore, in the analysis of the ϕ meson, it is permissible to associate multiple track candidates with a single HBD cluster when

different SSD hits are used or when the reconstructed momentum differs by 0.2 GeV/c or more. All possible pairs are formed from these candidates. Next, we reconstruct the target from the pair tracks. Figure 5.1 shows the distribution of vertices when fitting two tracks without fixing the target's z-coordinate, subject to the condition that the pair shares a common vertex somewhere. A distinct structure emerges in the positions of the three targets. From the resulting vertex distribution, we determine which pair of tracks originate from which target. We then re-perform the pair fitting with the vertex z-coordinates fixed to the target z-coordinates, thereby obtaining the invariant mass distribution.

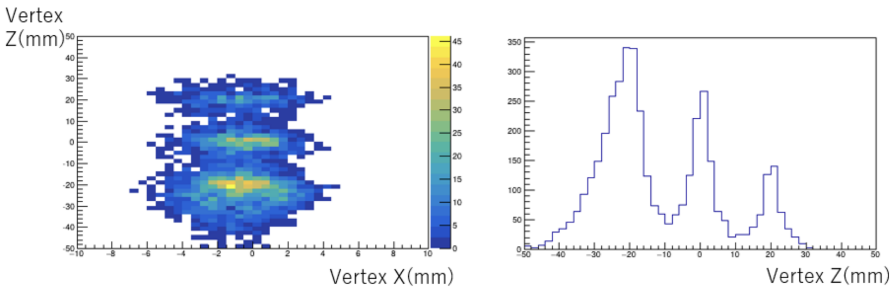

Figure 5.1: Vertex distribution when performing pair tracking without fixing the z-coordinate. A distinct structure is visible at the target position. Left: x-z plane. Right: Distribution of vertex z-coordinates.

The invariant mass distribution obtained through such analysis is shown in Figure 5.2.

Furthermore, Figure 5.3 shows the invariant mass distribution of electron pairs obtained by analyzing the data separately for each target [68].

In Figure 5.3, an exponential function was used for background fitting, whilst a Gaussian function was used for the peak portion of the ϕ meson. The background shape was determined from this fitting, and the yield of the ϕ meson was established as the integral value after background subtraction. To evaluate systematic errors, we examined another background model using quadratic functions along with signal shapes derived from simulations based on the embedding described in section5.1. For all fittings, the integration region was kept identical. Furthermore, to assess systematic errors, we considered multiple different binning schemes. Ultimately, systematic errors were assigned as the maximum deviation from the representative value.

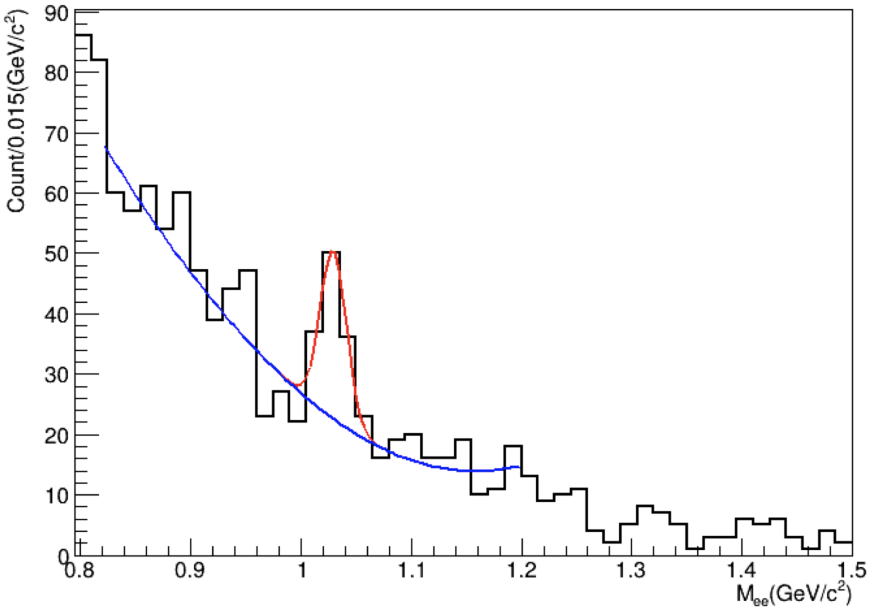

Figure 5.2: Peak of the ϕ meson in the invariant mass distribution of electron pairs

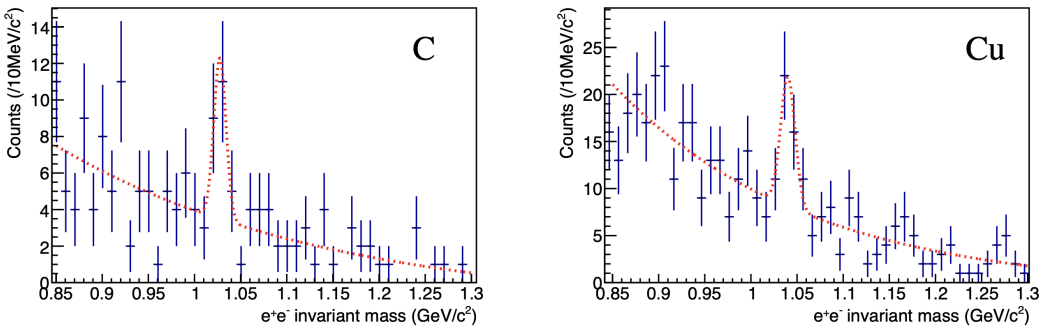

Figure 5.3: Peak of the ϕ meson in the invariant mass distribution of electron pairs for each target. The Cu target is the sum of the two plates. [68]

5.2 Efficiencies

The online trigger performance of the LG, HBD, and GTR detectors, which issue trigger signals to investigate trigger efficiency, and the performance of the trigger logic module were evaluated. Subsequently, the efficiency of the offline cuts was also evaluated. For LG and HBD, trigger efficiency was evaluated channel-by-channel using offline tracking data. When an offline track passed through a particular detector channel, a trigger signal was verified from that channel. Consequently, the efficiency confirmed here also encompasses the performance of the front-end circuitry for trigger generation. The channel-by-channel trigger efficiency obtained individually was implemented in the detector simulation to determine the acceptances for e^+ and e^- originating from ϕ mesons. This enabled verification that the trigger threshold was not excessively high. As a result, the trigger efficiency for $\phi \to e^+e^-$ events was 93%±0.05% for LG and 34%±0.1% for HBD in general. Therefore, the efficiency for single-track events was 97% (LG) and 59% (HBD). For reference, the design values for the single-track trigger efficiency are 90% (LG) and 68% (HBD). The details of the evaluation method are described in the following subsection. Regarding the trigger logic module, data were collected when a trigger known as the two-electron(VM) trigger mode was activated to acquire $\phi \to e^+e^-$ data. Candidate single-electron tracks were determined by geometrically matching the LG, HBD, and GTR trigger tiles. Furthermore, to suppress the contributions of π^0 Dalitz decay and gamma conversion, the trigger was set to fire only when the opening angle was large. Specifically, it required that the LG trigger points be separated by at least 45 degrees. An efficiency exceeding 99.99% was confirmed in the two-electron trigger data. That is, virtually all trigger events possess a trigger hit that satisfies the trigger conditions. Meanwhile, the analysis results, confirming whether combinations that meet the two-electron trigger conditions are activated, under the statistical constraints of two-electron candidates within the data acquired with the low-bias trigger, agree at 100%.

5.2.1 GTR

The GTR layer efficiency was calculated. The results are summarized in Table 5.1. In principle, the tracking layer comprises four layers for both x and y, combining STS and GTR. However, the efficiency is calculated based on whether the reconstructed track, when tracking excludes the layer whose detection efficiency is evaluated, contains a cluster of hits within the evaluated layer.

Table 5.1: Detection efficiency of GTR. The efficiency of the GTR-300 strip signal was evaluated in the presence of the trigger signal.

Size of GTR	module 104		module 106	
	ϵ_x	ϵ_y	ϵ_x	ϵ_y
GTR-100(strip)	100	100	96	98
GTR-200(strip)	100	97	93	94
GTR-300(trigger)	-	63	-	74
GTR-300(strip)	99	84	98	96

Using this, the single-track efficiency becomes 91% for Module 104 (including STS efficiency of 94%) and 81% for Module 106. Consequently, the efficiency of the pair reconfiguration becomes 74%. The ASD of the GTR receives charge from the rear surface of the GEM-3 in the GTR-300 and generates a trigger signal. The overall efficiency is 63% for module 104 and 74% for module 106, with a paired efficiency of 46%. This is worse than the design value of 88%, due to the need to set a higher threshold to eliminate ASD noise. Furthermore, the positional dependence of the ASD trigger efficiency is shown in Table 5.2.

Next, we evaluated reconstruction efficiency under realistic background conditions using embedding. This method involves embedding waveform samples from GTR tracks in actual experimental data and applying the same reconstruction procedure described in Section 5.1.1 to assess the efficiency with which the embedded tracks are correctly reconstructed. Waveform samples are extracted from low-intensity data (1.0×10^9 protons per spill). As the reconstruction efficiency depends on event multiplicity, all recorded events were scanned to account for multiplicity dependence. The average efficiency for the three targets (evaluated at the most frequent multiplicity) was 30%. The systematic uncertainty estimated from the multiplicity dependence correction was calculated to be 12%.

5.2.2 LG

The energy calibration for each channel of the LG was performed in two steps. First, the response to charged particles was used for calibration without requiring a single-electron signal in the HBD. Charged particles are detected by the GTR and STS. Charged pions do not produce electromagnetic showers in the lead glass but emit Cherenkov light. The pion peak within the ADC distribution was used for the first step of calibration. The subsequent step used the energy-momentum distribution of the electron candidates selected by the HBD. The value of each channel E/p was

Table 5.2: Channel dependence of ASD trigger efficiency. The "-" indicates a dead channel or a noisy channel. Each channel corresponds to one of the 24 GEM strips of the GEM-3 on the GTR-300. The GEM strips are horizontally elongated, with each channel representing vertical information: channel 0 corresponds to the lowest position and channel 23 to the highest position.

channel	module 104	module 106
0	-	-
1	93	85
2	85	82
3	54	70
4	78	80
5	83	86
6	80	72
7	45	-
8	44	64
9	70	73
10	72	71
11	65	69
12	79	73
13	79	73
14	79	69
15	80	59
16	56	67
17	78	74
18	80	69
19	73	-
20	-	-
21	92	75
22	90	80
23	-	-

corrected so that it was equal to one for electrons. Furthermore, the dependence of the incident position on the E/p distribution was also corrected. Using the electron beam from the KEK PF-AR test beamline, we measured the response to electrons under various incident conditions[69]. This correction was applied to cancel the dependencies measured at PF-AR from the data acquired during Run0-e. Figures 5.4(a) and (c) show the peak positions of the E/p distribution for Run0-e data after applying the correction for incident position. Here, the sample momentum range is 0.5 to 0.6 GeV/c in (a) and 1.0 to 1.1 GeV/c in (c). Some correlations remain, but the significance is approximately 10%. The width of the E/p distribution was also confirmed in Figure 5.4(b) and (c). The sample in (b) is the same as that in (a), and the sample in (d) is the same as that in (c). The blue points represent data from Run0-e. In Figure 5.4(b), the Run0-e data reproduce the PF-AR data (magenta). In Figure 5.4(d), the resolution is poor in the small incident position y region, resulting in slightly worse performance compared to the PF-AR results. When evaluating efficiency using the following simulation, this actual response should be taken into account. Figure 5.5(a) shows the energy-momentum distribution after

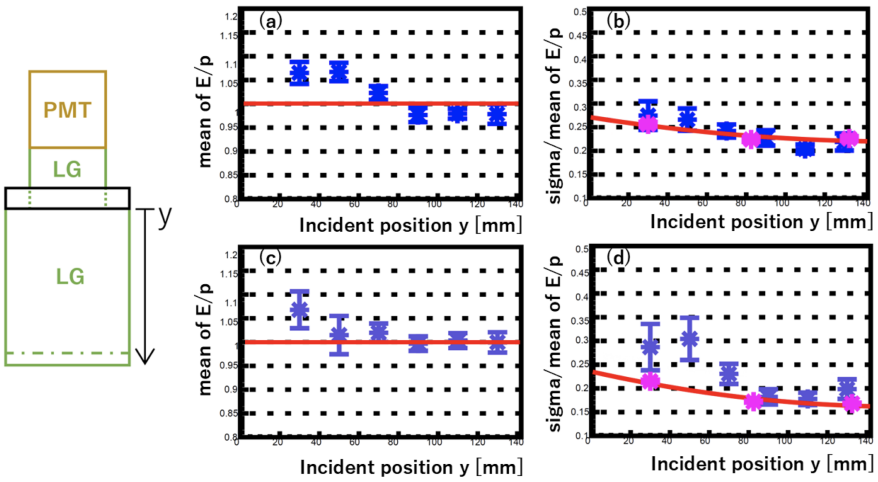

Figure 5.4: (a), (c) Peak position of the E/p distribution. (b), (d) Width of the E/p distribution. The momentum range of the samples is 0.5–0.6 GeV/c for (a) and (b), and 1.0–1.1 GeV/c for (c) and (d). The blue dots represent data from Run0-e, while the magenta dots denote data points from the test experiment conducted at KEK PF-AR[69]. The test experiment results were fitted with a quadratic function, indicated by the red lines in (b) and (d). The red lines in (a) and (c) represent the $E/p = 1$ line.

energy calibration and correction for incident position. Figure 5.5(b) presents the sample plot after excluding data points where $y < 75$ mm to remove positional dependence and low resolution effects.

The trigger efficiency for electron pairs originating from ϕ mesons was evaluated

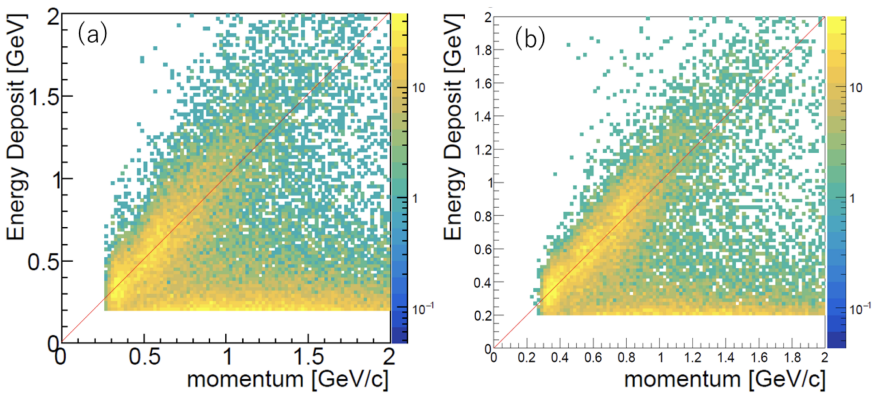

Figure 5.5: Energy-momentum distribution. In (b), those with $y < 75$ mm are excluded.

based on the response described above. Specifically, the evaluation was performed by simulating the following procedure.

- The momentum of the ϕ meson is calculated using JAM(event generator)[67].
- Electrons and positrons decayed from ϕ meson pass the spectrometer according to their momentum and magnetic field. Then we obtain their momentum, the LG channel ID to which the electrons reach, and the incident position on the LG block.
- The energy loss distribution is determined according to a Gaussian distribution, with its mean being the momentum of the incident electron. The width of the distribution follows the red line in Figure 5.4(b), imparting an incident position dependence. The red line was obtained for an electron of 0.5 GeV/c. This simulation simulates electron pairs originating from the ϕ meson, whose momentum is in most cases greater than 0.5 GeV/c; therefore, this estimate is conservative.
- When an electron passes through two LG blocks, the energy loss is distributed across two channels.
- Apply the trigger threshold of Run-0e to the energy loss obtained in this manner.

This simulation achieved a trigger efficiency of 98% for single tracks. The systematic error arising from the energy loss of a single electron distributed across two LG blocks was evaluated at 2%. The pair efficiency, that is, the efficiency of triggering the ϕ meson, was 96%. This is a sufficiently high efficiency. Finally, to evaluate the meson

yield in Run-0e, we examine the impact of offline cut conditions. In subsection 5.1.1, we require the energy-to-momentum ratio to be between 0.53 and 2. Taking into account this condition alongside the acceptance of the detector and the dead zone in Run-0e, the overall efficiency of $\phi \to e^+e^-$ is estimated to be 91%. This corresponds to a single-track efficiency of 95%.

5.2.3 HBD

To evaluate the overall efficiency of the trigger, the turn-on curves were obtained for each trigger channel of the HBD. Figure 5.6(a) shows the charge distribution of the electron sample obtained above and the turn-on curve for one channel. The turn-on curve becomes shallower due to trigger signal noise. The distribution of electrons that survive the trigger threshold is shown in magenta in Figure 5.6(b). The trigger efficiency is calculated as the ratio of the magenta line (number of surviving electrons) to the blue line (total number of electrons). Trigger efficiency is evaluated for each trigger channel. Figure 5.7 shows the positional dependence of trigger efficiency for the foremost module. Despite differing gains, the same threshold was applied to all channels, resulting in significant variations in trigger efficiency between channels.

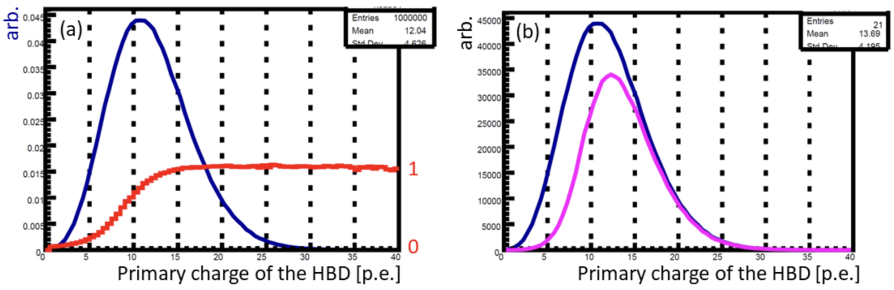

Figure 5.6: The charge distribution of the electron sample is shown by the blue line in (a) and (b). The red line in (a) represents the charge dependence of the trigger efficiency (turn-on curve). The magenta line in (b) shows the distribution of surviving electrons when the trigger efficiency of the red curve is multiplied by the blue line.

The overall trigger efficiency for electrons and positrons originating from mesons was evaluated in simulations for LG as described in 5.2.2. The results yielded an efficiency of 59% for single tracks and 34% for paired tracks, with the single track efficiency being lower than the design value of 68%. To evaluate the yield of the ϕ meson obtained in Run0-e, offline cut conditions were also examined. As shown in subsection 5.1.1, a charge threshold of six photoelectrons and a cluster size of two or more were applied. The 6-photoelectron threshold is not a strict cut for triggered samples, as indicated by the magenta line in Figure **??**(b). Furthermore, applying

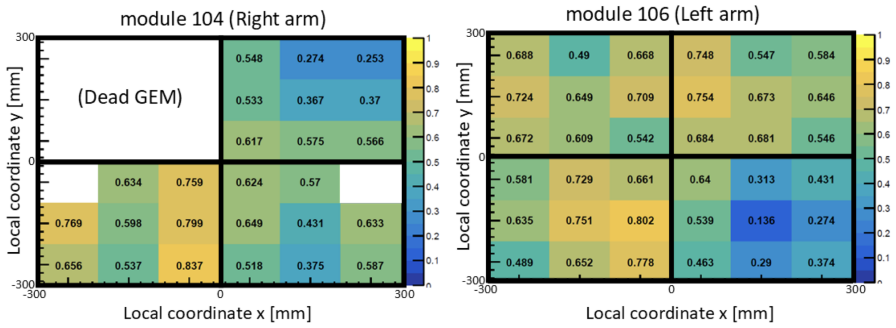

Figure 5.7: Trigger efficiency per trigger channel in modules 104 and 106.

Table 5.3: Various efficiency values.

electron ID efficiency (HBD)$\epsilon_{\mathrm{HBDeID}}$	56%	for single track, including trigger eff.
electron ID efficiency (LG)$\epsilon_{\mathrm{LGeID}}$	95%	for single track, including trigger eff.
GTR trigger efficiency$\epsilon_{\mathrm{GTRtrg}}$	46%	GTR-ASD, for a pair
Trigger logic efficiency$\epsilon_{\mathrm{trgLog}}$	84%	
detector acceptanceR_{acc}	1.49%	8 module configuration
pair reconstruction efficiencyϵ_{pair}	30%	74%(layer eff.)×41%(reco eff.)
additional analysis cutsϵ_{ana}	91%	timing and geometrical match of detectors etc.

the cluster size cut to triggered samples with six or more photons still preserves 95% ± 2% of the events. In summary, the single-electron efficiency of the HBD is 56%, calculated as the product of the trigger efficiency (59%) and the offline efficiency (95%). Consequently, the pair efficiency is 31%.

5.3 Cross section

Summarizing all the efficiencies achieved so far yields the following table 5.4.

Therefore, the total efficiency for the electron pair is as follows.

$$\epsilon_{\mathrm{total}} = \epsilon_{\mathrm{GTRtrg}} \times (\epsilon_{\mathrm{HBDeID}} \times \epsilon_{\mathrm{LGeID}})^2 \times \epsilon_{\mathrm{pair}} \times \epsilon_{\mathrm{ana}} \tag{5.1}$$

The yield of ϕ mesons obtained is calculated as follows using the above efficiency:

$$N_{\phi} = N_{\phi/1\mathrm{event}} \times N_{\mathrm{event}} \times R_{\mathrm{branch}} \times \epsilon_{\mathrm{total}} \times R_{\mathrm{acc}} \tag{5.2}$$

Here, $N_{\phi/1\mathrm{event}}$ denotes the number of ϕ mesons produced per pA collision event, N_{event} denotes the number of pA collision events, and R_{branch} denotes the branching

ratio for $\phi \to e^+e^-$. Furthermore, R_{acc} represents the acceptor of the spectrometer. $N_{\phi/1\text{event}}$ is expressed as follows using the cross section σ_ϕ for the production of the ϕ meson in pA collisions.

$$N_{\phi/1\text{event}} = \sigma_\phi \times \frac{\rho_{\text{target}} d_{\text{target}}}{A_{\text{target}}} N_A \tag{5.3}$$

Here, ρ_{target} denotes the density of the target, with the carbon target being 2.21 g/cm^3 and the copper target being 8.96 g/cm^3. d_{target} represents the thickness of the target, with the carbon target being 0.05 cm and the copper target being 0.008 cm. A_{target} denotes the atomic number of the target and N_A is the Avogadro number. Furthermore, N_{event} can also be expressed as the proton number. It is obtained by multiplying the number N_{proton} measured by an ion chamber positioned upstream of the beam dump, the veto ratio R_{veto} (the proportion lost due to the GTR multiplicity veto), and the DAQ live time. The GTR multiplicity veto is described in Section 4.2.1. However, ion chamber measurements lack time information. Therefore, during the veto period, monitoring was performed using the streaming TDC. Since it had been confirmed that the number of hits in the LG is proportional to the beam intensity, the number of hits in the LG during the veto period was obtained via the streaming TDC. Then, this was divided by the total number of hits to calculate the proportion of protons lost due to the GTR multiplicity veto. This resulted in an estimated value of approximately 71%. The DAQ live time is the ratio of accepted triggers to requested triggers, calculated from values recorded using the streaming TDC, and was approximately 85%. Furthermore, the systematic error of this method was assessed at 3%. Consequently, N_{event} is estimated to be approximately 1.21×10^{14} events for Run0-e.

Therefore, the cross section for the production of the ϕ meson is expressed as follows.

$$\sigma_\phi = \frac{N_\phi}{N_{\text{event}} R_{\text{branch}}} \frac{1}{R_{\text{acc}} \epsilon_{\text{total}}} \frac{A_{\text{target}}}{\rho_{\text{target}} d_{\text{target}} N_A} \tag{5.4}$$

In Run0-e, the targets were arranged along the beam axis in the order Cu, C, Cu. As shown in Figure 5.3, the experimental yield of the ϕ meson was obtained with counting by distinguishing the origin of the pair tracks at their generation points. The results are summarized in the following Table 5.4.

This yield is converted to the production cross section using equation 5.4. However, since the acceptor and efficiency depend on momentum, the momentum distribution of the ϕ meson is required. Regarding efficiency, the momentum dependence has not yet been analyzed; only overall efficiency has been obtained. The momentum

Table 5.4: Yield of ϕ mesons obtained at each target [68].

Target	Yield	χ/ndf
C	11.9±6.8±5.2	40.5/39
Cu	23.6±11.0±8.5	37.8/39

dependence of the acceptance can be verified using a p+A collision event generator and Monte Carlo simulations with Geant4. JAM was used as an event generator. Consequently, the total cross-sections for the ϕ meson were obtained for each target as follows [68].

- C: 2.0±1.1(stat.)±1.0(syst.) mb
- Cu: 10.3±4.8(stat.)±4.4(syst.) mb

The copper target was calculated from the weighted average of two measurements.

Using the cross sections obtained here, we estimate the yield achievable in E16Run2 and scale the spectral function of the ϕ meson calculated in Chapter 3 to estimate the invariant mass distribution.

Chapter 6

Estimation of yields in Run2

6.1 ϕ meson

Using the cross-section for the production of the ϕ meson obtained in Section , we estimate the yield for E16 Run2. Although many aspects of Run2 remain unconfirmed, the initial plan was for Run1 to comprise 160 shifts and Run2 320 shifts (1 shift = 8 hours). However, several efficiencies are lower than the design values, necessitating an extension of Run1 to 360 shifts to achieve sufficient statistics. Therefore, assuming that Run2 remains twice the length of Run1 as originally planned, we set it to 720 shifts here. In Run0-e, the length of one spill was approximately 4.24 seconds, which means that 849 spills of beam arrived per hour. Since each spill contained 1.0×10^{10} protons, a total of 4.89×10^{16} protons will be irradiated onto the target during Run2. Furthermore, multiplying the GTR multiplicity veto rate of 72%, the production time of approximately 62% (the proportion of Run2 time available for VMrun), the proportion of time unavailable due to DAQ downtime of approximately 10%, and the DAQ operational efficiency of 90%, yields an effective number of pA collision events recorded of 1.77×10^{16}. From this, the yield is estimated based on equation 5.2, incorporating effects such as the efficiency discussed in Section 6.1. However, acceptance differs between Run0-e and Run2. In Run2, in addition to the existing middle 8 modules, 9 modules each are added to the upper and lower sections, expanding the acceptance to 3.25 times that of Run0-e. Calculating with the same efficiencies as before, for an arrangement of Cu, C, and Cu targets, the calculation yields 52k ϕ mesons from the Cu target, 68k from the C target, totaling 172k ϕ mesons. This is used to estimate the invariant mass distribution in Run2, taking into account chiral mixing at finite density. Furthermore, for the lead target case, since the data was not acquired in Run0-e, estimating the yield similarly using

the cross section measured at 12 GeV in the KEK-PS E325 experiment converted to 30 GeV yields a calculation indicating that 20k ϕ mesons can be obtained from a single target.

6.2 Backgrounds

As explained in section3.4, the background yield is calculated for the three combinations ee, $e\pi$, and $\pi\pi$ using the equation 3.10. The simulation using JAM and Geant4, as shown in section3.4, involved bombarding a single Cu target with 4.8×10^{10} protons at the Run1 acceptor (only the middle eight modules). Without event mixing, the number of various background events obtained from this simulation was approximately $ee \sim 6.9 \times 10^{-1}$, $e\pi \sim 1.88 \times 10^{5}$, and $\pi\pi \sim 6.73 \times 10^{2}$. Thus, the number of various background events produced per p+A collision is this $1/4.8 \times 10^{10}$ times. Furthermore, the electron identification efficiency for LG obtained in Run0-e was 0.95 for single tracks, while HBD was 0.56. Therefore, the electron identification efficiency for single tracks is $0.95 \times 0.56 = 0.28$. Furthermore, the charge-pion rejection efficiency was confirmed in test beam experiments prior to Run0-e and is 99.9997%. Therefore, the probability of incorrectly identifying a charged pion as an electron is $1 - \epsilon_{\pi\,\text{rejection}} = 3.0 \times 10^{-4}$. Furthermore, the other efficiency denoted as ϵ_{others} in equation 3.10 is given by $\epsilon_{\text{others}} = \epsilon_{\text{GTRtrg}} \times \epsilon_{\text{trg logic}} \times \epsilon_{\text{pair, reco}} \times \epsilon_{\text{ana}}$, with the respective values as shown in Table 5.4. Furthermore, in Run2, assuming 720 shifts as postulated in Section 6.1, 4.89×10^{16} protons are irradiated onto the target. Applying the GTR multiplicity veto of 72% and multiplying by the production time (approximately 62%) available for VMrun within Run2, and the downtime due to DAQ unavailability (approximately 10%), the effective number of pA collision events recorded becomes 1.77×10^{16}. Using these values, the yields of various background types generated for two Cu targets are as follows.

- e^+e^- pair from π^0 Dalitz decay and γ conversion: 53k
- $\pi^+\pi^-$ pair which is wrongly identified as an electron pair: 4.6k
- $e^\pm\pi^\mp$ pair from the combination of the above two: 29k

However, this simulation is time-consuming and resource-intensive, making it impractical to perform readily. Therefore, the background for the C and Pb targets is estimated as follows, based on the simulation results for Cu: Generally, the hadron production cross section in p+A reactions exhibits a dependence on the atomic

mass, where $\sigma \propto A^{\alpha}$. For electrons originating from the $\pi^{\pm}$ and π^{0} considered as background, it is known that $\alpha \sim 0.8 \pm 0.1$. Therefore, using this information, the following correction is applied.

$$N^{\mathrm{Bkg}}_{\mathrm{C,Pb}} = \frac{N^{\mathrm{Atom}}_{\mathrm{C,Pb}} A^{\alpha}}{N^{\mathrm{Atom}}_{\mathrm{Cu}} 63^{\alpha}} N^{\mathrm{Bkg}}_{\mathrm{Cu}} \tag{6.1}$$

However, N^{Atom} denotes the number of atomic nuclei within the target (including the number of target sheets), A represents the atomic masses of C and Pb, and 63 denotes the atomic mass of Cu. The estimated background counts for C and Pb are as follows.

- $e^{+}e^{-}$ pair from π^{0} Dalitz decay and γ conversion: 55k for C, 19k for Pb
- $\pi^{+}\pi^{-}$ pair which is wrongly identified as an electron pair: 4.8k for C, 1.6k for Pb
- $e^{\pm}\pi^{\mp}$ pair from the combination of the above two: 31k for C, 10k for Pb

Scaling each background in Figure 3.6 to achieve this quantity.

Chapter 7

Results and Discussions

This chapter presents the calculated results for the invariant mass distribution of electron pairs expected in E16 Run2, taking into account chiral mixing in finite density. This is achieved using the calculation method described in Chapter 3 and the ϕ meson production cross section obtained in Section 6.1. First, as discussed in section 2.3, the mixing strength is treated as a free parameter. We therefore vary the mixing strength to several values to confirm the results. Next, we examine the differences for each type of target atom. Finally, while varying the degree of chiral symmetry restoration, we estimate how much mass degeneracy of the chiral partners can be observed in the E16 experiment.

7.1 Effect of Mixing Strength

Following the mixing scheme introduced in Section 2.3, the mixing strength is treated as a free parameter. The scenario assumes the full 2560 hours of beam time anticipated for Run 2. At nuclear density ρ_0, a 30% restoration of chiral symmetry is assumed. No changes in the mass or width of the ϕ meson due to this chiral symmetry restoration are assumed. Instead, we envisage a scenario where the mass and width of the $f_1(1420)$ meson approach those of the ϕ meson. We calculated the electron-pair invariant mass distribution for this scenario in the E16 experiment Run2. The targets in this section are initially two Pb targets. This is primarily to facilitate understanding how the effects of chiral mixing influence the invariant mass distribution. As will be quantitatively confirmed in the next section 7.2, Pb has a larger nuclear radius than C or Cu, making it more susceptible to density effects. Measurement of the cross section for ϕ meson production in the 30 GeV p+Pb target has also not been

performed in Run0-e; therefore, the cross section scaled to 30 GeV from the KEK-PS E325 experiment (12 GeV) is used. Furthermore, the invariant mass distributions shown in the following present the results obtained by selecting the momentum regions where the $f_1(1420)$ meson signal can be observed with the highest significance for each mixing strength. First, the results for the mixing strength $c = 0.1\rho/\rho_0$ [GeV] are shown in Figure 7.1. For $c = 0.1\rho/\rho_0$ [GeV], the mixing strength is too weak to

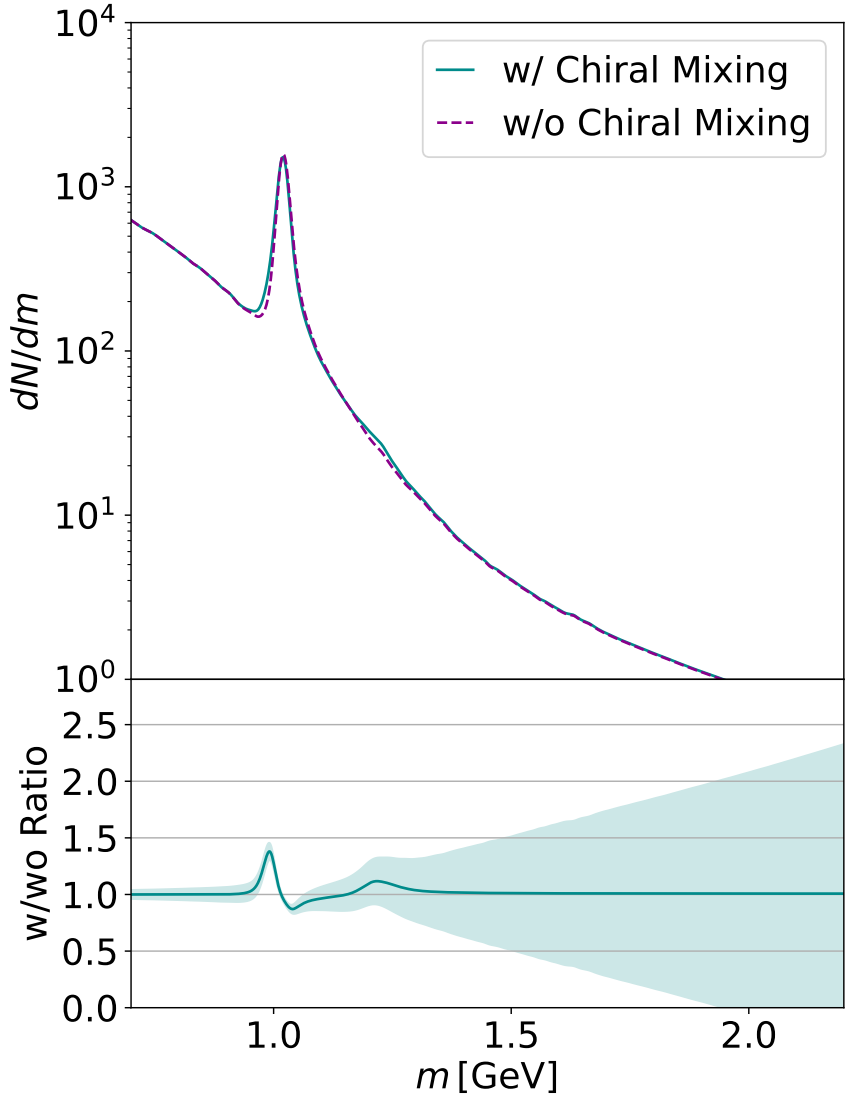

Figure 7.1: Expected electron-positron pair invariant mass distribution for E16 Run2 at mixing strength $c = 0.1\rho/\rho_0$ [GeV].

produce any significant difference between the presence and absence of chiral mixing. The results for a mixing strength $c = 1.0\rho/\rho_0$ [GeV] are shown in Figure 7.2. Only the mixing strength differs; all other conditions are identical to those previously described. In this case, the mixing strength becomes extremely large, causing the ϕ

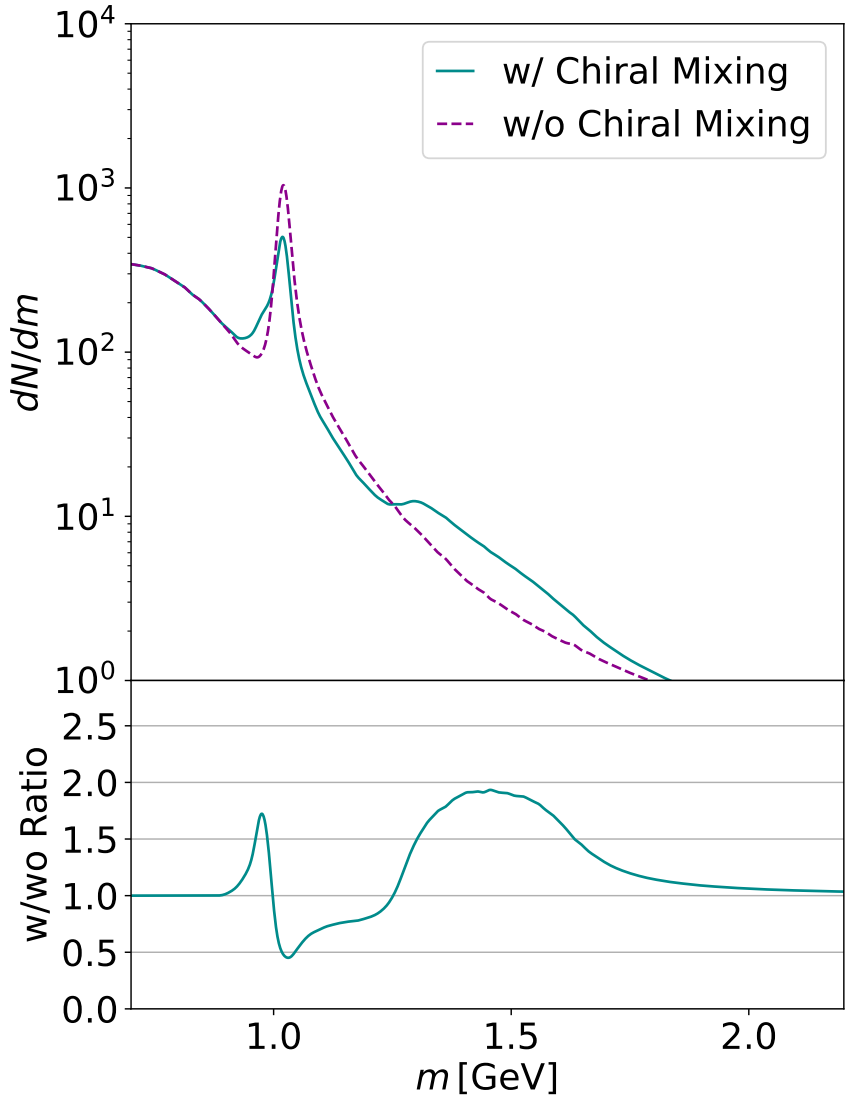

Figure 7.2: Expected electron-positron pair invariant mass distribution for E16 Run2 at mixing strength $c = 1.0\rho/\rho_0$ [GeV].

meson and the $f_1(1420)$ meson to mix strongly. Consequently, as shown in the right panel of Figure 2.5, the spectral function (i.e., the momentum components in the invariant mass distribution) exhibits a large $f_1(1420)$ meson component. However, the dispersion relation also changes significantly as a result of the large mixing strength. Consequently, the peak position of the $f_1(1420)$ meson differs for each momentum, and integration over momentum yields a low peak height, resulting in a low significance. Furthermore, consequently, the structure of the $f_1(1420)$ meson in the invariant mass distribution appears to be very broad. In this case, the in-medium pole mass of $f_1(1420)$ is difficult to discern, and it is also challenging to determine whether its mass is evolving towards mass degeneracy with the ϕ meson. In addition, a tail has formed to the left of the peak of the ϕ meson. This tail arises from the transverse wave component of the ϕ meson, due to changes in the dispersion relation caused by chiral mixing. The tail extending towards the lighter end in the mass distribution of vector mesons was typically attributed to energy loss due to processes such as bremsstrahlung from lepton pairs or interactions with the detector, effects from interactions with the medium, or mass changes arising from the restoration of chiral symmetry [33]. However, it has now been demonstrated that, in finite density, changes in the dispersion relation as a result of chiral mixing can also produce such a tail. This result demonstrates that the effects of chiral mixing in finite density can similarly generate such tails. As with the chiral mixing scenario examined here, only the transverse mode generates this tail; therefore, in principle, it is possible to distinguish between the two by examining the angular distribution of the lepton pair (for a more detailed discussion, see Ref.[70]).

The mixing strength values confirmed so far were consistent with the derivation of the WZW term [50] at $c = 0.1\rho/\rho_0$ [GeV] and with holographic QCD [47] at $c = 1.0\rho/\rho_0$ [GeV]. However, these values were calculated in the u and d sectors, or using methods such as the mean-field approximation [50], and thus are not highly precise figures. Moreover, in the s sector, the mixing strength includes the coupling constant $g_{\phi NN}$ for the interaction between the ϕ meson and the nucleons, meaning that there is no reliable predicted value for the mixing strength [51, 28, 52, 53]. Figure 7.3 shows the invariant mass distribution of the $f_1(1420)$ meson at the mixing strength, where it is observable with the highest significance. At the mixing strength $c = 0.4\rho/\rho_0$ [GeV], the $f_1(1420)$ meson was found to be observable with the highest significance. At this point, the $f_1(1420)$ meson is observable with approximately 2σ significance. In excess of weak mixing strengths, there is insufficient mixing, preventing any increase in the significance of $f_1(1420)$. In contrast, at excessively strong mixing strengths, the dispersion relation undergoes significant changes, creating distinct mass bands for the $f_1(1420)$ meson structure at different momenta. Consequently, integration does not

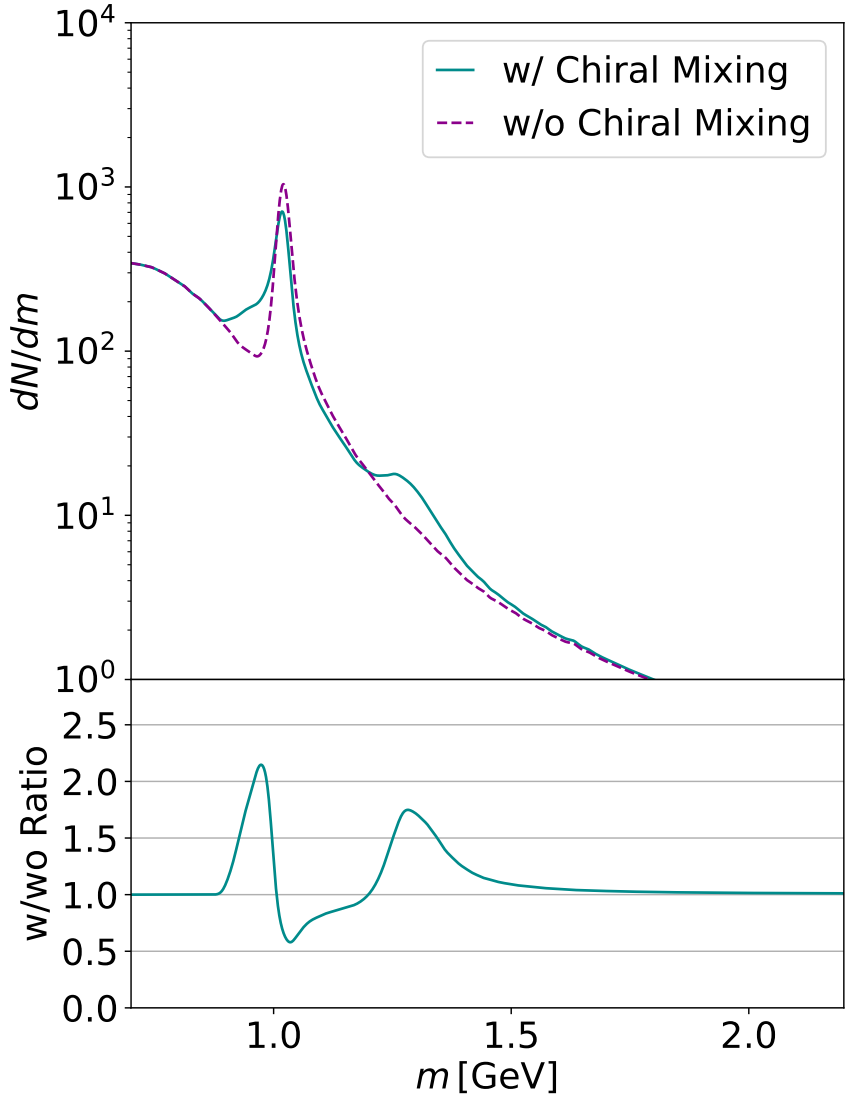

Figure 7.3: Expected electron-positron pair invariant mass distribution for E16 Run2 at mixing strength $c = 0.4\rho/\rho_0$ [GeV].

yield peak height, which is of low significance. However, it was found that a moderate mixing strength, i.e. between these extremes, enables the achievement of a high significance. However, as explained in section 2.3, the mixing strength in the s-sector may be weaker than in the u,d-sectors because it includes the coupling constant for the ϕ-N interaction. However, if the proportionality coefficient were halved, the density would need to be doubled to achieve the same mixing strength. In practice, for example, if the proportionality coefficient part of the mixing strength is 0.1 GeV and 0.4 GeV is ideal for a nuclear target, it should be possible to achieve the ideal density by reaching four times the nuclear density in heavy-ion collision experiments such as baryon stopping. However, in heavy-ion collisions, several issues must be considered, such as the spatiotemporal evolution of density and the Boltzmann suppression effect arising from the Bose-Einstein distribution of thermal photons at finite temperature. Regarding whether the strength of chiral mixing examined here is realistic, as stated in section 2.3, there is also research employing a different approach based on dimensional analysis, which indicates that the mixing strength is of the same order as the Fermi momentum (~ 0.2 GeV) at nuclear density. Therefore, it can be said that this value is not significantly deviant.

7.2 Effect of Difference of Target

Next, this section examines the target nucleus-dependent behavior of chiral mixing effects. E16 Run0-e used carbon and copper targets. Run2 further plans to use lead targets, among others. This section presents results for the three types: carbon, copper, and lead. However, for the carbon and copper results, the production cross section for the ϕ meson obtained in Run0-e is used. For the lead target, the production cross section from the KEK-PS E325 experiment, scaled to J-PARC's 30 GeV, is employed. Furthermore, the restoration of chiral symmetry is again assumed to be 30% based on the nuclear density. It is assumed that the mass of the ϕ meson remains unchanged due to chiral symmetry restoration, and that the $f_1(1420)$ meson degenerates towards the ϕ meson. Furthermore, the mixing strength is assumed to be $c = 0.4\rho/\rho_0$ GeV. The results for each type of nuclear target are shown below. Calculations were performed considering two scenarios for the entire beam time (2 times of Run 1, 720 shifts) envisaged for Run 2: one using two copper targets and one carbon target, and another using two lead targets and one carbon target over the same time period. The results are shown in the following Figure 7.4.

As can be seen in Figure 7.4, the effect of chiral mixing appears to increase progres-

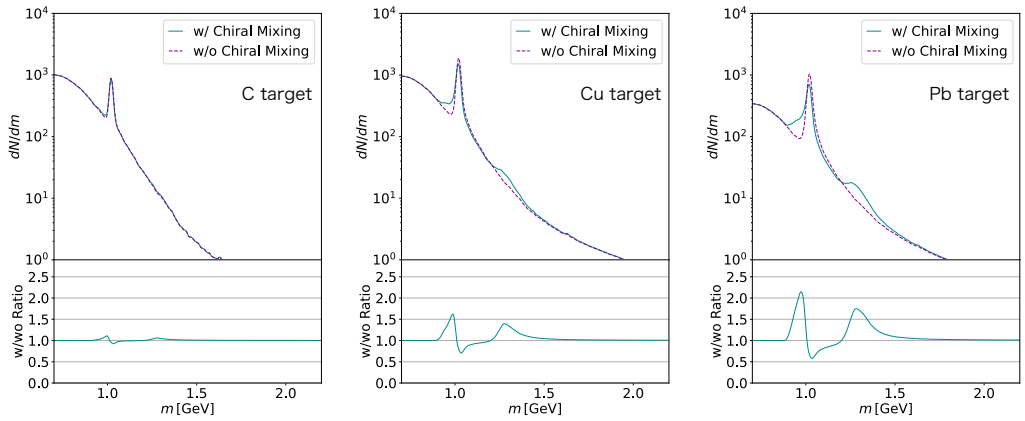

Figure 7.4: Expected electron-pair invariant mass distributions for E16 Run2 at various targets. Assumes mixing strength $c = 0.4\rho/\rho_0$ [GeV]. (Left) Carbon target. (Middle) Copper target. (Right) Lead target. Statistics for 720 shifts. Note that copper and lead assume the use of two targets.

sively in order C, Cu, Pb. This is because as the nuclear radius increases, more ϕ mesons decay within the nucleus. In contrast, in the carbon target with its small nuclear radius, most ϕ mesons escape into the normal vacuum outside the nucleus after production and decay without encountering any density. Consequently, their behavior approximates the Breit-Wigner distribution in near-vacuum, lacking the structure of the $f_1(1420)$ meson. This property allows the measurement results from the carbon target to serve as a reference for cases where chiral mixing does not occur. In theoretical calculations and Monte Carlo simulations such as those in this study, it is impossible to fully account for the dynamics of QCD and hadrons in reality and faithfully reproduce the invariant mass distribution. Consequently, when attempting to compare experimental results with theoretical calculations, especially in studies like this one seeking very small signals, contributions from other physics (background) that could not be fully accounted for interfere with interpretation. Therefore, by experimentally obtaining distributions with a carbon target, where density effects are negligible, and distributions with a lead target, where density effects are fully reflected, and comparing them, it becomes possible to isolate the pure density-dependent effects. This enables the analysis to find a $f_1(1420)$ meson signal in the data of the lead target.

7.3 Degree of Chiral Symmetry Partial Restoration and Mass Degeneracy of Chiral Partner

Finally, we examine the shape of the invariant mass distribution by varying the degree of chiral symmetry restoration. Keeping the mixing strength at the ideal condition of $c = 0.4\rho/\rho_0$ [GeV], we discuss how the invariant mass distribution changes at each degree of restoration and whether such changes can be detected experimentally. As confirmed in Section 1.2.5, the experimental results for the pionic atom suggest a restoration of chiral symmetry of approximately 40% in the u and d sectors at the nuclear density. In the s-sector, the restoration of chiral symmetry may be somewhat delayed, but a restoration of around 10% to 20% would not be unnatural. Therefore, we examined the shape of the invariant mass distribution while varying the degree of restoration in 10% increments, from no restoration of chiral symmetry to a 40% restoration.

As can be seen in Figure 7.5, as the chiral symmetry recovers, the structure of the $f_1(1420)$ meson approaches the peak of the ϕ meson, revealing a process of mass degeneracy. Furthermore, examining the peak position of the $f_1(1420)$ meson using the ratio of chiral mixing presence/absence under the ratio of chiral symmetry restoration (red line) below 7.5 is particularly instructive. CSRdelay, the peak position of the $f_1(1420)$ meson can be readily confirmed using the ratio indicating the presence or absence of chiral mixing. Compared to the case where chiral symmetry is not restored (red line), even a 10% restoration of chiral symmetry (yellow-green line) shifts the structure of the $f_1(1420)$ meson towards a lighter state by approximately 30–40 MeV. This mass change is sufficiently observable within the mass resolution (approximately 7 to 8 MeV) of the E16 experiment's spectrometer.

7.4 Discussion

Based on the results confirmed so far, we discuss the observability of mass degeneracy in chiral partners in the J-PARC E16 experiment. First, regarding mixing strength, it bears repeating that it involves significant theoretical uncertainties, including the inclusion of ϕ-N interaction coupling constants within the model. Currently, there are no theoretical means to determine its precise value; we can only determine that it lies on the order of magnitude of approximately 0.1 GeV at normal nuclear density. Assuming that the mixing strength was at its ideal value ($\sim$0.4 GeV at ρ_0), the present calculations indicate that within the statistical error range, acquiring 720

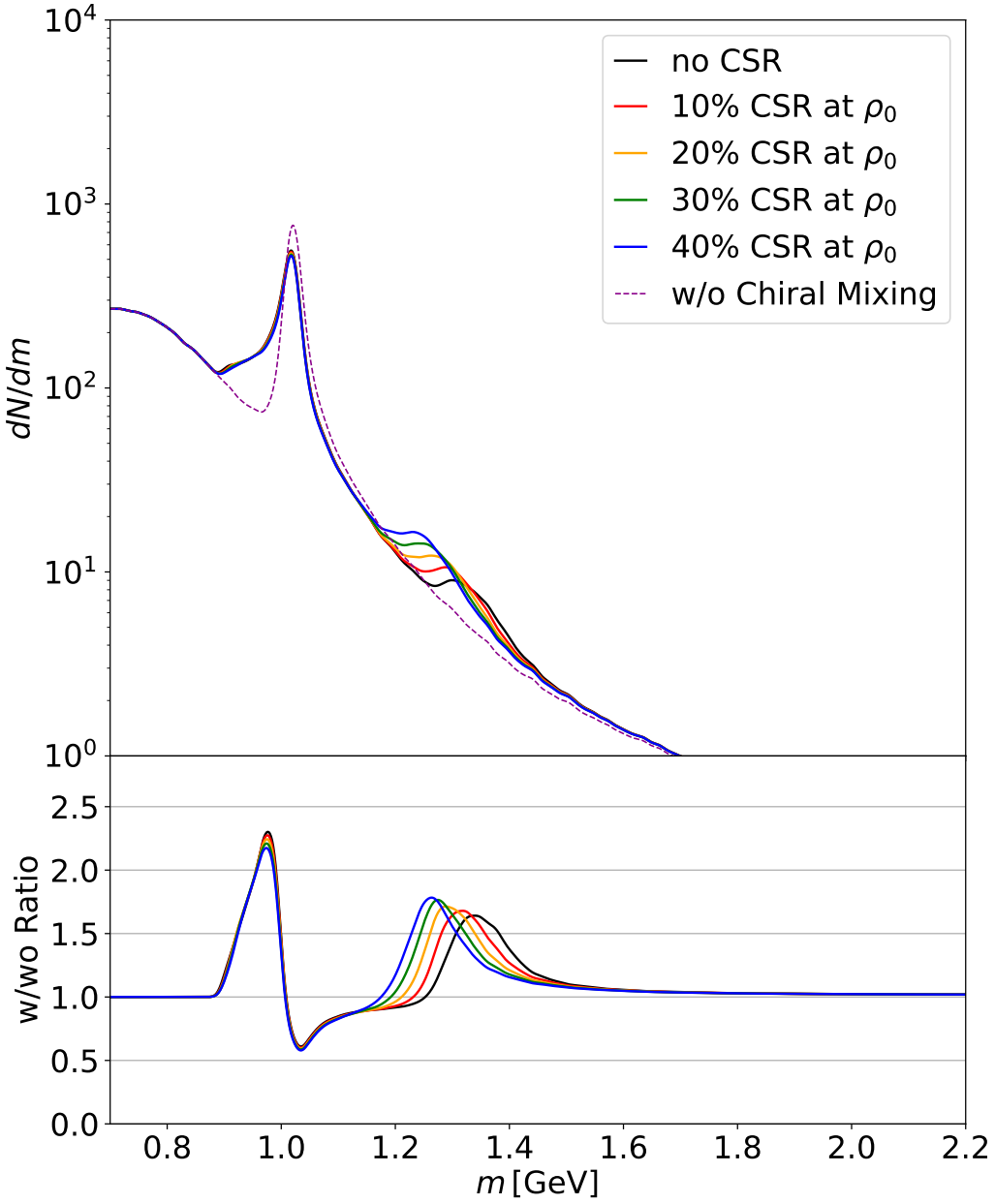

Figure 7.5: Mass distribution as the degree of chiral symmetry restoration at the nuclear density is varied. The target is lead, with mixing strength assumed as $c = 0.4\rho/\rho_0$. As chiral symmetry is restored, the structure of the $f_1(1420)$ meson approaches that of the ϕ meson peak, and mass degeneracy becomes apparent.

shifts (=5760 h) of data using two lead targets would yield an estimate capable of detecting the significance of 2σ of the $f_1(1420)$ meson signal, as shown in Figure 7.3. Furthermore, as shown in Figure 7.5, it was found that even a 10% restoration of chiral symmetry at nuclear density would produce a mass change in the $f_1(1420)$ meson sufficient to be detected by the E16 spectrometer. Therefore, it can be proposed that the J-PARC E16 experiment has the potential to detect the mass degeneracy of chiral partners at nuclear density. However, if the actual mixing strength is too weak, it is difficult to detect the $f_1(1420)$ meson signal in the E16 experiment. As shown in equation 2.11, the mixing strength is proportional to the density. Therefore, for example, if the proportionality coefficient was 0.1 GeV, achieving four times the nuclear density would, in principle, be equivalent to the ideal mixing strength of 0.4 GeV in ρ_0 presented here. However, while such high densities are achievable using heavy-ion collisions planned at facilities like J-PARC HI, the analysis becomes more challenging due to effects such as density evolution over time, higher-multiplicity background, and Boltzmann suppression at finite temperature. Nevertheless, the experiment remains highly worthwhile. Furthermore, even if no signal is detected in the E16 experiment despite sufficient statistics being obtained, an upper limit on the mixing strength can still be established. This would provide insights into the coupling constant of the ϕ-N interaction, making it a highly valuable experimental result. Moreover, when the actual mixing strength is excessively strong, the structure of the $f_1(1420)$ meson becomes extremely broad, as confirmed in Figure 7.2. In this case, the structure is not readily apparent at first glance, making a comparison with a reference such as a carbon target paramount. Even in such cases, if an excess is observed that is not present in the carbon target, it is possible to discuss the extent of chiral symmetry restoration in the nuclear density by assuming an effective theory of chiral mixing and an appropriate background model such as JAM, as in this calculation. Furthermore, compared to other mixing strengths, it might not be impossible to select the ϕ meson, which decays by sensing a density below the nuclear density in the nuclear periphery, by focusing solely on relatively large momenta to examine the invariant mass distribution, and then adjust the mixing strength. However, in that case, high-momentum components are inherently disadvantaged in terms of statistics. Furthermore, even for low-momentum particles, setting an extremely narrow momentum window to suppress broad distributions and aim for a spectrum function-like shape would still be statistically disadvantageous.

Furthermore, with respect to the tail structure that appears to the left of the ϕ meson peak, it has been discovered that this tail is generated not only by the previously considered mass change of the ϕ meson due to the restoration of chiral symmetry or by the ϕ-N interaction, but also by changes in the dispersion relation due to

chiral mixing. Analyzing this tail may allow constraints to be placed on the mixing strength, even if the $f_1(1420)$ meson signal is not observed. However, a challenge remains in separating this tail, as similar tails can be produced by various effects.

In any case, the mixing strength is theoretically only known to an order of magnitude and remains entirely unknown. Therefore, it is highly worthwhile to conduct experiments and analyzes such as the J-PARC E16 Run 2 $p + A$ fixed-target experiment with its large statistics. This is because, in the case of an ideal mixing strength, it is quite possible to sufficiently observe the onset of mass degeneracy at nuclear density during J-PARC E16 Run 2. Should no signal be observed despite sufficient statistics, constraints can be placed on the mixing strength. Furthermore, it has been recognized that this could yield significant results, potentially providing insights into the ϕ-N interaction via equation 2.11.

Chapter 8

Summary

At finite density, charge conjugation is explicitly violated, yielding a term where the vector field and axial vector field mix directly. This study focuses on the pair ϕ-$f_1(1420)$ among chiral partners, estimating the impact of finite-density-induced chiral mixing on the experimental results anticipated in J-PARC E16 Experiment Run 2. As a methodology, based on the theory of chiral effective fields, we calculated the spectral function of the ϕ meson, taking this mixing term into account. Subsequently, using mean-field approximation techniques, we estimated the ϕ-N interaction within the target nucleus, the dynamics of the off-shell ϕ meson via the PHSD transport approach, and the effects of chiral symmetry restoration using Generalized Hidden Local Symmetry and a simple model. Furthermore, we analyzed the electron-pair invariant mass distributions obtained at J-PARC E16 Run0e to evaluate the ϕ meson production cross-section in the E16 experiment (p+C and Cu, 30 GeV) and estimated the yield for Run 2. This enabled an assessment of the observability of the $f_1(1420)$ meson signal in Run 2. The results indicate that, for an ideal mixing strength (0.4 GeV at nuclear density), the signal is observable with approximately 2σ significance within the statistical error. Furthermore, it was demonstrated that if chiral symmetry recovers to approximately 10% at nuclear density, a mass change sufficient for detection by the E16 spectrometer could be expected. This indicates the potential of the J-PARC E16 experiment to observe the mass degeneracy of chiral partners at nuclear density.

Bibliography

[1] Ryugo S. Hayano and Tetsuo Hatsuda. Hadron properties in the nuclear medium. *Rev. Mod. Phys.*, 82:2949–2990, Oct 2010.

[2] Ralf Rapp. Signatures of thermal dilepton radiation at ultrarelativistic energies. *Phys. Rev. C*, 63:054907, Apr 2001.

[3] R. Rapp, J. Wambach, and H. van Hees. The Chiral Restoration Transition of QCD and Low Mass Dileptons. *Landolt-Bornstein*, 23:134, 2010.

[4] Kenji Fukushima and Chihiro Sasaki. The phase diagram of nuclear and quark matter at high baryon density. *Progress in Particle and Nuclear Physics*, 72:99–154, 2013.

[5] Jisu Kim and Su Houng Lee. Masses of hadrons in the chiral symmetry restored vacuum. *Phys. Rev. D*, 105:014014, Jan 2022.

[6] Su Houng Lee. Chiral symmetry breaking, chiral partners, and the k_1 and k^* in medium, 2024.

[7] A. Bazavov, S. Dentinger, H.-T. Ding, P. Hegde, O. Kaczmarek, F. Karsch, E. Laermann, Anirban Lahiri, Swagato Mukherjee, H. Ohno, P. Petreczky, R. Thakkar, H. Sandmeyer, C. Schmidt, S. Sharma, and P. Steinbrecher. Meson screening masses in $(2 + 1)$-flavor qcd. *Phys. Rev. D*, 100:094510, Nov 2019.

[8] Elisa Meninno and on behalf of the ALICE Collaboration. Dilepton measurements with the alice experiment at the lhc. *Journal of Physics: Conference Series*, 1602(1):012016, jul 2020.

[9] Antonio Uras. Low-mass dilepton production with alice at the lhc. *Nuclear Physics A*, 932:218–223, 2014. Hard Probes 2013.

[10] R. Arnaldi et al. NA60 results on thermal dimuons. *Eur. Phys. J. C*, 61:711–720, 2009.

[11] Ralf Rapp. Update on chiral symmetry restoration in the context of dilepton data. *Journal of Physics: Conference Series*, 420(1):012017, mar 2013.

[12] G. Agakichiev et al. e+ e- pair production in Pb - Au collisions at 158-GeV per nucleon. *Eur. Phys. J. C*, 41:475–513, 2005.

[13] G. E. Brown and Mannque Rho. Scaling effective lagrangians in a dense medium. *Phys. Rev. Lett.*, 66:2720–2723, May 1991.

[14] K. Ozawa, H. En'yo, H. Funahashi, M. Kitaguchi, M. Ishino, H. Kanda, S. Mihara, T. Miyashita, T. Murakami, R. Muto, M. Naruki, F. Sakuma, H. D. Sato, T. Tabaru, S. Yamada, S. Yokkaichi, Y. Yoshimura, J. Chiba, M. Ieiri, M. Nomachi, O. Sasaki, M. Sekimoto, K. H. Tanaka, and H. Hamagaki. Observation of ρ/ω meson modification in nuclear matter. *Phys. Rev. Lett.*, 86:5019–5022, May 2001.

[15] M. Naruki, Y. Fukao, H. Funahashi, M. Ishino, H. Kanda, M. Kitaguchi, S. Mihara, K. Miwa, T. Miyashita, T. Murakami, T. Nakura, F. Sakuma, M. Togawa, S. Yamada, Y. Yoshimura, H. En'yo, R. Muto, T. Tabaru, S. Yokkaichi, J. Chiba, M. Ieiri, O. Sasaki, M. Sekimoto, K. H. Tanaka, H. Hamagaki, and K. Ozawa. Experimental signature of medium modifications for ρ and ω mesons in the 12 gev $p + a$ reactions. *Phys. Rev. Lett.*, 96:092301, Mar 2006.

[16] R. Muto et al. Evidence for In-Medium Modification of the ϕ Meson at Normal Nuclear Density. *Phys. Rev. Lett.*, 98:042501, Jan 2007.

[17] B. Friman and H.J. Pirner. P-wave polarization of the -meson and the dilepton spectrum in dense matter. *Nuclear Physics A*, 617(4):496–509, 1997.

[18] P. Muehlich, V. Shklyar, S. Leupold, U. Mosel, and M. Post. The spectral function of the meson in nuclear matter from a coupled-channel resonance model. *Nuclear Physics A*, 780(3):187–205, 2006.

[19] E. Oset, A. Ramos, E. J. Garzon, R. Molina, L. Tolos, C. W. Xiao, J. J. Wu, and B. S. Zou. Interaction of vector mesons with baryons and nuclei. *Int. J. Mod. Phys. E*, 21:1230011, 2012.

[20] Swapan Das. Nuclear effects on the ρ meson produced in the inclusive photonuclear reaction, 11 2021.

[21] Horst Lenske. Interactions of ω mesons in nuclear matter and with nuclei. *Eur. Phys. J. A*, 59(10):222, 2023.

[22] G. Agakichiev et al. Enhanced production of low mass electron pairs in 200-GeV/u S - Au collisions at the CERN SPS. *Phys. Rev. Lett.*, 75:1272–1275, 1995.

[23] R. Rapp and J. Wambach. Chiral symmetry restoration and dileptons in relativistic heavy ion collisions. *Adv. Nucl. Phys.*, 25:1, 2000.

[24] R. Arnaldi et al. First measurement of the rho spectral function in high-energy nuclear collisions. *Phys. Rev. Lett.*, 96:162302, 2006.

[25] Hendrik van Hees and Ralf Rapp. Comprehensive interpretation of thermal dileptons at the SPS. *Phys. Rev. Lett.*, 97:102301, 2006.

[26] R. Nasseripour et al. Search for medium modification of the rho meson. *Phys. Rev. Lett.*, 99:262302, 2007.

[27] D. Trnka, G. Anton, J. C. S. Bacelar, O. Bartholomy, D. Bayadilov, Y. A. Beloglazov, R. Bogendörfer, R. Castelijns, V. Crede, H. Dutz, A. Ehmanns, D. Elsner, R. Ewald, I. Fabry, M. Fuchs, K. Essig, Ch. Funke, R. Gothe, R. Gregor, A. B. Gridnev, E. Gutz, S. Höffgen, P. Hoffmeister, I. Horn, J. Hössl, I. Jaegle, J. Junkersfeld, H. Kalinowsky, Frank Klein, Fritz Klein, E. Klempt, M. Konrad, B. Kopf, M. Kotulla, B. Krusche, J. Langheinrich, H. Löhner, I. V. Lopatin, J. Lotz, S. Lugert, D. Menze, J. G. Messchendorp, T. Mertens, V. Metag, C. Morales, M. Nanova, R. Novotny, M. Ostrick, L. M. Pant, H. van Pee, M. Pfeiffer, A. Roy, A. Radkov, S. Schadmand, Ch. Schmidt, H. Schmieden, B. Schoch, S. Shende, G. Suft, V. V. Sumachev, T. Szczepanek, A. Süle, U. Thoma, R. Varma, D. Walther, Ch. Weinheimer, and Ch. Wendel. Observation of in-medium modifications of the ω meson. *Phys. Rev. Lett.*, 94:192303, May 2005.

[28] S. et al. Acharya. Experimental evidence for an attractive $p-\phi$ interaction. *Phys. Rev. Lett.*, 127:172301, Oct 2021.

[29] Emma Chizzali, Yuki Kamiya, Raffaele Del Grande, Takumi Doi, Laura Fabbietti, Tetsuo Hatsuda, and Yan Lyu. Evidence of a p-ϕ bound state. 12 2022.

[30] Philipp Gubler, Masaya Ichikawa, Taesoo Song, and Elena Bratkovskaya. Production and in-medium modification of ϕ mesons in proton-nucleus reactions from a transport approach. 8 2024.

[31] A. Feijoo, M. Korwieser, and L. Fabbietti. Relevance of the coupled channels in the ϕp and ρ^0p Correlation Functions. 7 2024.

[32] Luciano M. Abreu, Philipp Gubler, K. P. Khemchandani, A. Martinez Torres, and Atsushi Hosaka. A study of the ϕN correlation function. 9 2024.

[33] Philipp Gubler and Keisuke Ohtani. Constraining the strangeness content of the nucleon by measuring the ϕ meson mass shift in nuclear matter. *Phys. Rev. D*, 90:094002, Nov 2014.

[34] Takahiro Nishi, Kenta Itahashi, DeukSoon Ahn, Georg P. A. Berg, Masanori Dozono, Daijiro Etoh, Hiroyuki Fujioka, Naoki Fukuda, Nobuhisa Fukunishi, Hans Geissel, Emma Haettner, Tadashi Hashimoto, Ryugo S. Hayano, Satoru Hirenzaki, Hiroshi Horii, Natsumi Ikeno, Naoto Inabe, Masahiko Iwasaki, Daisuke Kameda, Keichi Kisamori, Yu Kiyokawa, Toshiyuki Kubo, Kensuke Kusaka, Masafumi Matsushita, Shin'ichiro Michimasa, Go Mishima, Hiroyuki Miya, Daichi Murai, Hideko Nagahiro, Megumi Niikura, Naoko Nose-Togawa, Shinsuke Ota, Naruhiko Sakamoto, Kimiko Sekiguchi, Yuta Shiokawa, Hiroshi Suzuki, Ken Suzuki, Motonobu Takaki, Hiroyuki Takeda, Yoshiki K. Tanaka, Tomohiro Uesaka, Yasumori Wada, Atomu Watanabe, Yuni N. Watanabe, Helmut Weick, Hiroki Yamakami, Yoshiyuki Yanagisawa, and Koichi Yoshida. Chiral symmetry restoration at high matter density observed in pionic atoms. *Nature Physics*, 19(6):788–793, March 2023.

[35] M. Ichikawa et al. Commissioning Runs of J-PARC E16 Experiment. *Acta Phys. Polon. Supp.*, 16(1):1–A143, 2023. in:Proc. 29th International Conference on Ultrarelativistic Nucleus–Nucleus Collisions: Quark Matter 2022, Krakow, Poland, 2022.

[36] Ryotaro Muto, Keizo Agari, Kazuya Aoki, Yoshinori Fukao, Erina Hirose, Masaharu Ieiri, Ruri Iwasaki, Yohji Katoh, Michifumi Minakawa, Yuhei Morino, Kyoichiro Ozawa, Yoshinori Sato, Shin'ya Sawada, Yoshihisa Shirakabe, Yoshihiro Suzuki, Hitoshi Takahashi, Kazuhiro Tanaka, Akihisa Toyoda, Hiroaki Watanabe, and Yutaka Yamanoi. Development of lambertson magnet and septum magnets for splitting 30-gev proton beam in hadron experimental facility at j-parc. *IEEE Transactions on Applied Superconductivity*, 26(4):1–4, 2016.

[37] Y. Komatsu. Development of gem tracker for in-medium $\phi \to e^+e^-$ measurement. 2011. University of Tokyo, Master thesis.

[38] W. Nakai. Development of tracking detectors for j-parc e16 experiment. 2013. University of Tokyo, Master thesis.

[39] K. Suzuki. Development of trigger signal read-out system for hadron blind detector for di-electron measurement. 2019. Kyoto University, Master thesis.

[40] S. Ashikaga. Development of lead glass carolimetor for di-electron measurement. 2018. Kyoto University, Master thesis.

[41] Kazuya Aoki, Sakiko Ashikaga, Wen-Chen Chang, Tatsuya Chujo, Ren Ejima, Hideto En'yo, Shinichi Esumi, Dairon Rodriguez Garces, Hideki Hamagaki, Johann M. Heuser, Ryotaro Honda, Masaya Ichikawa, Daichi Ishii, Shunsuke Kajikawa, Jo Kakunaga, Koki Kanno, Akio Kiyomichi, Yusuke Hori, Chih-Hsun Lin, Yuhei Morino, Tomoki N. Murakami, Ryotaro Muto, Shunnosuke Nagafusa, Wataru Nakai, Satomi Nakasuga, Megumi Naruki, Toshihiro Nonaka, Hiroyuki Noumi, Shuta Ochiai, Makoto Ogura, Kyoichiro Ozawa, Adrian Rodriguez Rodriguez, Takao Sakaguchi, Hiroyuki Sako, Fuminori Sakuma, Susumu Sato, Shinya Sawada, Michiko Sekimoto, Kenta Shigaki, Kotaro Shirotori, Hitoshi Sugimura, Tomonori N. Takahashi, Tomohiro Taniguchi, Maksym Teklishyn, Alberica Toia, Rento Yamada, Kanako H. Yamaguchi, Yorito L. Yamaguchi, Shogo Yanai, and Satoshi Yokkaichi. Experimental investigation of vector mesons in medium through dielectron decay at j-parc. *Journal of Subatomic Particles and Cosmology*, 3:100019, 2025.

[42] W. Anderson, B. Azmoun, A. Cherlin, C.Y. Chi, Z. Citron, M. Connors, A. Dubey, J.M. Durham, Z. Fraenkel, T. Hemmick, J. Kamin, A. Kozlov, B. Lewis, M. Makek, A. Milov, M. Naglis, V. Pantuev, R. Pisani, M. Proissl, I. Ravinovich, S. Rolnick, T. Sakaguchi, D. Sharma, S. Stoll, J. Sun, I. Tserruya, and C. Woody. Design, construction, operation and performance of a hadron blind detector for the phenix experiment. *Nuclear Instruments and Methods in Physics Research Section A: Accelerators, Spectrometers, Detectors and Associated Equipment*, 646(1):35–58, 2011.

[43] F. Sauli. Gem: A new concept for electron amplification in gas detectors. *Nuclear Instruments and Methods in Physics Research Section A: Accelerators, Spectrometers, Detectors and Associated Equipment*, 386(2):531–534, 1997.

[44] Y. Giomataris and G. Charpak. A hadron-blind detector. *Nuclear Instruments and Methods in Physics Research Section A: Accelerators, Spectrometers, Detectors and Associated Equipment*, 310(3):589–595, 1991.

[45] M. Dey, V. L. Eletsky, and B. L. Ioffe. Mixing of vector and axial mesons at finite temperature: an Indication towards chiral symmetry restoration. *Phys. Lett. B*, 252:620–624, 1990.

[46] Chihiro Sasaki, Masayasu Harada, and Wolfram Weise. Role of axial-vector mesons near the chiral phase transition. *Nuclear Physics A*, 827(1):350c–352c, 2009. PANIC08.

[47] Sophia K. Domokos and Jeffrey A. Harvey. Baryon-number-induced chern-simons couplings of vector and axial-vector mesons in holographic qcd. *Phys. Rev. Lett.*, 99:141602, Oct 2007.

[48] Ren Ejima, Philipp Gubler, Chihiro Sasaki, and Kenta Shigaki. Toward a direct measurement of partial restoration of chiral symmetry at j-parc e16 via density-induced chiral mixing. *Phys. Rev. C*, 111:055201, May 2025.

[49] Norbert Kaiser and Ulf-G. Meissner. Generalized hidden symmetry for low-energy hadron physics. *Nuclear Physics A*, 519(4):671–696, 1990.

[50] Masayasu Harada and Chihiro Sasaki. A Novel spectral broadening from vector–axial-vector mixing in dense matter. *Phys. Rev. C*, 80:054912, 2009.

[51] Igor I. Strakovsky, Lubomir Pentchev, and Alexander I. Titov. Comparative analysis of ωp, ϕp, and $j/\psi p$ scattering lengths from a2, clas, and gluex threshold measurements. *Phys. Rev. C*, 101:045201, Apr 2020.

[52] Yan Lyu, Takumi Doi, Tetsuo Hatsuda, Yoichi Ikeda, Jie Meng, Kenji Sasaki, and Takuya Sugiura. Attractive $n-\phi$ interaction and two-pion tail from lattice qcd near physical point. *Phys. Rev. D*, 106:074507, Oct 2022.

[53] E.Ya. Paryev. Testing the -nuclear potential in pion-induced meson production on nuclei near threshold. *Nuclear Physics A*, 1032:122624, April 2023.

[54] Steven Weinberg. Phenomenological lagrangians. *Physica A: Statistical Mechanics and its Applications*, 96(1):327–340, 1979.

[55] Chihiro Sasaki. Signatures of chiral symmetry restoration in dilepton production. *Physics Letters B*, 801:135172, 2020.

[56] Chihiro Sasaki. Anomaly-induced chiral mixing in cold and dense matter. *Phys. Rev. D*, 106:054034, Sep 2022.

[57] HyungJoo Kim and Philipp Gubler. The ϕ meson with finite momentum in a dense medium. *Phys. Lett. B*, 805:135412, 2020.

[58] D. B. Kaplan and A. E. Nelson. Kaon Condensation in Dense Matter. *Nucl. Phys. A*, 479:273c, 1988.

[59] E. Oset and A. Ramos. decay in nuclei. *Nuclear Physics A*, 679(3):616–628, 2001.

[60] G. Q. Li, C.-H. Lee, and Gerald E. Brown. Kaon production in heavy-ion collisions and maximum mass of neutron stars. *Physical Review Letters*, 79:5214–5217, 1997.

[61] W.S. Chung, C.M. Ko, and G.Q. Li. Seeing phi mesons through dileptons. *Nuclear Physics A*, 641(3):357–378, 1998.

[62] Masako Bando, Taichiro Kugo, and Koichi Yamawaki. Nonlinear Realization and Hidden Local Symmetries. *Phys. Rept.*, 164:217–314, 1988.

[63] Masayasu Harada and Chihiro Sasaki. Dropping ρ and A_1 meson masses at the chiral phase transition in the generalized hidden local symmetry. *Phys. Rev. D*, 73:036001, Feb 2006.

[64] A. Bazavov, T. Bhattacharya, M. Cheng, C. DeTar, H.-T. Ding, Steven Gottlieb, R. Gupta, P. Hegde, U. M. Heller, F. Karsch, E. Laermann, L. Levkova, S. Mukherjee, P. Petreczky, C. Schmidt, R. A. Soltz, W. Soeldner, R. Sugar, D. Toussaint, W. Unger, and P. Vranas. Chiral and deconfinement aspects of the qcd transition. *Phys. Rev. D*, 85:054503, Mar 2012.

[65] W. Cassing and E. L. Bratkovskaya. Parton transport and hadronization from the dynamical quasiparticle point of view. *Phys. Rev. C*, 78:034919, 2008.

[66] W. Cassing and E. L. Bratkovskaya. Parton-Hadron-String Dynamics: an off-shell transport approach for relativistic energies. *Nucl. Phys. A*, 831:215–242, 2009.

[67] Y. Nara, N. Otuka, A. Ohnishi, K. Niita, and S. Chiba. Relativistic nuclear collisions at $10a$ gev energies from p + Be to au+au with the hadronic cascade model. *Phys. Rev. C*, 61:024901, Dec 1999.

[68] Satomi Nakasuga, Yuhei Morino, Kazuya Aoki, Yoki Aramaki, Daichi Arimizu, Sakiko Ashikaga, Wen-Chen Chang, Ren Ejima, Hideto En'yo, Dairon Rodriguez Garces, Johann M. Heuser, Ryotaro Honda, Masaya Ichikawa, Daichi Ishii, Shunsuke Kajikawa, Jo Kakunaga, Koki Kanno, Daisuke Kawama, Yusuke Komatsu, Takehito Kondo, Yusuke Hori, Hikari Murakami, Tomoki Murakami, Ryotaro Muto, Shunnosuke Nagafusa, Wataru Nakai, Megumi Naruki, Yuki Obara, Shuta Ochiai, Makoto Ogura, Kyoichiro Ozawa, Adrian Rodriguez Rodriguez, Hiroyuki Sako, Susumu Sato, Michiko Sekimoto, Kenta Shigaki, Kazuki

Suzuki, Tomonori Takahashi, Tomohiro Taniguchi, Maksym Teklishyn, Alberica Toia, Rento Yamada, Kanako Yamaguchi, Yorito Yamaguchi, Shogo Yanai, and Satoshi Yokkaichi. First measurement of meson production in 30 gev proton-nucleus reactions via di-electron decay at j-parc. *Prog. Theor. Exp. Phys. (To Be Published)*.

[69] J-PARC E16 collaboration. Pf-ar test beamline at kek.

[70] In Woo Park, Hiroyuki Sako, Kazuya Aoki, Philipp Gubler, and Su Houng Lee. Disentangling longitudinal and transverse modes of the ϕ meson through dilepton and kaon decays. *Phys. Rev. D*, 107(7):074033, 2023.